

PROPAGATION MODELS
FOR HILLY TERRAIN BASED ON RAY OPTIC METHODS

A THESIS SUBMITTED TO
THE GRADUATE SCHOOL OF NATURAL AND APPLIED SCIENCES
OF
MIDDLE EAST TECHNICAL UNIVERSITY

BY

ERKAN ERSİN YILDIRIM

IN PARTIAL FULLFILLMENT OF THE REQUIREMENTS
FOR
THE DEGREE OF MASTER OF SCIENCE
IN
ELECTRICAL AND ELECTRONICS ENGINEERING

SEPTEMBER 2015

Approval of the thesis:

**PROPAGATION MODELS
FOR HILLY TERRAIN BASED ON RAY OPTIC METHODS**

submitted by **ERKAN ERSİN YILDIRIM** in partial fulfillment of the requirements for the degree of **Master of Science in Electrical and Electronics Engineering Department, Middle East Technical University** by,

Prof. Dr. Gülbin Dural Ünver
Dean, Graduate School of **Natural and Applied Sciences** _____

Prof. Dr. Gönül Turhan Sayan
Head of Department, **Electrical and Electronics Engineering** _____

Prof. Dr. Gülbin Dural Ünver
Supervisor, **Electrical and Electronics Engineering Dept., METU** _____

Examining Committee Members:

Prof. Dr. S. Sencer Koç
Electrical and Electronics Engineering Dept., METU _____

Prof. Dr. Gülbin Dural Ünver
Electrical and Electronics Engineering Dept., METU _____

Prof. Dr. Özlem Aydın Çivi
Electrical and Electronics Engineering Dept., METU _____

Assoc. Prof. Dr. Lale Alatan
Electrical and Electronics Engineering Dept., METU _____

Prof. Dr. Birsen Saka
Electrical and Electronics Engineering Dept., Hacettepe Uni. _____

Date: 11.09.2015

I hereby declare that all information in this document has been obtained and presented in accordance with academic rules and ethical conduct. I also declare that, as required by these rules and conduct, I have fully cited and referenced all material and results that are not original to this work.

Name, Last Name : ERKAN ERSİN YILDIRIM

Signature :

ABSTRACT

PROPAGATION MODELS FOR HILLY TERRAIN BASED ON RAY OPTIC METHODS

Yıldırım, Erkan Ersin

M. S., Department of Electrical and Electronics Engineering

Supervisor: Prof. Dr. Gülbin Dural Ünver

September 2015, 127 pages

In RF propagation path loss modeling, numerical methods may not be useful since they require very long computation times because electrically very large objects may be located in the terrain. Ray optic methods such as Geometrical Optics (GO) or Geometrical Theory of Diffraction (GTD) are more commonly used in propagation problems as well as the empirical models. Although ray optics methods are designed for very high frequency applications, they provide quite accurate path loss estimations in hilly terrain including electrically very large obstructions.

In this thesis, ray optic methods are reviewed and applied to various different basic geometries. Computed results are compared with those obtained by the Longley-Rice model which is based on the use of empirical data. Weak and strong features of both ray optic methods and empirical methods are discussed. Finally, by using the results obtained previously, how to optimize the receiver parameters in order to obtain the maximum EM signal radiated by a transmitter in the hilly terrain is discussed.

Keywords: RF Propagation Path Loss Modeling, Terrain Elevation Modeling, Ray Optics, Geometrical Theory of Diffraction, Longley-Rice Model, Antenna Optimization, Received Signal Power Optimization

ÖZ

DAĞLIK ARAZİDE IŞIN BAZLI YÖNTEMLERE DAYANAN YAYILIM MODELLERİ

Yıldırım, Erkan Ersin

Yüksek Lisans, Elektrik Elektronik Mühendisliği Bölümü

Tez Yöneticisi: Prof. Dr. Gülbin Dural Ünver

Eylül 2015, 127 sayfa

Elektromanyetik yayılım modellemede, dalga boyuna göre çok büyük engellerin bulunabileceği dağlık alanlarda, nümerik metotlar hesaplama zamanları açısından yetersiz hale gelebilmektedir. Deneysel modellerin yanı sıra, geometrik optik (GO) teori ya da geometrik kırınım teorisi (GTD) gibi ışın bazlı yöntemler de sıkça kullanılmaktadır. Bu yöntemler çok yüksek frekanslı dalgalar için tasarlanmış olmakla birlikte, dalga boyuna göre çok büyük engellerin olduğu dağlık alanlarda, VHF ve UHF banttaki yayılım modellemelerinde de yeterli doğrulukta çözümler sunmaktadır.

Bu tezde, ışın bazlı metotlar incelenmiş ve çeşitli basit yapılara uygulanmıştır. Elde edilen sonuçlar deneysel olarak elde edilmiş olan Longley-Rice yayılım modeli sonuçlarla karşılaştırılmıştır. Hem teorik hem de deneysel metotların güçlü ve zayıf yönleri değerlendirilmiştir. Son aşamada ise, elde edilen bilgiler ışığında, dağlık bir alanda, alıcının vericiden yayılan EM dalgaları en verimli şekilde alabilmesi için; alıcı parametrelerinin nasıl seçilmesi gerektiği tartışılmıştır.

ANAHTAR KELİMELER: Elektromanyetik Yayılım Modelleme, Dağlık Arazi Modelleme, Işın Bazlı Yöntemler, Geometrik Kırınım Teorisi (GTD), Longley-Rice Metodu, Anten Optimizasyonu, Alınan Sinyal Gücü Optimizasyonu

To My Family

ACKNOWLEDGEMENTS

I would like to express my deepest thanks and gratitude to my supervisor Prof. Dr. Gülbin DURAL ÜNVER for her encouragement, guidance, advice and support throughout this study.

I also wish to thank to all my colleagues at ASELSAN, especially Ezgi KOÇ KARAKAŞ, Şeref Yaşar TEKİN and Mehmet Nazım BATUR, for their support, understanding and motivation.

My special appreciation goes to my mother Suna YILDIRIM, my father Hasan YILDIRIM and my sisters Esra Ezgi YILDIRIM and Dr. Sinem Esin YILDIRIM for their love, support, persistent confidence on me and understanding at all stages of my life. Without their presence, this thesis would not have been possible.

Last, but definitely not the least, I am very grateful to Aybüge ÇEKİNMEZ for her love, patience, understanding during this study, always believing in me and supporting in any case. Thank you for everything, thank you for always being there for me.

TABLE OF CONTENTS

ABSTRACT	v
ÖZ	vi
ACKNOWLEDGEMENTS	viii
TABLE OF CONTENTS	ix
LIST OF TABLES	xi
LIST OF FIGURES	xii
LIST OF ABBREVIATIONS	xviii
CHAPTERS	
1. INTRODUCTION	1
2. GEOMETRICAL THEORY OF DIFFRACTION	5
2.1 INTRODUCTION	5
2.2 GEOMETRICAL OPTICS	11
2.2.1 Basics of Geometrical Optics.....	13
2.2.1.1 Refractive Index	13
2.2.1.2 Snell's Law and Fresnel Equations	14
2.2.1.3 Fermat's Principle	15
2.2.1.4 Eikonal Surfaces and Eikonal Equation.....	19
2.2.2 Amplitude Relations in Geometrical Optics	22
2.2.3 Phase and Polarization Relations in Geometrical Optics	26
2.2.4 Surface Reflection Mechanisms.....	28
2.3 GEOMETRICAL THEORY OF DIFFRACTION	39
2.3.1 Amplitude, Phase and Polarization Relations in GTD.....	40
2.3.2 Straight Edge Diffraction of the Normally Incident Waves upon a Wedge	42
2.3.3 The Total Field Scattered by a PEC Wedge.....	44
2.3.4 The Diffraction Coefficient in GTD	50
2.4 ADVANTAGES OF GTD COMPARED TO GO.....	57

3. EVALUATION OF GTD BASED PROPAGATION MODELS	63
3.1 TERRAIN PROFILES ANALYZED BY USING GTD	64
3.1.1 A Mountain Modeled as a PEC Half-plane	65
3.1.2 A Mountain Modeled as a Wedge with a Nonzero Angle.....	82
3.2 LONGLEY-RICE MODEL IN HILLY TERRAIN.....	94
3.2.1 Input Parameters and the Details of Longley-Rice Model	95
3.2.2 Propagation Path Loss Calculations of the Longley-Rice Model ...	98
3.3 COMPARISON of MEASURED DATA AND RESULTS OF MODELS.....	101
3.3.1 Profile R1-0.5-T1 (Planar, Line-of-Sight Sloping Terrain).....	102
3.3.1.1 Operating Frequency 230 MHz, Terrain Profile R1-0.5-T1 ..	103
3.3.1.2 Operating Frequency 1846 MHz, Terrain Profile R1-0.5-T1	105
3.3.2 Profile R1-5-T5A (Abrupt Terrain, Beyond the Line-of-Sight)....	106
3.3.2.1 Operating Frequency 230 MHz, Terrain Profile R1-5-T5A...	108
3.3.2.2 Operating Frequency 4595 MHz, Terrain Profile R1-5-T5A.	110
4. OPTIMIZATION OF AN ANTENNA SYSTEM LOCATED ON A HILLY TERRAIN IN TERMS OF RECEIVER SIDE	113
5. CONCLUSION.....	122
REFERENCES	126

LIST OF TABLES

TABLES

Table 2-1 Existence of fields in Figure 2-22	44
Table 3-1 The Longley-Rice model parameters (from [27]).....	96
Table 3-2 The original identification of R1-0.5-T1 made by McQuate (from [29])	102
Table 3-3 The original identification of R1-5-T5A made by McQuate (from [29])	106

LIST OF FIGURES

FIGURES

Figure 2-1 Physical equivalent for scattering fields by a perfect electric conductor (PEC) (a) Actual problem (b) Physical equivalent (from [1]).....	8
Figure 2-2 Physical optics (PO) equivalent of a flat conducting infinite surface (from [1])	10
Figure 2-3 Two media whose refractive indices are n_1 and n_2 (from [11])	14
Figure 2-4 yz -plane at $x=x$ separates two different media	18
Figure 2-5 Primary and secondary wave front of a radiated wave (from [1]).....	19
Figure 2-6 Eikonal surfaces for plane (<i>top-left</i>), cylindrical (<i>top-right</i>) and spherical (<i>bottom</i>) waves (from [1])	21
Figure 2-7 Cross sectional areas along the travel of a spherical wave radiating from a point source (from [1]).....	22
Figure 2-8 Astigmatic tube of rays (a) Eikonal surface (b) Caustic Lines (from [1])	25
Figure 2-9 Parameters that can be defined for a reflecting surface (a) Normal section curves and principal planes (b) Principle radii of curvature (from [1]) ..	28
Figure 2-10 Reflection from a well-behaved surface (from [1]).....	29
Figure 2-11 Astigmatic tube of rays and principal radii of curvature of reflected and incident waves at a curved surface (from [1])	31
Figure 2-12 Reflection of a cylindrical field radiated from an infinite line (from [1])	33
Figure 2-13 An infinitely long z -directed, constant I_0 current electric line source above a finite width, infinite length PEC strip (from [1])	34

Figure 2-14 Far-zone approximation of $H_0^{(2)}(\beta\rho)$ (<i>real part</i>)	35
Figure 2-15 Far-zone approximation of $H_0^{(2)}(\beta\rho)$ (<i>imaginary part</i>)	35
Figure 2-16 Infinitely long z-directed electric line with incident and reflected paths at far-field	36
Figure 2-17 The α angle depends on h/w	37
Figure 2-18 The total field distribution of an infinitely long electric line source given in Figure 2-13, calculated by the code developed in MATLAB®	38
Figure 2-19 Oblique incidence diffraction from a curved edge (from [1]).....	40
Figure 2-20 Oblique incidence wedge diffraction from a straight edge (from [1])	41
Figure 2-21 Regions of a wedge diffraction.....	43
Figure 2-22 Regions of a wedge diffraction in coordinate system	43
Figure 2-23 Infinitely long line source shown in coordinate system	44
Figure 2-24 Infinitely long line source and PEC wedge	46
Figure 2-25 (a) Plane wave incidence (b) Cylindrical wave incidence	48
Figure 2-26 The ϕ – variation of the total E-field at $\rho = \lambda$ when the unity amplitude plane wave radiated from an electric line-source $\phi' = 30^\circ$ is incident upon a wedge.....	49
Figure 2-27 The ϕ – variation of the total H-field at $\rho = \lambda$ when the unity amplitude plane wave radiated from an magnetic line-source $\phi' = 30^\circ$ is incident upon a wedge.....	49
Figure 2-28 Incident diffracted field of plane wave upon a half-plane wedge	56
Figure 2-29 Reflected diffracted field of plane wave upon a half-plane wedge.....	57
Figure 2-30 Plane wave incidence with an angle of 30° upon a half-plane wedge	57
Figure 2-31 Normalized GO fields pattern for Figure 2-30	58

Figure 2-32 GO, diffracted and total (GTD) fields for Figure 2-30	59
Figure 2-33 An infinitely long line source above w – width finite strip	60
Figure 2-34 Angle definitions on the strip	60
Figure 2-35 Normalized total diffracted field of an infinitely long line source above w – width finite strip given in Figure 2-33 ($h = 0.5\lambda$ and $w = 2\lambda$).....	61
Figure 2-36 Total GO field and total (Diffracted + GO) field of for the geometry presented in Figure 2-33	61
Figure 3-1 Transmitter and receiver antennas on either side of a mountain modeled as PEC Half-Plane Wedge	66
Figure 3-2 Comparison between obstruction loss values by using Keller’s method and the UTD code developed in MATLAB [®] (<i>soft polarization</i>)	68
Figure 3-3 Comparison between obstruction loss values by using Keller’s method and the UTD code developed in MATLAB [®] (<i>hard polarization</i>).....	68
Figure 3-4 Incident shadow boundary for the case $d_{Tx} = d_{Rx} = h = 5\lambda$ and $h_{Tx} = 0$	69
Figure 3-5 Obstruction loss calculated by both Keller’s method and the code developed in MATLAB [®] (<i>soft polarization</i>).....	71
Figure 3-6 Obstruction loss calculated by both Keller’s method and the code developed in MATLAB [®] (<i>hard polarization</i>).....	71
Figure 3-7 Configuration to examine the antenna height symmetry	72
Figure 3-8 Obstruction loss for both of the cases given in Figure 3-7 (<i>soft pol.</i>) ...	72
Figure 3-9 Configuration to examine the antenna distance symmetry	73
Figure 3-10 For Figure 3-9, loss calculated by UTD based MATLAB [®] code.....	74
Figure 3-11 For Figure 3-9, loss calculated by Keller’s formula	74
Figure 3-12 Other parameters when investigating the effect of obstruction height	75

Figure 3-13 Loss calculated by the code developed in MATLAB [®] (<i>soft pol.</i>).....	76
Figure 3-14 Loss calculated by the code developed in MATLAB [®] (<i>hard pol.</i>).....	76
Figure 3-15 Configuration to examine the effect of receiver parameters, d_{Rx} and h_{Rx}	77
Figure 3-16 Obstruction loss vs. d_{Rx} calculated by MATLAB [®] (<i>soft pol.</i>).....	78
Figure 3-17 Obstruction loss vs. d_{Rx} calculated by MATLAB [®] (<i>hard pol.</i>).....	78
Figure 3-18 Receiver antenna distance optimization for the case-1 given in Figure 3-15 in order to minimize the total loss.....	79
Figure 3-19 Obstruction loss vs. h_{Rx} calculated by MATLAB [®] (<i>soft pol.</i>).....	80
Figure 3-20 Obstruction loss vs. h_{Rx} calculated by MATLAB [®] (<i>hard pol.</i>).....	81
Figure 3-21 Total loss for the case-2 given in Figure 3-15 for soft polarization	81
Figure 3-22 Transmitter and receiver antennas on either side of a mountain that can be modeled as a wedge that has a nonzero wedge angle.....	82
Figure 3-23 Configuration to investigate the effect of obstruction height.....	84
Figure 3-24 Loss calculated by MATLAB [®] vs. h for different WA (<i>soft pol.</i>).....	85
Figure 3-25 Loss calculated by MATLAB [®] vs. h for different WA (<i>hard pol.</i>).....	85
Figure 3-26 All height values are fixed only WA angle differs.....	86
Figure 3-27 Loss calculated by MATLAB [®] vs. WA for Figure 3-26 (<i>soft pol.</i>).....	87
Figure 3-28 Loss calculated by MATLAB [®] vs. WA for Figure 3-26 (<i>hard pol.</i>) ...	87
Figure 3-29 Configuration to examine the effect of d_{Rx} and h_{Rx} with 45° wedge ..	88
Figure 3-30 Soft and hard obstruction loss vs. d_{Rx} with WA=45°	89
Figure 3-31 Soft polarization obstruction loss vs. d_{Rx} with WA=0° and 90°	90
Figure 3-32 Hard polarization obstruction loss vs. d_{Rx} with WA=0° and 90°	90

Figure 3-33 Obstruction loss vs. h_{Rx} for the case-2 given in Figure 3-29 (<i>soft pol.</i>)	92
Figure 3-34 Obstruction loss vs. h_{Rx} for the case-2 given in Figure 3-29 (<i>hard pol.</i>)	92
Figure 3-35 Total loss for the case-2 given in Figure 3-29 for soft polarization	93
Figure 3-36 Obstruction loss vs. h_{Rx} for the case-2 given in Figure 3-29 for different wedge angles for soft polarization	93
Figure 3-37 Interface of the Longley-Rice based propagation modelling program	98
Figure 3-38 Obstruction loss vs. obstruction height (h) for Figure 3-37.....	99
Figure 3-39 Obstruction loss vs. receiver antenna distance for Figure 3-37.....	100
Figure 3-40 Obstruction loss vs. receiver antenna height for Figure 3-37.....	100
Figure 3-41 Exact and linear elevation data for profile R1-0.5-T1	103
Figure 3-42 Path losses vs. receiver antenna height at 230 MHz for R1-0.5-T1 ..	104
Figure 3-43 Path losses vs. receiver antenna height at 1846 MHz for R1-0.5-T1	105
Figure 3-44 The exact R1-5-T5A terrain profile and linearization of terrain	107
Figure 3-45 Coordinate system and coordinates of linear terrain	108
Figure 3-46 Embedded terrain profile R1-5-T5A at the interface of the program	109
Figure 3-47 Path losses vs. receiver antenna height at 230 MHz for R1-5-T5A ..	110
Figure 3-48 Path losses vs. receiver antenna height at 4595 MHz for R1-5-T5A	111
Figure 4-1 A simple antenna system where the receiver in diffraction region	113
Figure 4-2 Representation of parallel polarization of an antenna and 3-D hill.....	115
Figure 4-3 Path losses vs. receiver antenna height at 1846 MHz for R1-0.5-T1 ..	117
Figure 4-4 Loss vs. d_{Rx} when $h_{Tx} = h_{Rx} = 25\lambda$, $h = 50\lambda$ and $d_{Tx} = 1000\lambda$	118

Figure 4-5 Total loss vs. d_{Rx} for $h_{Tx} = h_{Rx} = 25\lambda$, $h = 50\lambda$ and $d_{Tx} = 1000\lambda$ 119

Figure 4-6 Total path loss vs. d_{Rx} for $h_{Tx} = h_{Rx} = 25\lambda$, $h = 50\lambda$ and $d_{Tx} = 500\lambda$

..... 119

Figure 4-7 Total path loss vs. d_{Rx} for $h_{Tx} = h_{Rx} = 25\lambda$, $h = 50\lambda$ and $d_{Tx} = 2000\lambda$

..... 120

LIST OF ABBREVIATIONS

E	: electric field intensity vector
EFIE	: electric field integral equations
GO	: geometrical optics
GSM	: Global System for Mobile Communications
GTD	: geometrical theory of diffraction
IE	: integral equations
ISB	: incident shadow boundary
MFIE	: magnetic field integral equations
MoM	: method of moments
MT	: modal techniques
PEC	: perfect electric conductor
PO	: physical optics
PTD	: physical theory of diffraction
RF	: radio frequency
RSB	: reflection shadow boundary
UTD	: uniform theory of diffraction
5G	: fifth generation mobile networks

CHAPTER 1

INTRODUCTION

Communication is an inseparable part of the daily lives of today's people. Depending on the increasing functionality of mobile devices, people desire to use the mobile devices everywhere. The mobile device can either be an old fashion analog handheld radio or a cellular phone that possesses the capacity to communicate by using 5G, making no difference in the sense that all the mobile devices use radio frequency (RF) signals to transmit or receive the voice or the data. Therefore to meet the communication needs of people, it is important to estimate the propagation characteristics of the RF signals. Communication has also a very important role about the public safety services like police, fire and rescue, ambulance and medical emergency all around the world. Having the capability to communicate in rural areas is as vital as in urban areas for these services.

Although using the numerical electromagnetic methods such as Method of Moments (MoM) is feasible to estimate the field distribution in a small area, such as in the case of indoor coverage of a room, it is not possible for thousands of meters distances including mountains whose elevations may be in the order of thousands of meters. Therefore alternative techniques have to be developed in order to model the propagation characteristics of RF signals in terms of theoretical models, empirical models or combinations of them.

First technique presented in this thesis to model the RF propagation uses electromagnetic theory, predominantly. One of the famous approaches mainly based on the theory is using *ray optics* models. Since these techniques are originally

developed in order to model the behavior of light, they are called as *ray optics* methods. Then it is realized that if the frequency is sufficiently high, they also provide acceptable outcomes for RF waves as well [1]. This thesis is mainly focused on *geometrical optics* (GO) and *geometrical theory of diffraction* (GTD) which is an extension of GO. It is first originated by Keller [2], [3] and Kouyoumjian and Pathak developed it in [4], [5], [6] and [7].

The second approach for modeling RF propagation utilizes the empirical data and measurements, predominantly. Although there are lots of empirical models, this thesis is focused on a famous and common one, *Longley-Rice propagation model*. It is mainly based on the RF levels measured at Gunbarrel Hill, Fritz Peak, North Table Mountain in U.S and repeated measurements in forests, flat areas etc. This model is offered by Longley and Rice in [26]. Also, there are other empirical propagation path loss models such as Hata, Okumura-Hata and COST-231 Hata which are not discussed in this thesis since they are mostly developed for urban areas.

In this thesis study, GTD is studied in a detailed way to represent the ray models. Then a code is developed in MATLAB[®] to simplify the complex calculations of GTD. Then for various types of terrain profiles that represent the real life examples are examined by this code. Similar terrain profiles are also studied by Longley-Rice propagation model. By comparing the GTD and Longley-Rice method results with the real life measurements, the strengths and weaknesses of both approaches are investigated. Then by taking into account the experiences gained by these studies, a receiver antenna height and location optimization is offered in order to improve the communication performance in a hilly terrain area. Finally, the comments, assumptions and the future works are described. Within this context,

- In Chapter 2, first it is explained why traditional methods are not sufficient and numerical methods are not feasible for propagation problems and ray optics methods are necessary. Then the theoretical ray optics methods are

described in a detailed way. Especially, the GO and GTD methods are discussed. It is shown by examples that diffraction mechanisms in GTD improve GO results.

- In Chapter 3, the terrain profiles that represent the real life propagation paths are studied by GTD and Longley-Rice models. Results of these two approaches are compared with the measured data from real life. And the strengths and weaknesses of both approaches are examined.
- In Chapter 4, by the help of the obtained theoretical results, a receiver antenna height and location optimization is offered in order to improve the communication performance in a hilly terrain area.
- In Chapter 5, overall results of this thesis are discussed. And also the expected and unexpected deviations are described and possible reasons of the deviations are investigated. Finally, the assumptions are the factors which are taken into account in thesis are emphasized. The possible future works about these assumptions and the parameters ignored are briefly described.

CHAPTER 2

GEOMETRICAL THEORY OF DIFFRACTION

2.1 INTRODUCTION

To solve propagation problem in a propagation medium, it is necessary to solve field distributions in the medium. One of the sources of the total received field is directly propagated waves between transmitter and receiver. However, for the most of the situations in the real life, there may be scatterers between the source and the receiver; therefore, scattered fields should be taken into account in addition to the direct fields to calculate the total received field. To solve electromagnetic radiating and scattering problems, there are different approaches available in the literature. Image theory, modal techniques (MT), integral equations (IE), physical optics (PO), geometrical optics (GO) are some of the well-known approaches in order to analyze such electromagnetic problems. However, due to the restrictions of real life, it is not easy to apply these theoretical approaches to the solutions of practical problems [1]. The restrictions and deficiencies of the above approaches are given in the introduction part of this chapter and also it is explained why the diffraction theory is, one of the most powerful tools to analyze wave propagation. Diffraction theory that covers both physical theory of diffraction (PTD) and geometrical theory of diffraction (GTD) is discussed in detail in this chapter.

The restrictions about image theory, model techniques (MT), integral equations (IE), physical optics (PO) and geometrical optics (GO) are given roughly in this part.

Well-known restrictions about image theory are assuming the scattering surface to be flat and infinite, at least, electrically very large, assuming the conductivity of the scattering surface is infinite. Some approximations should be made about the surface since there is not such a flat scattering surface in the real life. However, these approximations are not quite accurate and the solution is valid only above the interface. Therefore, although image theory can be useful to analyze some parts of the complex problems, it is clear that it is not enough to analyze the complete problem.

In order to analyze electromagnetic characteristics of an object by using modal techniques (MT), it is necessary to represent the object and the environment by orthogonal curvilinear coordinate systems [1]. Orthogonality emphasizes the fact that all the unit vectors in a curvilinear coordinate system are perpendicular to one another. However, it is not possible to describe all the objects in nature by using orthogonal curvilinear coordinate systems. Moreover, in modal techniques the solution is found in the form of infinite series by the help of the boundary conditions. When the size of the object is larger than about a wavelength, convergence problems of the infinite series will be encountered. Therefore, in order to apply the modal solutions to an electromagnetic problem like scattering or propagating, approximate representations of the object or medium are generally used. Modal solution requires complex mathematical calculations that cannot be applied for large distances in terms of wavelength. For example, a typical GSM system transmits at 1 GHz and wavelength is smaller than 1 meter. However, the coverage area of a GSM base station is in the order of kilometers. Therefore, using modal techniques in real life propagation problems is almost impossible.

Although assuming the objects are infinitely long makes the required calculations encountered in an electromagnetic scattering problem easier; in practice the sizes of the objects are always finite. Therefore, it is very useful to model real-life problem by some mathematical equations. Such a mathematical model is called integral equation (IE) technique. In this technique, the unknown induced current distribution

on an arbitrary shaped object is a part of the integral equation. Generally, integral equations are solved by using numerical techniques, such as Method of Moments (MoM). After solving the current density on an object, it is possible to analyze the scattering or radiating characteristics of that object. Although arbitrary shapes can be analyzed in this technique, the numerical computations require powerful computers. Furthermore, if the sizes of the objects are too many wavelengths, the memory capacities of the available computers are not sufficient to use this technique in order to solve electromagnetic scattering and radiating problems. Therefore, this technique is generally more useful for the design of electromagnetic devices whose dimensions are comparable with the operating frequency, for example, antennas or filters. This technique is not useful for propagation problems due to the given reasons.

As mentioned above, there are some deficiencies of well-known methods; therefore, they may not be used to solve propagation problems. These deficiencies are based on the fact that the sizes of the objects at the earth surface like mountains are generally electrically large. That means the dimensions of these objects are greater than the wavelength of the operating frequency. Therefore, when the sizes of the objects are too many wavelengths like in the case of the propagation medium at the earth surface, another practical approach is necessary. Since it is harder to solve such problems mathematically, high-frequency asymptotic techniques can be used. The two most common techniques of analyzing the radiating or scattering characteristics of objects whose dimensions are too many wavelengths are *geometrical theory of diffraction* (GTD) and *physical theory of diffraction* (PTD).

Although GTD and PTD are based on different electromagnetic theorems, in the applications, both give similar results. Another similarity between PTD and GTD is that both are improved versions of former theorems. GTD is first originated by Keller [2], [3] and Kouyoumjian and Pathak developed it in [4], [5], [6] and [7]. GTD improves classical *geometrical optics* (GO) theorem by introducing the diffraction mechanism. This chapter mainly discusses GO and GTD in detail,

however; for the sake of completeness, a brief description of PTD is also given in this chapter.

Like GTD, the PTD, introduced by Ufimtsev in [8], [9] and [10]; includes some extensions additional to a classical electromagnetic theorem, *physical optics* (PO).

In classical PO, the scattering of perfect electric conductor (PEC) obstacle is analyzed. The original problem is given in Figure 2-1. If the obstacle is removed, the radiated fields would be \vec{E}_1 and \vec{H}_1 . By using classical calculation methods, for example, by using auxiliary vector potentials \vec{A} and \vec{F} , it is assumed that both \vec{E}_1 and \vec{H}_1 can be found. The scattered fields are \vec{E}^s and \vec{H}^s . Therefore the total field outside the obstacle (\vec{E} and \vec{H}) is given as

$$\vec{E} = \vec{E}_1 + \vec{E}^s \quad (2.1)$$

$$\vec{H} = \vec{H}_1 + \vec{H}^s \quad (2.2)$$

In Figure 2-1b, physical equivalent of the actual problem is given. Since this theorem aims to find the scattered fields from PEC and the scattering can only be observed outside the PEC, the fields inside the PEC are not important. Therefore, to simplify problem, the fields inside the PEC are taken as $-\vec{E}_1$ and $-\vec{H}_1$.

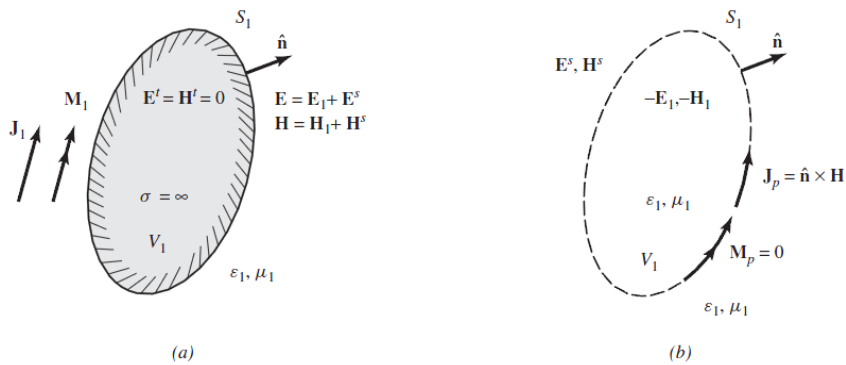


Figure 2-1 Physical equivalent for scattering fields by a perfect electric conductor (PEC) (a) Actual problem (b) Physical equivalent (from [1])

In the equivalent problem, the permittivity and permeability of both mediums (inside and outside of the PEC) are the same. It also simplifies the problem. Since PEC is removed at the equivalent problem; actually, there is no real boundary. Since PEC is removed, the source of the scattered fields is also removed. However, two fictitious sources are added to equivalent problems in order to obtain exactly the same scattered fields in the case of PEC exists. These two fictitious sources are magnetic and electric current densities over the boundary S_I . Magnetic current density $\vec{\mathbf{M}}_p$ and electric current density $\vec{\mathbf{J}}_p$ are given In Figure 2-1b. By using boundary conditions,

$$\vec{\mathbf{M}}_p = -\hat{\mathbf{n}} \times (\vec{\mathbf{E}} - \vec{\mathbf{E}}^t) = -\hat{\mathbf{n}} \times \vec{\mathbf{E}} = -\hat{\mathbf{n}} \times (\vec{\mathbf{E}}_1 + \vec{\mathbf{E}}^s) = 0 \quad (2.3)$$

$$\vec{\mathbf{J}}_p = \hat{\mathbf{n}} \times (\vec{\mathbf{H}} - \vec{\mathbf{H}}^t) = \hat{\mathbf{n}} \times \vec{\mathbf{H}} = \hat{\mathbf{n}} \times (\vec{\mathbf{H}}_1 + \vec{\mathbf{H}}^s) \quad (2.4)$$

In Eqn. (2.3) and Eqn. (2.4), $\vec{\mathbf{H}}^t$ and $\vec{\mathbf{E}}^t$ fields are zero, since the field inside the PEC is zero. Therefore, fictitious magnetic current density $\vec{\mathbf{M}}_p$ and electric current density $\vec{\mathbf{J}}_p$ can be represented in terms of tangential component of total fields $\vec{\mathbf{E}}$ and $\vec{\mathbf{H}}$. And these fictitious sources give exactly the same scattered field outside the boundary S_I . Another important point in these equations is that there is no need to define $\vec{\mathbf{M}}_p$; in other words, $\vec{\mathbf{J}}_p$ is enough according to the uniqueness theorem [1].

The equivalent electric current density, $\vec{\mathbf{J}}_p$, is also found in terms of an unknown quantity $\vec{\mathbf{H}}$, where $\vec{\mathbf{H}}$ is the sum of $\vec{\mathbf{H}}^s$ and $\vec{\mathbf{H}}_1$ (It is assumed that $\vec{\mathbf{H}}_1$ is known). On the other hand, at the beginning of the problem, the aim was to solve unknown $\vec{\mathbf{H}}^s$ and $\vec{\mathbf{E}}^s$. Therefore, physical equivalent does not seem to simplify the problem. However, representing the problem as equivalent current densities provides to use some numerical methods, electric and magnetic field integral equations, called as EFIE and MFIE, respectively. Another advantage of physical equivalent is that the

equivalent permittivity and permeability are same everywhere. Therefore, using auxiliary vector potentials $\vec{\mathbf{A}}$ and $\vec{\mathbf{F}}$ is possible in Figure 2-1b, unlike Figure 2-1a.

If the PEC is electrically very large and if it could be assumed as infinite, as it is given in Figure 2-2, tangential component of the scattered field, $\vec{\mathbf{H}}^s$, is equal to tangential component of the $\vec{\mathbf{H}}_1$ field. The most important advantage of using physical equivalent lies in this assumption.

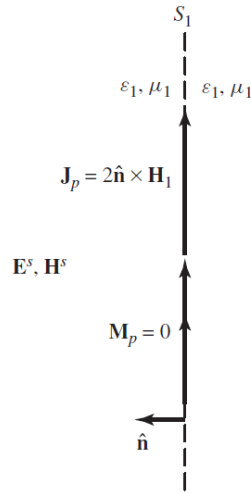


Figure 2-2 Physical optics (PO) equivalent of a flat conducting infinite surface
(from [1])

By using this assumption, one can rewrite Eqn. (2.4) as

$$\vec{\mathbf{J}}_p = \hat{\mathbf{n}} \times \vec{\mathbf{H}} = \hat{\mathbf{n}} \times (\vec{\mathbf{H}}_1 + \vec{\mathbf{H}}^s) = 2\hat{\mathbf{n}} \times \vec{\mathbf{H}}_1 \quad (2.5)$$

Therefore, the fictitious electric field current density is written in terms of a known field parameter, $\vec{\mathbf{H}}_1$. However, it should be pointed out that the approximations and assumptions in PO theorem may cause wrong results due to the degree of complexity of scattering object. As mentioned before, *Physical theory of diffraction* (PTD) is a developed version of classical PO theorem which is discussed in this chapter. Ufimtsev examined that the fringing field calculated in classical PO

approach does not satisfy the reciprocity principle. Therefore, to overcome this problem, he suggested adding fringe currents into the classical PO approach to explain diffraction mechanism at edges of different types of objects like, wedge, disc, finite length cylinder etc [8]. The details of the studies made by Ufimtsev can be found in the literature; however, they are beyond the scope of this thesis.

In the introduction part, the deficiencies of the classical theorems are explained and high frequency asymptotic techniques are suggested. These techniques are PTD and GTD. PTD was summarized with its earlier version PO up to this point in this chapter. Similar to PTD, GTD is also an extension of a classical approach, *geometrical optics* (GO). Since GTD is the main concern of this chapter, GTD and GO deserves a detailed discussion.

2.2 GEOMETRICAL OPTICS

As mentioned before, it is difficult to apply classical theorems when the objects in the problem are arbitrary shaped or electrically very large. Because arbitrary shaped objects cannot be easily represented by orthogonal curvilinear systems and the solution of scattering problem that involves electrically very large objects may not converge due to the fact that modal solutions are generally in the form of infinite series. Numerical studies might aid for the solution. For example, in *integral equation* (IE) method, the solution is generally achieved by using MoM. However, for large scaled problems like propagation in a terrain, this solution requires a lot of time and large computation memories. Therefore, when the object is electrically large, diffraction mechanism is quite useful.

Diffraction at high frequency depends on:

- Geometrical properties of the object at diffraction point
- The properties of the incident field: the amplitude, phase and polarization

In ray optics, the phase of the field is the product of optical length measured from a reference point and the wave number of the medium. With the appropriate units, it can be written as,

$$\textit{Phase} \text{ [rad]} = \textit{Optical length} \text{ [m]} \times k \text{ [rad / m]} \quad (2.6)$$

Phase jumps due to the caustics should be taken into account in addition to Eqn. (2.6). The details of caustics will be discussed later in this chapter but it is simply a line or a point through that all the rays of a wave pass. Also when calculating the phase difference of a field according to a reference point, one can use a simple principle about rays. The rays follow a path that is always an extremum from one point to another point. A well-known fact, light travels in straight paths, is a result of this principle. However this is actually valid only if the medium is homogenous. In inhomogeneous medium, the ray is curved.

Similar to the reflection coefficient, a diffraction coefficient is defined in the diffraction problems. Diffraction coefficient is a dyadic for electromagnetic scattering problems. Change in the value of the amplitude of the incident field can be calculated by using conservation of energy principle. Therefore, a dyadic diffraction coefficient and attenuation coefficient are defined for the field on a diffracted ray.

The main concern of this chapter is to calculate attenuation and diffraction coefficients of a wedge shaped object. It is known that dealing with complex problems requires dividing the problem into some well-known canonical problems. From this point of view, wedge has priority at this study; because, landform which includes complex hills or mountains can be generally represented by using the wedge shaped objects. The final solution of these types of complex problems will also be the superposition of the well-known solutions of the wedge diffraction problems. Also, it is assumed that wedge surface is PEC. This is an acceptable assumption due to the fact that the surface of the earth behaves as PEC for the

frequency bands commonly used in practical communication systems such as VHF and UHF.

2.2.1 Basics of Geometrical Optics

Geometrical optics (GO) is also called as *ray optics* since it is based on ray phenomena. It is originally developed to analyze the propagation of light. It is shown that if the frequency is high enough, the wave nature of the light may not be taken into account. Therefore, it is assumed that the electromagnetic waves transport energy according to the rules of ray concept. It is shown that if the object is too large according to the operating frequency; GO approach gives sufficiently accurate results and does not require corrections.

Since in GO theorem, electromagnetic fields is related to light; the summary of simple definitions and principles used in optics are given in the subsequent sections for the sake of completeness.

2.2.1.1 Refractive Index

Simply it can be said that the refractive index of a medium determines the propagation of light or any other radiation in that medium. The speed and wavelength of radiation is decreased by the amount of refractive index, n , if n is greater than 1. Vacuum has a refractive index of 1. Two well-known equations,

$$n = \frac{c}{v} \quad (2.7)$$

$$\lambda = \frac{\lambda_0}{n} \quad (2.8)$$

where c is the speed of light in vacuum, v is the speed of light in the medium. λ_0 is wavelength of light in vacuum and λ is wavelength of light in the medium.

2.2.1.2 Snell's Law and Fresnel Equations

Fresnel equations describe the behavior of light, when it travels between two media whose refractive indices are different. These equations were introduced by Augustin-Jean Fresnel, a French engineer and physicist, details are given in [11].

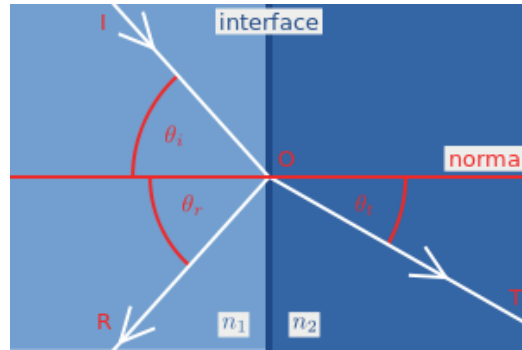


Figure 2-3 Two media whose refractive indices are n_1 and n_2 (from [11])

When the light meets a medium, whose refractive index is different, some of the light is reflected and some of the light is refracted. The polarization of the incident light wave is one of the most important parameters to determine the behavior of the incident light wave. There are two different polarizations: *s-polarization* and *p-polarization*. One can represent the polarization of any light wave by superpositioning it in terms of the above two polarized light waves. The incident, reflected and refracted waves define a plane. If the incident light is perpendicular to this plane according to its electric field, the incident field is called as s-polarized. Otherwise, its electric field is parallel to this plane, and the incident wave is called as p-polarized. The notation is similar to the vertical and horizontal polarization widely used electromagnetic propagation problems.

Very-well known angle relations given in Snell's Law are:

$$\theta_i = \theta_r \quad (2.9)$$

$$\frac{\sin \theta_i}{\sin \theta_t} = \frac{n_2}{n_1} \quad (2.10)$$

Also the ratio of the reflected power to the incident power is called as reflectance R, and the ratio of the refracted power to the incident power is called as transmittance T. Unlike angle relations, the power relations depend on the polarization.

The reflectance for s-polarized light is given as

$$R_s = \left| \frac{n_1 \cos \theta_i - n_2 \cos \theta_t}{n_1 \cos \theta_i + n_2 \cos \theta_t} \right|^2 \quad (2.11)$$

The reflectance for p-polarized light is given as

$$R_p = \left| \frac{n_1 \cos \theta_t - n_2 \cos \theta_i}{n_1 \cos \theta_t + n_2 \cos \theta_i} \right|^2 \quad (2.12)$$

It is not necessary to define transmittance since the sum of the reflectance and transmittance gives unity due to the conservation of energy.

$$T_s = 1 - R_s \quad (2.13)$$

$$T_p = 1 - R_p \quad (2.14)$$

Another important principle that is very useful to discover the geometrical optics is Fermat's principle.

2.2.1.3 Fermat's Principle

Fermat's principle denotes that the light prefer to travel from point A to B in a path such that it takes the least time to travel among all other possible paths. If the medium is homogenous, the light travels in a straight path and it corresponds to the

shortest path and least time. Although this behavior of the light in the homogenous medium was described very well, how the light travels in an inhomogeneous medium had not known until Pierre de Fermat, a French mathematician. Actually, Fermat's principle is not an independent approach; for example, it can be proved by using Huygens' Principle.

The mathematical expression of the Fermat's principle is given in the following parts. An electromagnetic wave travels from point A to B at a time T, which can be expressed as:

$$T = \int_{t_0}^{t_1} dt = \int_{t_0}^{t_1} \frac{c}{c} \frac{v}{v} dt = \frac{1}{c} \int_{t_0}^{t_1} \frac{c}{v} \frac{ds}{dt} dt = \frac{1}{c} \int_A^B n ds \quad (2.15)$$

where c is the speed of light in free space, ds is an infinitesimal distance along path and v is the speed of electromagnetic wave in that medium, which is equal to ds/dt . Also it was given in Eqn. (2.7) $n = c/v$.

Optical path length from A to B in a medium can be defined as multiplication of physical length from A to B and the refractive index of that medium. As a mathematical expression, the optical path length, S, can be written as

$$S = \int_A^B n ds \quad (2.16)$$

Combining Eqn. (2.15) and Eqn. (2.16) gives the relation between time and optical length which is given in Eqn. (2.17):

$$S = cT \quad (2.17)$$

Although the final version is not submitted by Fermat, modern Fermat's principle says that:

“The optical length of the path which is followed by a light from A to B, is an extremum (usually a minimum) and the optical length can be defined as the physical length multiplied by the refractive index of that medium.”

By the help of the calculus of variations context, Fermat's principle defined above can be summarized as

$$\delta \int_{P_1}^{P_2} n(s) ds = 0 \quad (2.18)$$

where δ represents *variational differential* and the remaining part is simply optical length in Eqn. (2.18).

The mathematical expression of Fermat's principle in Eqn. (2.18) states that if the medium is homogenous, $n(s) = n = \text{constant}$, the paths are straight lines. In other words, Fermat's principle states that in a homogenous medium the light can travel in the shortest time between P_1 and P_2 by only following a straight path. As mentioned above, the fact that the smallest length between point P_1 and P_2 is simply a straight line is one of the well-known axioms at math since ancient times. But the main contribution of Fermat's principle to the literature is about inhomogeneous mediums, where the reflection and refraction mainly occur.

Snell's law can be proved by using Fermat's principle. In Figure 2-4, the light travels from Medium1 to Medium 2. yz -plane at $x=x$ separates Medium 1 and 2. According to the Fermat's principle, the derivative of time with respect to x has to be zero as a result of Eqn. (2.18).

Let the velocity of the wave in Medium 1 be v_1 and in Medium 2 be v_2 . Therefore, $v_1 = c/n_1$ and $v_2 = c/n_2$ can also be written.

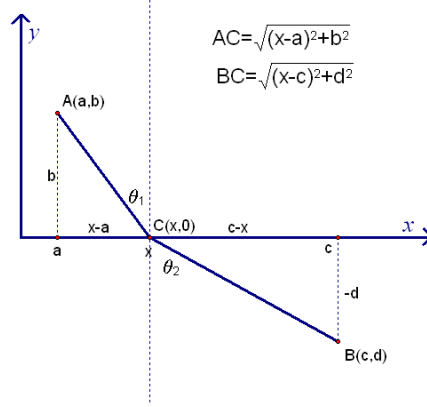


Figure 2-4 yz-plane at $x=x$ separates two different media

Therefore,

$$\frac{dT}{dx} = \frac{d(T_1 + T_2)}{dx} = 0 \quad (2.19)$$

$$T_1 = \frac{\sqrt{(x-a)^2 + b^2}}{v_1} \quad \text{and} \quad T_2 = \frac{\sqrt{(c-x)^2 + d^2}}{v_2} \quad (2.20)$$

$$\frac{d(T_1 + T_2)}{dx} = \frac{1}{\cancel{2}} \frac{\cancel{2}(x-a)}{\sqrt{(x-a)^2 + b^2}} \frac{1}{v_1} - \frac{1}{\cancel{2}} \frac{\cancel{2}(c-x)}{\sqrt{(c-x)^2 + d^2}} \frac{1}{v_2} = 0 \quad (2.21)$$

$$\begin{array}{ccc} \downarrow & & \downarrow \\ \sin \theta_1 & & \sin \theta_2 \end{array}$$

$$\frac{\sin \theta_1}{v_1} = \frac{\sin \theta_2}{v_2} \Rightarrow \frac{\sin \theta_1}{c/n_1} = \frac{\sin \theta_2}{c/n_2} \Rightarrow \boxed{\frac{\sin \theta_1}{\sin \theta_2} = \frac{n_2}{n_1}} \quad (2.22)$$

The same result is given in Eqn. (2.10). The relationship between these theorems can be summarized by the fact that Snell's Law can be derived from Fermat's principle, which is the mathematical requirement or mathematical representation of Huygens' Principle.

2.2.1.4 Eikonal Surfaces and Eikonal Equation

Wave front is the set of points having the same phase. It represents a surface in wave propagation. For the propagation of electromagnetic wave in a homogenous, lossless and isotropic medium, primary and secondary wave fronts are connected by straight lines for all points, as shown in Figure 2-5.

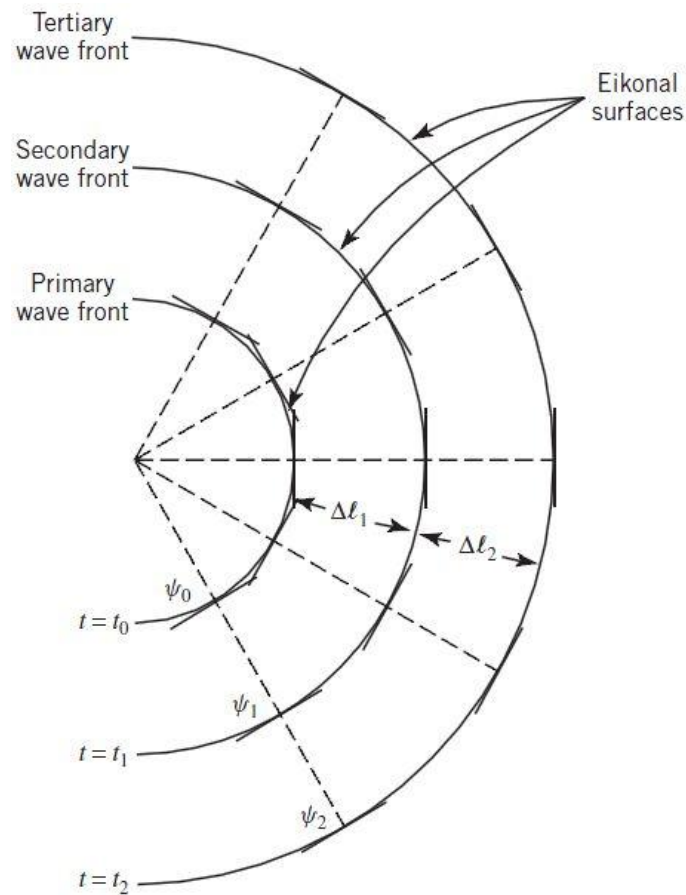


Figure 2-5 Primary and secondary wave front of a radiated wave (from [1])

It should be noticed here that the power intensity between two points located at successive wavefronts should be constant due to the conservation of energy flux.

If it is possible to define the relationship between the secondary wave front and primary wave front, the same equation can also be used to find out the relationship between power density at the secondary wave front and primary wave front.

The wave velocity is always perpendicular to wave front surfaces in both anisotropic and isotropic media. However, energy flow direction which is determined by ray velocity is different than the direction of the wave velocity in anisotropic medium.

In Figure 2-5, it is obvious that $\Delta\ell = v\Delta t$ and $v = c/n$. Also previously the relationship between phase and optical length is defined in Eqn. (2.6). Therefore,

$$\text{Phase Difference} = \frac{\phi}{c} \Delta\psi = \omega\Delta t = \phi \frac{\Delta\ell}{v} \Rightarrow \frac{\Delta\psi}{\Delta\ell} = \frac{c}{v} \quad (2.23)$$

Using Eqn. (2.7), Eqn. (2.24) can be written:
$$\frac{\Delta\psi}{\Delta\ell} = n \quad (2.24)$$

Also, it can be written

$$\Delta\psi = |\nabla\psi| \Delta\ell \quad (2.25)$$

Substituting Eqn. (2.24) into Eqn. (2.25) gives

$$\|\nabla\psi_n(x, y, z)\|^2 = \left\{ \frac{\partial\psi_n}{\partial x} \right\}^2 + \left\{ \frac{\partial\psi_n}{\partial y} \right\}^2 + \left\{ \frac{\partial\psi_n}{\partial z} \right\}^2 = n^2(s) \quad (2.26)$$

Eqn. (2.26) is known as *eikonal equation*. In [4], Kouyoumjian developed another approach to derive the eikonal equation. The wave equation for \mathbf{E} field given in Eqn. (2.27) is solved by using the asymptotic solution of Maxwell's equations and Luneberg-Kline asymptotic expansion for very large frequencies by Kouyoumjian.

$$\nabla^2 \vec{\mathbf{E}} + k^2 \vec{\mathbf{E}} = 0 \quad (2.27)$$

Also by the help of the Luneberg-Kline asymptotic expansion for very high frequencies, Kouyoumjian derives the same eikonal equation given in Eqn. (2.26).

The eikonal equation relates the rays and eikonal surfaces one-to-one. Therefore, it is sufficient to deal with only one of them to solve GO problems. It is also proved that, this approach can be extended to the low frequencies. Therefore, if the propagating wave is planar, eikonal surfaces are planar and perpendicular to the direction of wave. If the propagating wave is cylindrical, the eikonal surfaces are cylindrical and perpendicular to the cylindrical radial vectors. If the propagated wave is spherical, the eikonal surfaces are spherical and perpendicular to the spherical radial vectors. Visualization of eikonal surfaces are given in Figure 2-6.

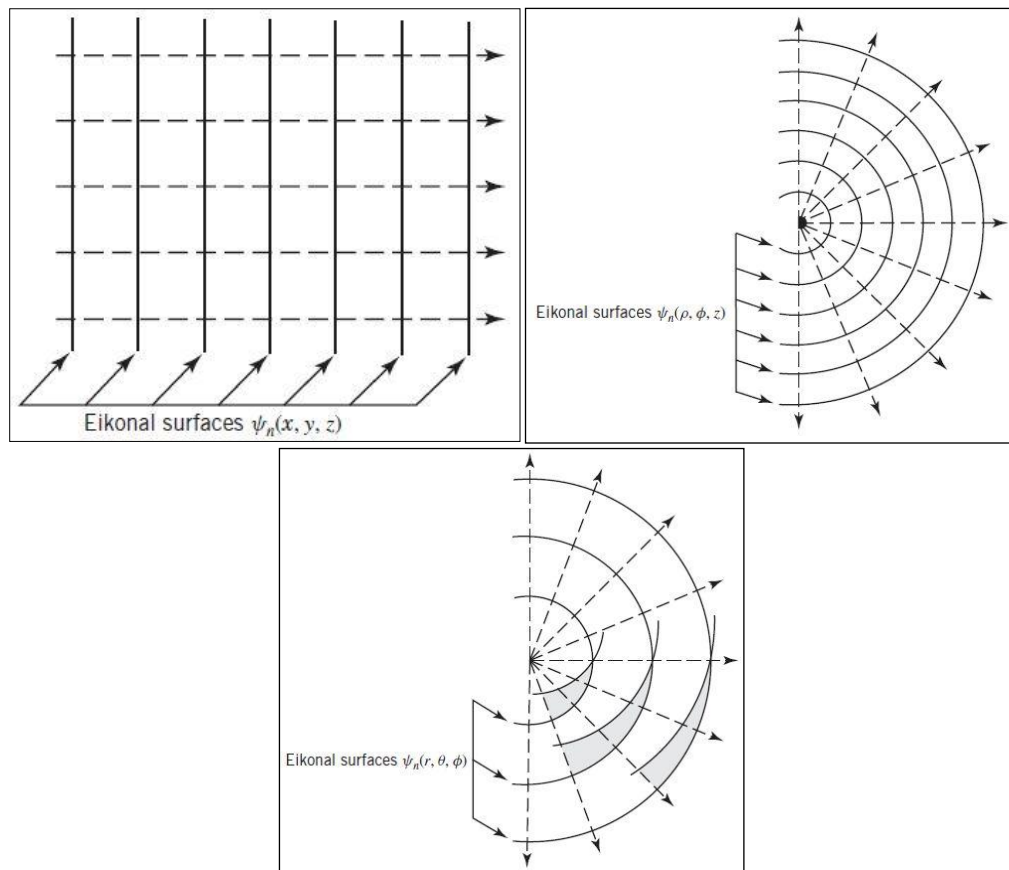


Figure 2-6 Eikonal surfaces for plane (*top-left*), cylindrical (*top-right*) and spherical (*bottom*) waves (from [1])

2.2.2 Amplitude Relations in Geometrical Optics

Conservation of energy, one of the fundamental theorems in physics, is also valid in GO. If an electromagnetic wave or light emanates from a point source, and it is assumed that it travels along spherical areas whose cross sections are given in Figure 2-7.

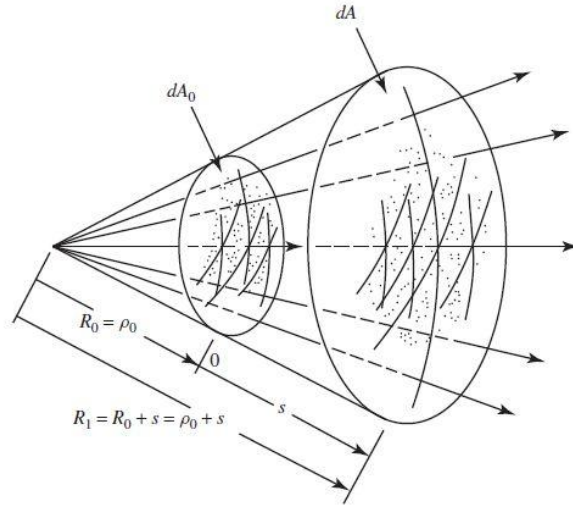


Figure 2-7 Cross sectional areas along the travel of a spherical wave radiating from a point source (from [1])

Since it is assumed that the electromagnetic waves propagate like straight rays, there is no ray such that it passes from dA_0 ; however, it does not reach to dA . Therefore, conservation of energy is satisfied between dA_0 and dA . The relationship between S_0 , the radiation density at $s=0$, and S , the radiation density at s is given in Eqn. (2.28).

$$S_0 dA_0 = S dA \Rightarrow \frac{S(s)}{S_0(0)} = \frac{dA_0}{dA} \quad (2.28)$$

As mentioned before, Eqn. (2.28) is only valid if there is no leakage field between dA_0 and dA . Also the relation between the peak values of $\vec{\mathbf{E}}$ field and radiation density S at far-zone is given in Eqn. (2.29).

$$S(r, \theta, \phi) = \frac{1}{2\eta} |\vec{\mathbf{E}}(r, \theta, \phi)|^2 = \frac{1}{2} \sqrt{\frac{\varepsilon}{\mu}} |\vec{\mathbf{E}}(r, \theta, \phi)|^2 \quad (2.29)$$

Since S is proportional to the square of the magnitude of the $\vec{\mathbf{E}}$ field, Eqn. (2.28) can be rewritten as Eqn. (2.30)

$$\frac{|\vec{\mathbf{E}}|^2}{|\vec{\mathbf{E}}_0|^2} = \frac{dA_0}{dA} \quad (2.30)$$

Eqn. (2.30) is a general formula valid for three cases: spherical, cylindrical and planar waves.

For spherical waves, according to Figure 2-7, Eqn. (2.30) can be rewritten as in the Eqn. (2.31). dA_0 and dA are pieces of a sphere; therefore, they should be proportional to radii of curvature of dA_0 and dA . Since wave fronts are spheres for this case, the radii of curvatures are simply the radius of sphere R_0 and R_1 . R_0 and R_1 correspond to ρ_0 and $\rho_0 + s$ in Figure 2-7, respectively.

$$\boxed{\frac{|\vec{\mathbf{E}}|}{|\vec{\mathbf{E}}_0|} = \sqrt{\frac{dA_0}{dA}} = \sqrt{\frac{4\pi R_0^2 / C_0}{4\pi R_1^2 / C_0}} = \frac{R_0}{R_1} = \frac{\rho_0}{\rho_0 + s}} \quad (2.31)$$

For cylindrical waves, Figure 2-7 does not perfectly fulfill the visualization since the wave front ratio proportional to R , not R^2 as in the case of spherical waves. The

concept is similar. So, for cylindrical waves, Eqn. (2.30) can be rewritten as in the Eqn. (2.32).

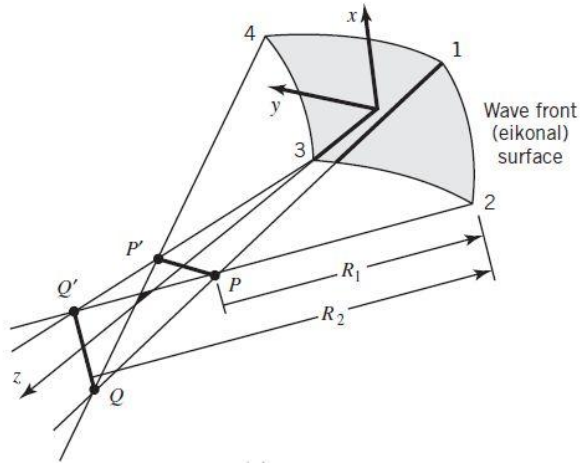
$$\boxed{\frac{|\vec{\mathbf{E}}|}{|\vec{\mathbf{E}}_0|} = \sqrt{\frac{dA_0}{dA}} = \sqrt{\frac{2\pi R_0 / C_1}{2\pi R_1 / C_1}} = \sqrt{\frac{R_0}{R_1}} = \sqrt{\frac{\rho_0}{\rho_0 + s}}} \quad (2.32)$$

For planar waves, it is clear that Eqn. (2.30) can be simplified as Eqn. (2.33)

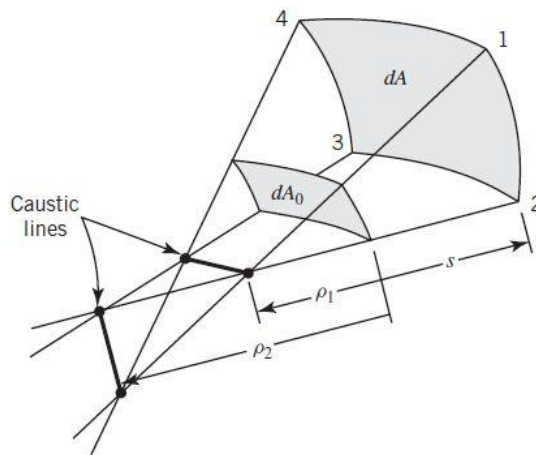
$$\boxed{\frac{|\vec{\mathbf{E}}|}{|\vec{\mathbf{E}}_0|} = 1} \quad (2.33)$$

Previously, Eqn. (2.30) is derived from the conservation of energy principle and Eqn. (2.31), (2.32) and (2.33) are three special cases for the wave fronts are spherical, cylindrical and planar. However, wave fronts do not have to be spherical, cylindrical or planar. Infinitely many different planes which include a line formed by a certain point on a sphere and the centre of the sphere can be selected. The intersections of these planes and sphere are circles. And the radii of these circles are all the same. In other words, the radius of curvature at a sphere is same for all planes. However, this is not valid for any eikonal surfaces. In Figure 2-8a, the wavefront or eikonal surface has the radius of curvature R_1 in the x - z plane and R_2 in the y - z plane. Since the wave front is not a partition of a sphere, $R_1 \neq R_2$ in this case. Since $R_1 \neq R_2$, the rays passing through the four corners of the wave front do not intersect at a single point. For example, rays 1 and 2 intersect at point P ; rays 1 and 2 intersect at point P' . Point P and P' are not same points. This is called as *astigmatic tube of rays*. The lines PP' and QQ' lines are called *caustics*.

If the wave front in Figure 2-8a, had been a partition of a sphere, the caustic would be a point. It would simply be the center of the sphere. The caustic is the focal point of all the rays passing through it. It may be a point like in the case of sphere, a line or a surface.



(a)



(b)

Figure 2-8 Astigmatic tube of rays (a) Eikonal surface (b) Caustic Lines (from [1])

According to Figure 2-8b; Eqn. (2.31), Eqn. (2.32) and Eqn. (2.33) can be written in general as in the form of Eqn. (2.34)

$$\boxed{\frac{|\vec{\mathbf{E}}|}{|\vec{\mathbf{E}}_0|} = \sqrt{\frac{dA_0}{dA}} = \sqrt{\frac{\rho_1 \rho_2}{(\rho_1 + s)(\rho_2 + s)}}} \quad (2.34)$$

The general formulation, given in Eqn. (2.34), actually turns into the

- Eqn. (2.31) if the wave front is spherical ($\rho_1 = \rho_2 = \rho_0$)
- Eqn. (2.32) if wave front is cylindrical ($\rho_1 = \infty, \rho_2 = \rho_0$ or $\rho_2 = \infty, \rho_1 = \rho_0$)
- Eqn. (2.33) if the wave front is planar ($\rho_1 = \rho_2 = \infty$)

Eqn. (2.34) relates the *magnitudes* of a high-frequency electromagnetic wave at consecutive wave fronts. This relation is derived from conservation of energy principle and it is very significant. Although the relation is also valid at lower frequencies, two more parameters should be taken into account in order to obtain the complete picture of operation at lower frequencies: *phase* and *polarization*

2.2.3 Phase and Polarization Relations in Geometrical Optics

Eqn. (2.34) should be developed by using the *Luneberg-Kline high frequency expansion* in order to cover phase and polarization parameters. Luneberg [12] and Kline [13] introduced an approach to apply the ray techniques of geometrical optics to the electromagnetic wave propagation.

Luneberg-Kline high frequency expansion is mainly based on the fact that $\vec{\mathbf{E}}$ field can be represented by infinite series as the following

$$\vec{\mathbf{E}}(\vec{\mathbf{R}}, \omega) = e^{-j\beta_0\psi(\vec{\mathbf{R}})} \sum_{m=0}^{\infty} \frac{\vec{\mathbf{E}}_m(\vec{\mathbf{R}})}{(j\omega)^m} \quad (2.35)$$

where $\vec{\mathbf{R}}$ = position vector

β_0 = phase constant for free-space

Substituting Eqn. (2.35) into the following homogenous wave equation

$$\nabla^2 \vec{\mathbf{E}} + \beta^2 \vec{\mathbf{E}} = 0 \quad (2.36)$$

and using the source-free Maxwell's equation,

$$\vec{\nabla} \cdot \vec{\mathbf{E}} = 0 \quad (2.37)$$

Luneberg [12] and Kline [13] proved that eikonal equation given in Eqn. (2.26) can be derived and the transport equation for first-order terms can be written in the following form

$$\frac{\partial \vec{\mathbf{E}}_0}{\partial s} + \frac{1}{2} \left\{ \frac{\nabla^2 \psi}{n} \right\} \vec{\mathbf{E}}_0 = 0 \quad (2.38)$$

Eqn. (2.38) is a functional relation used by Luneberg and Kline in order to obtain the $\vec{\mathbf{E}}$ field at point s in terms of the $\vec{\mathbf{E}}$ field at the reference point $s = 0$ according to Figure 2-8b.

$$\vec{\mathbf{E}}(s) = \underbrace{\vec{\mathbf{E}}'_0(0) e^{j\phi_0(0)}}_{\text{Field at reference point (s=0)}} \underbrace{\sqrt{\frac{\rho_1 \rho_2}{(\rho_1 + s)(\rho_2 + s)}}}_{\text{Spatial attenuation (divergence) factor}} \underbrace{e^{-j\beta s}}_{\text{Phase factor}} \quad (2.39)$$

where $\vec{\mathbf{E}}'_0(0)$ = field amplitude at reference point ($s = 0$)

$\phi_0(0)$ = field phase at reference point ($s = 0$)

It is possible to derive Eqn. (2.39) from Eqn. (2.34) by rewriting fields as vectors and adding a phase factor for the propagation wave from $s = 0$ to s . However, Luneberg-Kline expansion approach is more elegant. Although Eqn. (2.39) is a high-frequency approximation, it gives reliable results at lower frequencies. It predicts the $+\pi/2$ phase jumps at caustics, $s = -\rho_1$ and $s = -\rho_2$, since inside the root of the divergence factor changes sign at caustics and $\sqrt{-1} = j = e^{j\pi/2}$ is known.

Although Eqn. (2.39) has advantages, it also has deficiencies. At exact caustics points, $s = -\rho_1$ and $s = -\rho_2$, the field goes to the infinity; therefore, it should not be used or it should be modified at caustics. Also omitting high-order terms causes some calculation errors. However, more efficient other tools are developed rather than modifying geometrical optics to overcome this problem because there is no way to remove the discontinuities at incident or reflection shadow boundaries even if the higher order terms are taken into account.

2.2.4 Surface Reflection Mechanisms

The principles of geometrical optics can be used not only to calculate amplitude relations of propagating field but also calculate amplitude relations of reflected field from a surface. Previously it is mentioned that a surface may have different radii of curvature at different planes which intersect the surface.

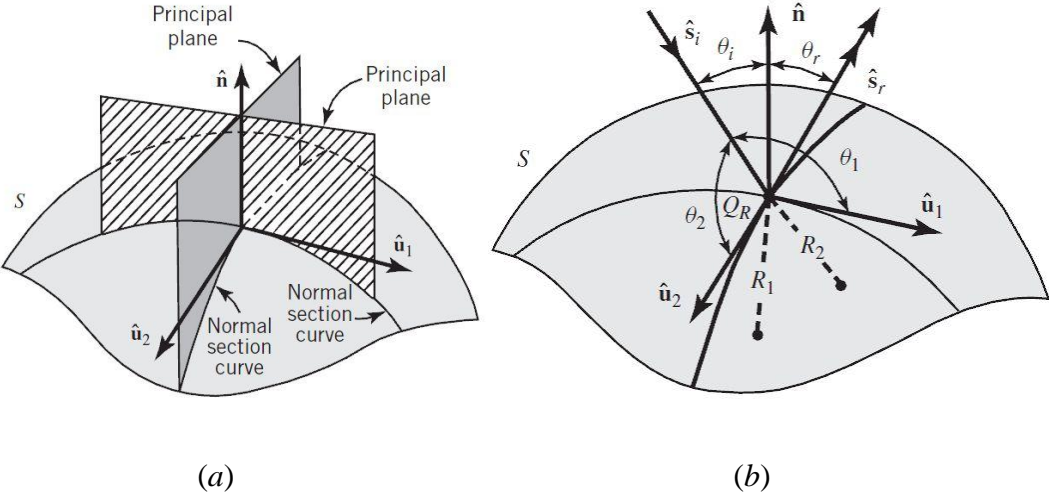


Figure 2-9 Parameters that can be defined for a reflecting surface (a) Normal section curves and principal planes (b) Principle radii of curvature (from [1])

In Figure 2-9a, \hat{n} is the unit normal vector to the surface at an arbitrary point, Q_R . There are infinitely many planes that include the unit normal vector. Each of these planes intersects the surface. The intersection is a curve, called as *normal section*

curve. Each normal section curve has its own radius of curvature. However, two of them are special among infinitely many normal section curves. For a well behaved surface, at an arbitrary point, one of them has a maximum radius of curvature and the other one has the minimum radius of curvature. Two planes that include these two special normal section curves are called *principal planes* and they are perpendicular to each other [1], as shown in Figure 2-9a.

In Figure 2-9b, the minimum and maximum radii of curvatures are represented by R_1 and R_2 . $\hat{\mathbf{u}}_1$ and $\hat{\mathbf{u}}_2$ are tangential unit vectors to the reflecting surface at Q_R and they are in principle planes. Therefore, they are also perpendicular to each other.

If an incident field hits a smooth surface, the reflection mechanism is mainly determined by Snell's law, $\theta_i = \theta_r$. However, boundary conditions determined by Maxwell's equations should also be taken into account.

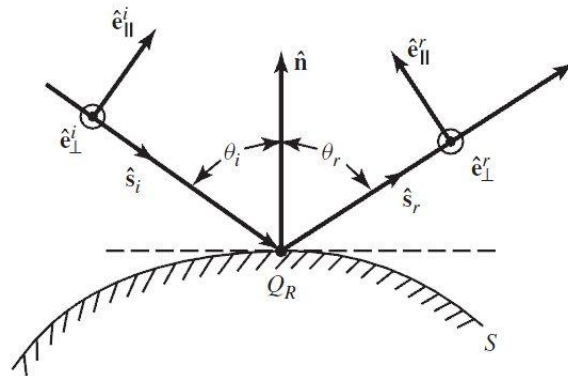


Figure 2-10 Reflection from a well-behaved surface (from [1])

In Figure 2-10; $\hat{\mathbf{s}}^i$, $\hat{\mathbf{s}}^r$ and $\hat{\mathbf{n}}$ are in the same plane. The incident and the reflected fields can be decomposed into the two components: parallel to this plane and perpendicular to this plane. $\hat{\mathbf{e}}_{\parallel}^i$ and $\hat{\mathbf{e}}_{\parallel}^r$ are the unit vectors of parallel components of the incident or reflected fields, respectively. Similarly, $\hat{\mathbf{e}}_{\perp}^i$ and $\hat{\mathbf{e}}_{\perp}^r$ are the unit vectors of perpendicular components of the incident or reflected fields, respectively.

The main idea behind the concept of the reflection mechanism is the fact that tangential components of the total, incident plus reflected, fields should be zero. Both parallel and perpendicular components given above have the tangential fields. For instance, for a perfect conducting surface; the incident field is assumed to be,

$$\vec{\mathbf{E}}_0^i = \hat{\mathbf{e}}_{\parallel}^i E_{0\parallel}^i + \hat{\mathbf{e}}_{\perp}^i E_{0\perp}^i \quad (2.40)$$

then the reflected field can be obtained in Eqn. (2.41).

$$\vec{\mathbf{E}}_0^r(s=0) = \vec{\mathbf{E}}_0^i(Q_R) \cdot \overline{\overline{\mathbf{R}}} = \vec{\mathbf{E}}_0^i(Q_R) \cdot [\hat{\mathbf{e}}_{\parallel}^i \hat{\mathbf{e}}_{\parallel}^r - \hat{\mathbf{e}}_{\perp}^i \hat{\mathbf{e}}_{\perp}^r] \quad (2.41)$$

where $\vec{\mathbf{E}}_0^r(s=0)$ = the reflected field just after the reflection point

$\vec{\mathbf{E}}_0^i(Q_R)$ = the incident field at the reflection point

$\overline{\overline{\mathbf{R}}}$ = dyadic reflection coefficient for PEC, $\begin{bmatrix} 1 & 0 \\ 0 & -1 \end{bmatrix}$

Eqn. (2.41) is rewritten, by using the incident field terms given in Eqn. (2.40), as

$$\vec{\mathbf{E}}_0^r(s=0) = \hat{\mathbf{e}}_{\parallel}^r E_{0\parallel}^i - \hat{\mathbf{e}}_{\perp}^r E_{0\perp}^i \quad (2.42)$$

It is clear that dyadic reflection coefficient given above makes the tangential components of the total field (*incident field given in Eqn. (2.40) plus reflected field given in Eqn. (2.42)*) zero. There are two assumptions here:

- The reflecting surface is planar very near the Q_R point
- The incident wave front is planar

These two assumptions require high-frequencies; however, it is shown that this approach is also valid for many practical problems.

If Eqn. (2.39) is applied to the Eqn. (2.41), the general formula of a reflected field at the distance s can be found as in the following Eqn. (2.43).

$$\vec{\mathbf{E}}^r(s) = \underbrace{\vec{\mathbf{E}}^i(Q_R)}_{\text{Field at reference point } Q_R} \cdot \underbrace{\bar{\mathbf{R}}}_{\text{Dyadic Reflection Coefficient}} \underbrace{\sqrt{\frac{\rho_1^r \rho_2^r}{(\rho_1^r + s)(\rho_2^r + s)}}}_{\text{Spatial attenuation (divergence) factor}} \underbrace{e^{-j\beta s}}_{\text{Phase factor}} \quad (2.43)$$

where ρ_1^r and ρ_2^r are principal radii of curvature of the reflected wave front at Q_R and they are defined in Figure 2-11.

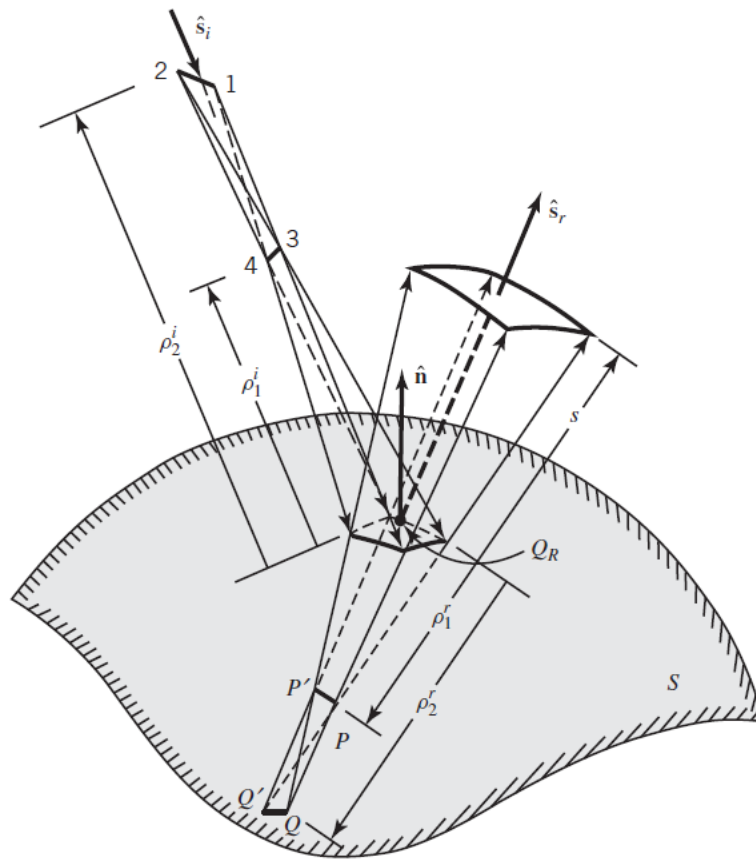


Figure 2-11 Astigmatic tube of rays and principal radii of curvature of reflected and incident waves at a curved surface (from [1])

According to the [7], the principal radii of curvature of the reflected field wave front, ρ_1^r and ρ_2^r , can be written in terms of the principal radii of curvature of the incident field wave front, ρ_1^i and ρ_2^i , and focal distances. The relationship defined at [7] is given in Eqn. (2.44) and Eqn. (2.45).

$$\boxed{\frac{1}{\rho_1^r} = \frac{1}{2} \left\{ \frac{1}{\rho_1^i} + \frac{1}{\rho_2^i} \right\} + \frac{1}{f_1}} \quad (2.44)$$

$$\boxed{\frac{1}{\rho_2^r} = \frac{1}{2} \left\{ \frac{1}{\rho_1^i} + \frac{1}{\rho_2^i} \right\} + \frac{1}{f_2}} \quad (2.45)$$

The focal distances, f_1 and f_2 , formula includes a high-order matrix terms that can be calculated from incident and reflecting angles and also includes principal radii of the reflecting surface. Detailed formulas can be found in [7] and they are not covered in this thesis; however, it should be underlined that if the incident wave front is planar, then $\rho_1^i = \rho_2^i = \infty$, and using Eqn. (2.44) and Eqn. (2.45), Eqn. (2.46) can be obtained.

$$\frac{1}{\rho_1^r \rho_2^r} = \frac{1}{f_1 f_2} = \frac{4}{R_1 R_2} \Rightarrow \rho_1^r \rho_2^r = \frac{R_1 R_2}{4} \quad (2.46)$$

According to the Eqn. (2.46), for a planar incident wave front, the principal radii of curvature of the reflected wave approach to infinity if R_1 and/or R_2 is infinite. Therefore, if the incident wave front is planar, GO cannot determine the radii of curvature of reflected wavefront when the reflecting surface is planar or cylindrical since these surfaces have infinite radii of curvature. This is a weakness about GO.

Another fundamental model in propagation problems is finding the total reflected field of a cylindrically reflected wavefront. Cylindrically shaped problems are important because 3-D problems can be represented in 2-D by the help of this type

of structures. It is mentioned before for a cylindrically reflected wavefront $\rho_1^r = \infty$ and $\rho_2^r = \rho^r$. Therefore, Eqn. (2.43) can be rewritten as in Eqn. (2.47); however, ρ^r is still unknown.

$$\boxed{\vec{\mathbf{E}}^r(s) = \vec{\mathbf{E}}^i(Q_R) \cdot \vec{\mathbf{R}} \sqrt{\frac{\rho^r}{\rho^r + s}} e^{-j\beta s}} \quad (2.47)$$

Cylindrical field may be radiated from an infinitely long line source located at a distance ρ_0 from the reflecting surface. 2-D representation of this case is given in Figure 2-12.

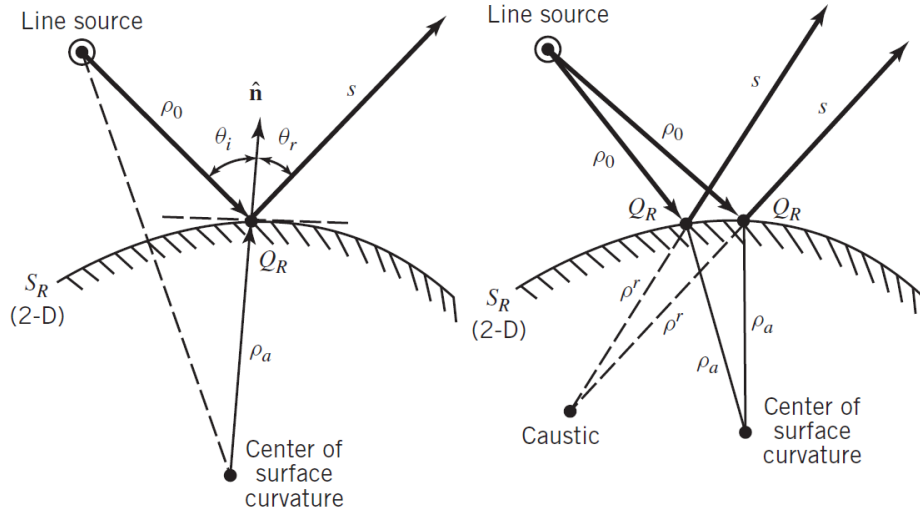


Figure 2-12 Reflection of a cylindrical field radiated from an infinite line (from [1])

If the reflection is like in Figure 2-12, according to [14], ρ^r can be obtained by

$$\frac{1}{\rho^r} = \frac{1}{\rho_0} + \frac{1}{\rho_a \cos \theta_i} \quad (2.48)$$

where ρ_0 is the distance of line source and ρ_a is the curvature of reflecting surface.

A fundamental example guides the more complex problems given in the following Figure 2-13.

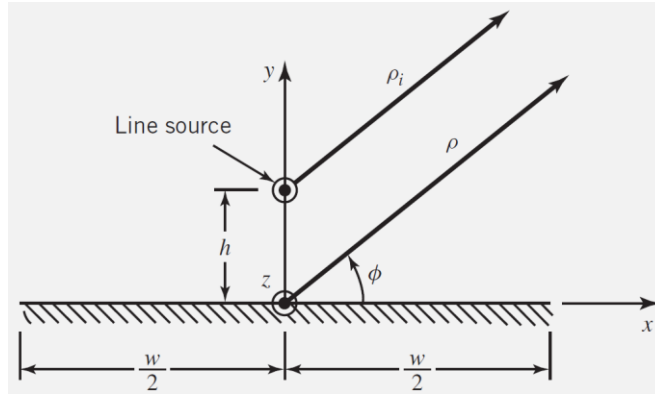


Figure 2-13 An infinitely long z-directed, constant I_0 current electric line source above a finite width, infinite length PEC strip (from [1])

According to [1], when there is no strip an infinitely long z-directed electric line radiates the field given in Eqn. (2.49) at a distance ρ_i ,

$$E_z^i = -\frac{\beta^2 I_0}{4\omega\epsilon} H_0^{(2)}(\beta\rho_i) \quad (2.49)$$

where $H_0^{(2)}(\beta\rho_i)$ is the Hankel function of zero order and of the second kind and ρ_i is shown in Figure 2-13. In Eqn. (2.49), far-field approximation property of the Hankel function of the second kind of the zero order can be used. It is given in Eqn. (2.50) for $n=0$.

$$H_n^{(2)}(\beta\rho) \stackrel{\beta\rho \rightarrow \text{large}}{\cong} \sqrt{\frac{2j}{\pi\beta\rho}} j^n e^{-j\beta\rho} \quad (2.50)$$

where

$$\beta\rho = 2\pi \frac{\rho}{\lambda} \quad (2.51)$$

According to Eqn. (2.51), large $\beta\rho$ values can be obtained by large ρ values and/or small λ values. Therefore, although the property given in Eqn. (2.50) is generally called as far-field or far-zone observation, it can be satisfied “near” field observations if the frequency is sufficiently high.

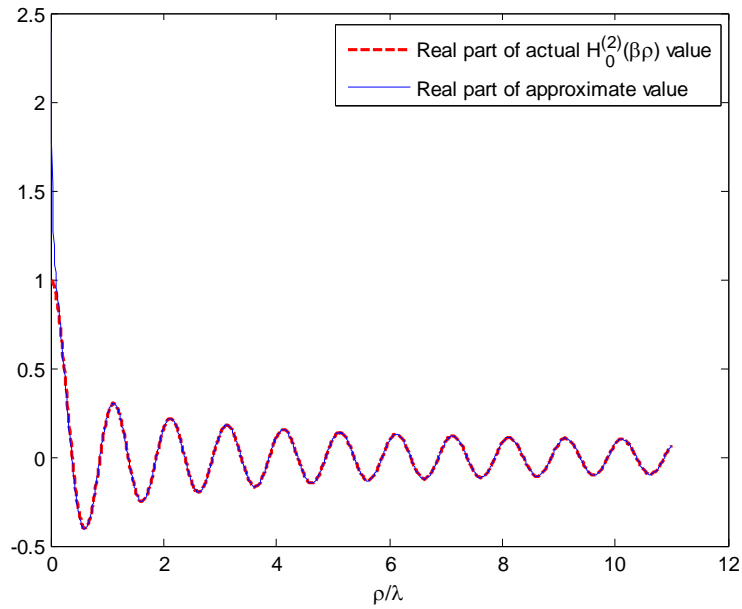


Figure 2-14 Far-zone approximation of $H_0^{(2)}(\beta\rho)$ (*real part*)

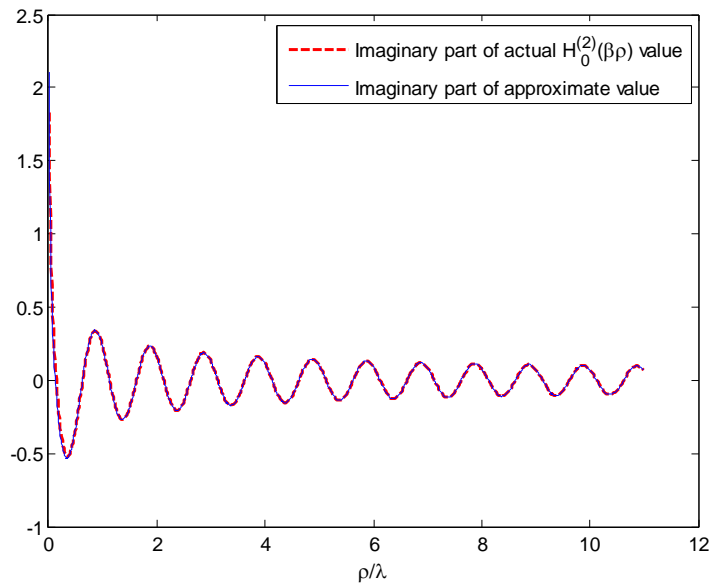


Figure 2-15 Far-zone approximation of $H_0^{(2)}(\beta\rho)$ (*imaginary part*)

Comparison of far-zone approximated values and actual values of $H_0^{(2)}(\beta\rho)$ is given in terms of real and imaginary part in Figure 2-14 and Figure 2-15, respectively. It is clear that even for small ρ/λ values, approximated values of $H_0^{(2)}(\beta\rho)$ is quite close to actual values. If ρ/λ is bigger than 10, the approximation is definitely consistent. Therefore, Eqn. (2.49) can be rewritten as

$$E_z^i = E_0 \frac{e^{-j\beta\rho_i}}{\sqrt{\rho_i}} \quad (2.52)$$

where
$$E_0 = -\frac{\beta^2 I_0}{4\omega\varepsilon} \sqrt{\frac{2j}{\pi\beta}} = -\eta I_0 \sqrt{\frac{j\beta}{8\pi}} \quad \text{where } \eta = \sqrt{\frac{\mu}{\varepsilon}} \quad (2.53)$$

Using Eqn. (2.47), Eqn. (2.48) with $\rho_a = \infty$ and Eqn. (2.52); the reflected field can be written as in Eqn. (2.54). ρ_r is shown in Figure 2-16.

$$E_z^r = -E_0 \frac{e^{-j\beta\rho_r}}{\sqrt{\rho_r}} \quad (2.54)$$

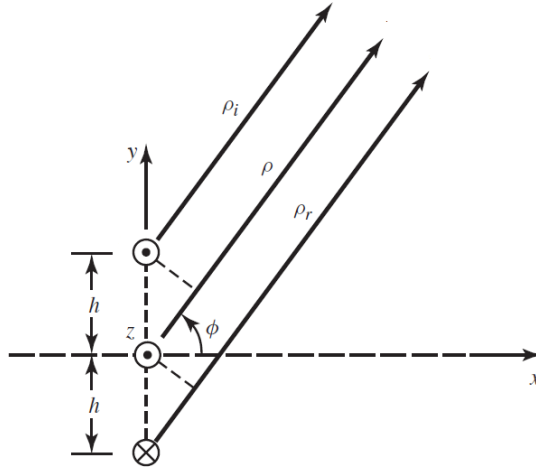


Figure 2-16 Infinitely long z-directed electric line with incident and reflected paths at far-field

It is obvious that the reflected field given in Eqn. (2.54) is in the same form as that radiates from a hypothetical image of the actual electric line source. In the far-zone applications ρ_i and ρ_r can be written as

$$\left. \begin{aligned} \rho_i &= \rho - h \sin \phi \\ \rho_r &= \rho + h \sin \phi \end{aligned} \right\} \text{for phase terms} \quad (2.55)$$

$$\rho_i \approx \rho_r \approx \rho \quad \left. \vphantom{\begin{aligned} \rho_i &= \rho - h \sin \phi \\ \rho_r &= \rho + h \sin \phi \end{aligned}} \right\} \text{for amplitude terms}$$

Using Eqn. (2.55), the incident field given in Eqn. (2.52) and reflected field given in Eqn. (2.54) can be rewritten as

$$E_z^i = E_0 e^{+j\beta h \sin \phi} \frac{e^{-j\beta \rho}}{\sqrt{\rho}}, \quad 0 \leq \phi \leq \pi + \alpha, \quad 2\pi - \alpha \leq \phi \leq 2\pi$$

$$E_z^r = -E_0 e^{-j\beta h \sin \phi} \frac{e^{-j\beta \rho}}{\sqrt{\rho}}, \quad \alpha \leq \phi \leq \pi - \alpha \quad (2.56)$$

Both incident and reflected fields are defined only in some particular regions given in Eqn. (2.56). In the shadow regions, there are no incident and reflected fields. The α angle in Eqn. (2.56) is shown in Figure 2-17 and it depends on h and w .

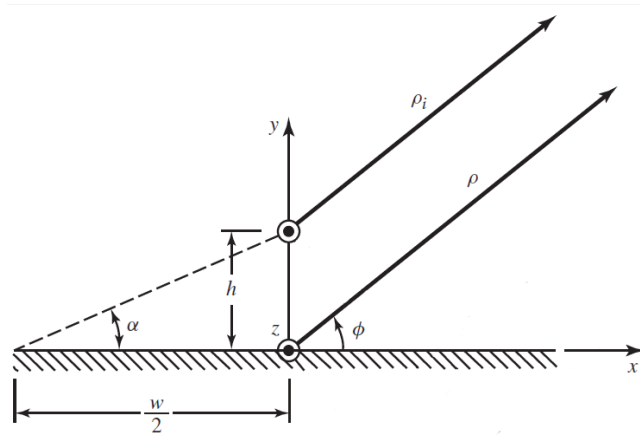


Figure 2-17 The α angle depends on h/w

Therefore, the total field can be written as

$$E_z^{total} = \begin{cases} E_0 e^{+j\beta h \sin \phi} \frac{e^{-j\beta \rho}}{\sqrt{\rho}} & 0 \leq \phi \leq \alpha, \\ & \pi - \alpha \leq \phi \leq \pi + \alpha, \\ & 2\pi - \alpha \leq \phi \leq 2\pi \\ 2jE_0 \sin(\beta h \sin \phi) \frac{e^{-j\beta \rho}}{\sqrt{\rho}} & \alpha \leq \phi \leq \pi - \alpha \\ 0 & \pi + \alpha \leq \phi \leq 2\pi - \alpha \end{cases} \quad (2.57)$$

For $h = 0.5\lambda$, the normalized total E field pattern is plotted in Figure 2-18 for both the $w = 2\lambda$ and $w = \infty$ cases.

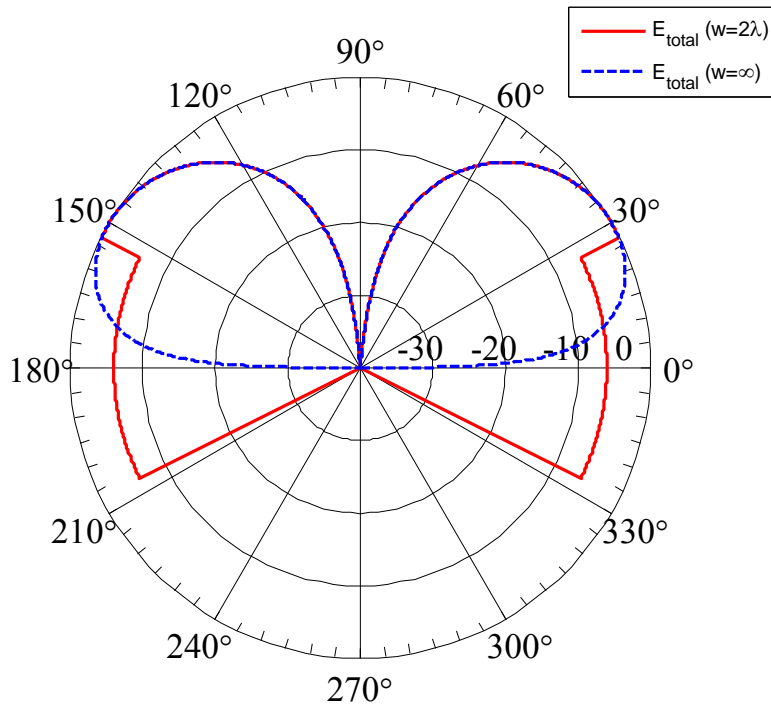


Figure 2-18 The total field distribution of an infinitely long electric line source given in Figure 2-13, calculated by the code developed in MATLAB[®]

According to Figure 2-17, for $w = 2\lambda$ case, $\alpha = \tan^{-1}(0.5\lambda / \lambda) \Rightarrow \alpha = 26.5^\circ$. The angle α indicates the incident and reflection shadow boundaries. In Figure 2-18, there are discontinuities at field distribution at shadow boundaries where $\phi = 180^\circ \pm 26.5^\circ$ and $\phi = 360^\circ \pm 26.5^\circ$. Even if the higher-order Luneberg-Kline expansion terms in Eqn. (2.35) are taken into account when calculating the GO terms, these discontinuities cannot be overcome.

In general, the failures of GO method can be summarized as:

- Singularities at the field calculations at or very closed to the caustics.
- Field discontinuities at or very closed to the shadow boundaries.
- Obvious field calculation errors due to the edges or surface discontinuities.
- Not describing any diffracted fields in the shadow region.

Although the GO method gives accurate results rarely, like $w = \infty$ case in Figure 2-18, it is necessary to improve GO for most of the cases. Improvements result in more accurate results for discontinuities, singularities or calculation errors. However, even if a deeper analysis is done in the limits of GO method, the diffracted fields in shadow region can never be obtained. Therefore, another approach that introduces the diffraction mechanism into the classical geometrical optics method is necessary. This approach is called as *Geometrical Theory of Diffraction* (GTD).

2.3 GEOMETRICAL THEORY OF DIFFRACTION

In real life applications, the total field distribution of a very long electric line source, located over a $w = 2\lambda$ strip, cannot be like in Figure 2-18, since there are discontinuities at shadow boundaries and there is no field at diffraction region. Therefore, classical GO is extended to Geometrical Theory of Diffraction (GTD) in order to contain diffraction fields additional to geometrical optics fields.

2.3.1 Amplitude, Phase and Polarization Relations in GTD

By using a similar approach as GO, Eqn. (2.58) can be developed for GTD, [1].

$$\vec{\mathbf{E}}^d(s) = \vec{\mathbf{E}}^d(0') \sqrt{\frac{\rho'_c \rho_c}{(\rho'_c + s)(\rho_c + s)}} e^{-j\beta s} \quad (2.58)$$

where $\vec{\mathbf{E}}^d(0') =$ diffracted field at the reference point, $0'$

$s =$ observation distance from the reference point, $0'$

$\rho'_c =$ distance from the diffraction point Q_D to the reference point $0'$

$\rho_c =$ distance from the second caustic to the reference point $0'$

The parameters given in Eqn. (2.58) are shown in Figure 2-19. Figure 2-19 shows the general case for edge diffraction; because, the field is obliquely incident upon a curved edge. The normal incidence is a special case of oblique incidence ($\beta'_0 = 90^\circ$) and straight edge is the infinite curvature case of curved edge. Also it should be noted that the field in Eqn. (2.58) is defined from the reference point $0'$ not the diffraction point Q_D . The point Q_D is also the first caustic of diffracted field.

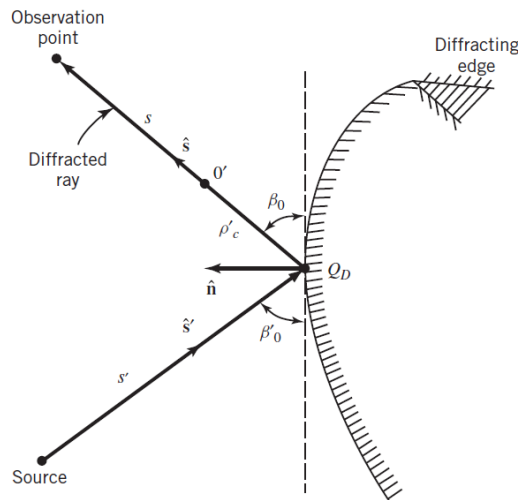


Figure 2-19 Oblique incidence diffraction from a curved edge (from [1])

After some mathematical manipulation and by carrying the reference point from $0'$ to Q_D ,

$$\vec{\mathbf{E}}^d(s) = \underbrace{\vec{\mathbf{E}}^i(Q_D)}_{\text{Field at reference point } Q_D} \cdot \underbrace{\vec{\mathbf{D}}}_{\text{Dyadic Diffraction Coefficient}} \underbrace{\sqrt{\frac{\rho_c}{s(\rho_c + s)}}}_{\text{Spatial attenuation (divergence) factor } A(\rho_c, s)} \underbrace{e^{-j\beta s}}_{\text{Phase factor}} \quad (2.59)$$

where $\vec{\mathbf{E}}^i(Q_D)$ = the incident field at the diffraction point,

ρ_c = distance between the first caustic Q_D (also the reference point, $s = 0$)

and the second caustic of the diffracted fields

The fields obtained from Eqn. (2.59) give the fields at the diffraction region and eliminates the discontinuities at the shadow boundaries at the same time.

Eqn. (2.59) is the most general formula for diffraction since it covers both the curved and straight edges. Since the curved edge diffraction is beyond the scope of this thesis, a simpler form of Eqn. (2.59) can be used for the straight edge case given in Figure 2-20.

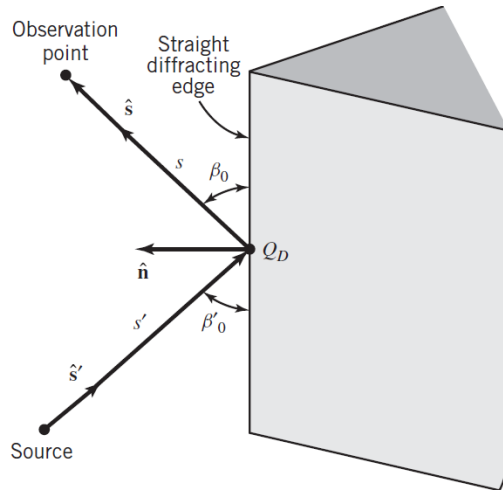


Figure 2-20 Oblique incidence wedge diffraction from a straight edge (from [1])

The simpler form of Eqn. (2.59) can be written as in the Eqn. (2.60) [1],

$$\boxed{\bar{\mathbf{E}}^d(s) = \bar{\mathbf{E}}^i(Q_D) \cdot \bar{\mathbf{D}} A(s', s) e^{-j\beta s}} \quad (2.60)$$

where

$$A(s', s) = \begin{cases} \frac{1}{\sqrt{s}} & \text{for plane and conical wave incidence} \\ \frac{1}{\sqrt{\rho}}, \rho = s \sin \beta_0 & \text{for cylindrical wave incidence} \\ \sqrt{\frac{s'}{s(s'+s)}} \stackrel{s \gg s'}{\cong} \frac{\sqrt{s'}}{s} & \text{for spherical wave incidence} \end{cases} \quad (2.61)$$

Actually Eqn. (2.61) can be derived from the $A(\rho_c, s)$ part of the Eqn. (2.59) by using $\rho_c = \infty$ for plane, conical and cylindrical waves and $\rho_c = s'$ for spherical waves.

This thesis is mainly focused on the straight edge diffraction when the field is normally incident upon a wedge.

2.3.2 Straight Edge Diffraction of the Normally Incident Waves upon a Wedge

The normal incidence means β'_0 , defined in Figure 2-20, is equal to 90° . One of simplest case for normal incidence can be defined as in Figure 2-21 or Figure 2-22. The line source is infinitely long and also wedge is infinitely long. This 2-D problem can be solved by the approximation of the normally incident wave upon a straight edge.

Infinitely long line source generates cylindrical waves as mentioned before. Although it does not seem a general case, by the help of the reciprocity theorem, this approach plays an important role in calculating the unique unknown parameter, D , in Eqn. (2.60).

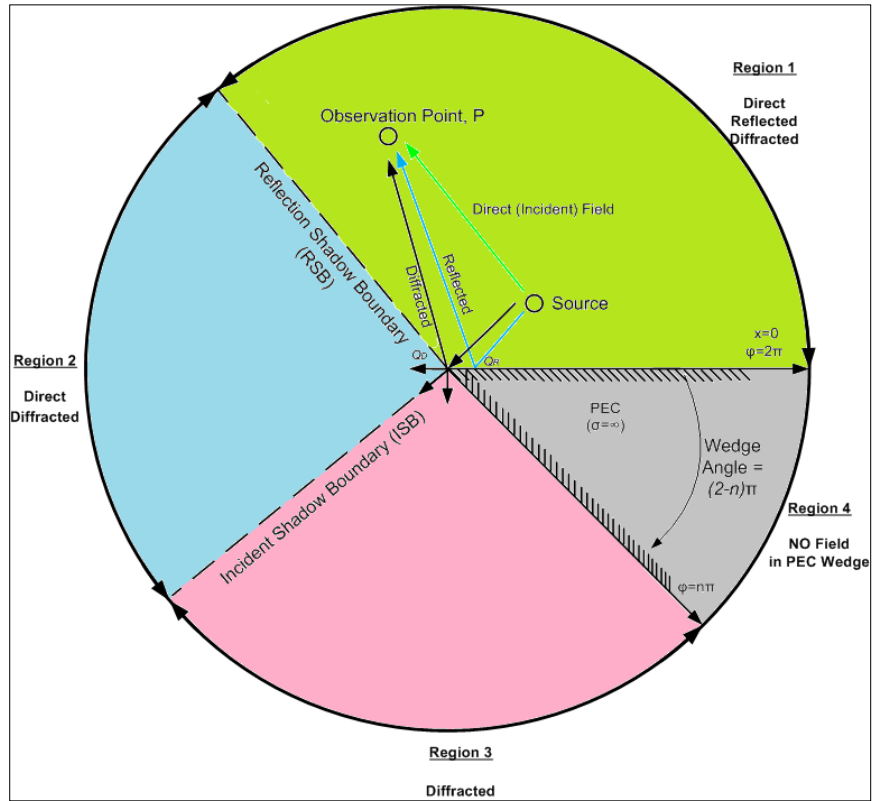


Figure 2-21 Regions of a wedge diffraction

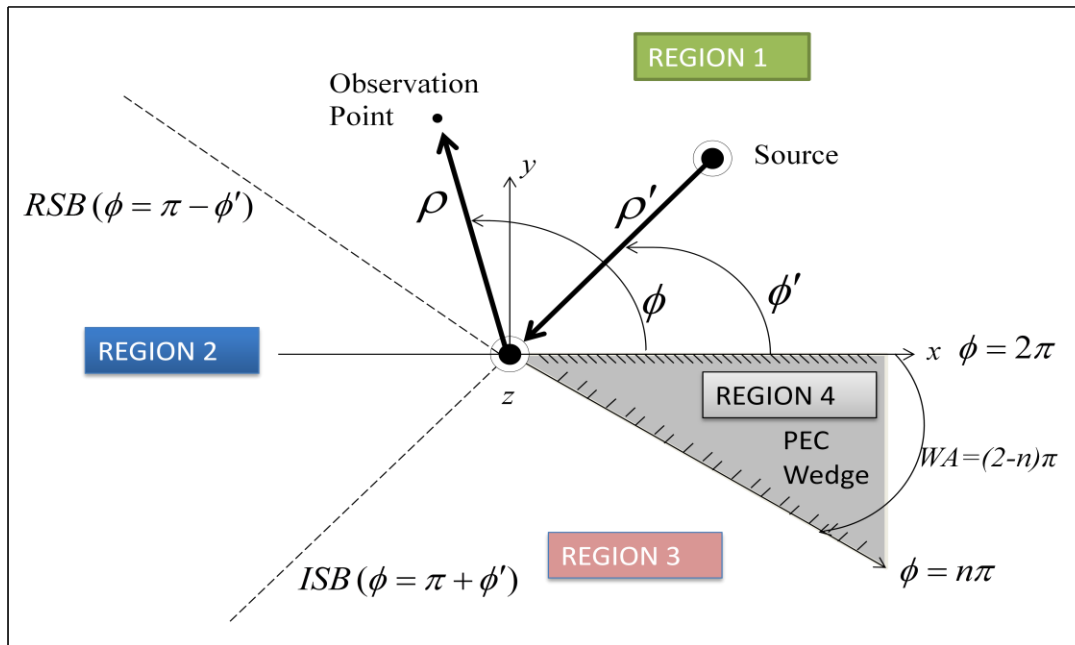


Figure 2-22 Regions of a wedge diffraction in coordinate system

In Figure 2-21, two important boundaries are shown. These are *Reflection Shadow Boundary* (RSB) and *Incident Shadow Boundary* (ISB). These boundaries emphasize that the incident and reflected fields cannot be existed after ISB and RSB, respectively. These boundaries and wedge divide the coordinate system into the four regions. While all the fields, *direct, reflected and diffracted fields*, exist in Region I; there is no reflected field in Region II since it is on the other side of the RSB. And in Region III, there are only diffracted fields. Region IV is the PEC wedge; therefore, there is no field there. The existing fields are given in Table 2-1.

Table 2-1 Existence of fields in Figure 2-22

Existence of Fields			
	<i>Diffracted</i>	<i>Direct</i>	<i>Reflected</i>
Region I	+	+	+
Region II	+	+	-
Region III	+	-	-
Region IV	-	-	-

2.3.3 The Total Field Scattered by a PEC Wedge

To find the total field scattered by a PEC wedge, when the source is an infinitely long line; first, the radiated field of an infinitely long line in the absence of the wedge should be found.

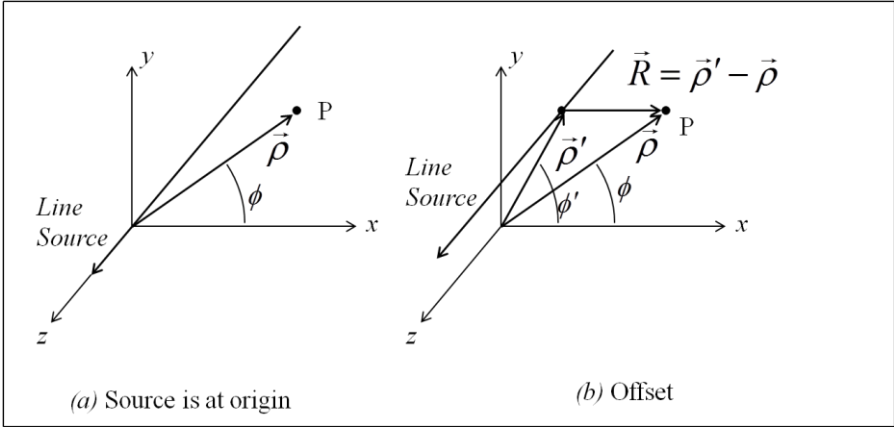


Figure 2-23 Infinitely long line source shown in coordinate system

The E-field radiated from the infinitely long electric line shown in Figure 2-23a is given in Eqn. (2.49) previously. Recall the Eqn. (2.49):

$$\boxed{E_z = -\frac{\beta^2 I_e}{4\omega\epsilon} H_0^{(2)}(\beta\rho)} \quad (2.62)$$

When the line source is at the origin, at far field, TEM^{*ρ*} is satisfied; therefore, E_{*z*} or H_{*φ*} can be obtained from the other one. Similar formula is valid for the offset electric line case given in Figure 2-23b:

$$\boxed{E_z = -\frac{\beta^2 I_e}{4\omega\epsilon} H_0^{(2)}(\beta|\vec{\rho} - \vec{\rho}'|)} \quad (2.63)$$

However, this time TEM^{*ρ*} is not satisfied since H_{*ρ*} is not zero anymore due to the circumferential angle is different than *φ*. Eqn. (2.63) is also gives the H_{*z*} for the magnetic line source by using the duality principle:

$$\boxed{H_z = -\frac{\beta^2 I_m}{4\omega\mu} H_0^{(2)}(\beta|\vec{\rho} - \vec{\rho}'|)} \quad (2.64)$$

Eqn. (2.63) and Eqn. (2.64) are the field distribution in the absence of conducting wedge. Some principles should be used to calculate the total field in the existence of wedge [1]:

- Total field (incident plus scattered fields) must vanish at the boundaries of the PEC wedge
- Reciprocity principle should be satisfied in the total field equation (*ρ* ↔ *ρ'*)
- *φ* variations must be represented by standing wave functions

Also by using the Fourier series for a current impulse [15], it is possible to represent the total field in the form of an infinite series of Bessel and sinusoidal functions. After some mathematical manipulations, the total field of both electric and magnetic line sources can be represented by only one formula [1]. For the infinitely long line source and wedge given in Figure 2-24, the total field is given in Eqn. (2.65).

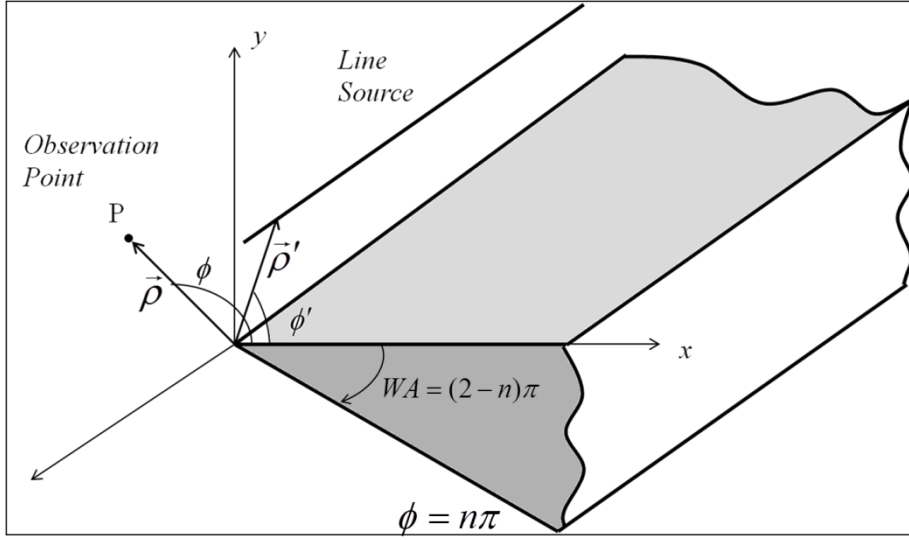


Figure 2-24 Infinitely long line source and PEC wedge

$$\begin{aligned}
 E_z^{total} &= -\frac{\omega\mu I_e}{4} G(\rho, \rho', \phi, \phi', n) \text{ for TM}^z \text{ (electric line source)} \\
 H_z^{total} &= +\frac{\omega\varepsilon I_m}{4} G(\rho, \rho', \phi, \phi', n) \text{ for TE}^z \text{ (magnetic line source)}
 \end{aligned}
 \tag{2.65}$$

where $G(\rho, \rho', \phi, \phi', n)$ is equal to

$$G = \frac{1}{n} \begin{cases} \sum_{m=0}^{\infty} \varepsilon_m J_{m/n}(\beta\rho) H_{m/n}^{(2)}(\beta\rho') \left\{ \cos \left[\frac{m}{n}(\phi - \phi') \right] \pm \cos \left[\frac{m}{n}(\phi + \phi') \right] \right\} & \text{for } \rho \leq \rho' \\ \sum_{m=0}^{\infty} \varepsilon_m J_{m/n}(\beta\rho') H_{m/n}^{(2)}(\beta\rho) \left\{ \cos \left[\frac{m}{n}(\phi - \phi') \right] \pm \cos \left[\frac{m}{n}(\phi + \phi') \right] \right\} & \text{for } \rho' \leq \rho \end{cases}
 \tag{2.66}$$

where $\varepsilon_m = \begin{cases} 1 & \text{for } m = 0 \\ 2 & \text{for } m \neq 0 \end{cases}$

In Eqn. (2.66), for electric line, TM^z , minus (-) sign is used; for magnetic line, TE^z , plus (+) sign is used between cosine terms. Electric line case is also called as *soft polarization* while magnetic line case is called *hard polarization*. The function G is called as *Green's Function*.

Eqn. (2.65) and Eqn. (2.66) give the exact total field scattered by a PEC wedge. Although equations are exact, they are not useful to calculate the unknown diffraction coefficient, D ; since, Eqn. (2.66) is poorly convergent for the large arguments of the Hankel or Bessel functions. The improvement is mainly discussed for the first part of the Eqn. (2.66) in this thesis. In other words, plane wave incidence is primary concern of this thesis. While $\rho \leq \rho'$ corresponds to the plane wave incidence, $\rho' \leq \rho$ corresponds to the cylindrically wave incidence and far-zone observation. Although plane wave incidence will be discussed in a detail way in this thesis, cylindrically wave incidence case can be easily found by using the reciprocity principle ($\rho \leftrightarrow \rho'$) and ($\phi \leftrightarrow \phi'$).

In [16], Hutchins suggests first obtaining an integral form of modal solution of plane wave incidence given in Eqn. (2.66); then, dividing this integral into the GO (incident and reflected) and GTD (incident and reflected) parts.

If the source is very far away from the diffraction point, the incident field upon the wedge is assumed as plane wave. For the offset orientation shown is Figure 2-23b and plane wave incidence ($\rho \leq \rho'$) case and by using the asymptotic expansion of the Hankel function of the second kind of order m/n , Eqn. (2.67) can be written,

$$\begin{aligned}
 E_z^{total} &= -\frac{\omega\mu I_e}{4} G \\
 \text{where } G &= \sqrt{\frac{2j}{\pi\beta}} \frac{e^{-j\beta\rho'}}{\sqrt{\rho'}} F(\beta\rho) \\
 \text{where } F(\beta\rho) &= \frac{1}{n} \sum_{m=0}^{\infty} \varepsilon_m J_{m/n}(\beta\rho) e^{j\frac{m\pi}{n^2}} \left\{ \cos\left[\frac{m}{n}(\phi - \phi')\right] - \cos\left[\frac{m}{n}(\phi + \phi')\right] \right\}
 \end{aligned} \tag{2.67}$$

$F(\beta\rho)$ in Eqn. (2.67) can also be used to find total H_z for a magnetic line source by only replacing the minus sign (-) between cosine terms with the plus sign (+). It should be noted that wedge angle is taken into account in Eqn. (2.67) since n depends on the wedge angle ($WA = [2 - n]\pi$). However Eqn. (2.67) does not take into account the fact that there is no field inside the PEC wedge.

Since ρ' is very far away from the diffraction point, the incident wave is plane wave. Therefore $F(\beta\rho)$ in Eqn. (2.67) gives total (*diffracted + incident + reflected*) field at (ρ, ϕ) when a unity amplitude plane wave is incident upon a wedge with an angle of ϕ' . In other words, Eqn. (2.67) corresponds to the case in Figure 2-25a. In Figure 2-25b, source is not at infinity and incident wave is cylindrical wave; but this time, observation is made at a distance very far away from the diffraction point, almost infinity. For the case Figure 2-25b, the total field at observation point, P, can easily be found by applying the reciprocity principle to the $F(\beta\rho)$ in Eqn. (2.67). In other words, by replacing ρ with ρ' , ϕ with ϕ' and ϕ' with ϕ , $F(\beta\rho')$ can be found from Eqn. (2.67). ϕ exchanges do not make any sense since cosine is an even function.

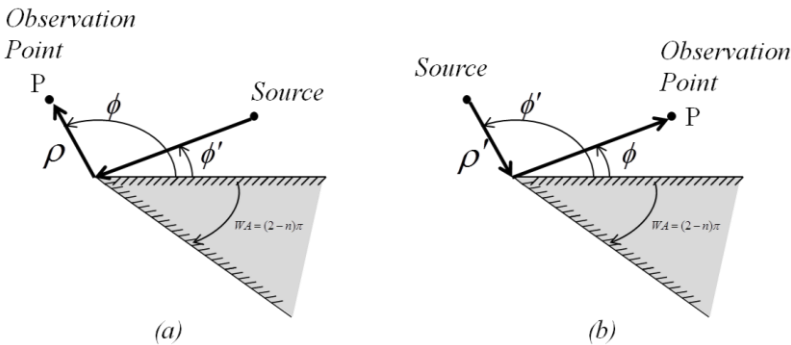


Figure 2-25 (a) Plane wave incidence (b) Cylindrical wave incidence

For the case of Figure 2-25a, the total E and H field is given in Figure 2-26 and in Figure 2-27 when the source is electric line (*soft-polarization*) and magnetic line (*hard-polarization*) for $\phi' = 30^\circ, \rho = \lambda$, respectively.

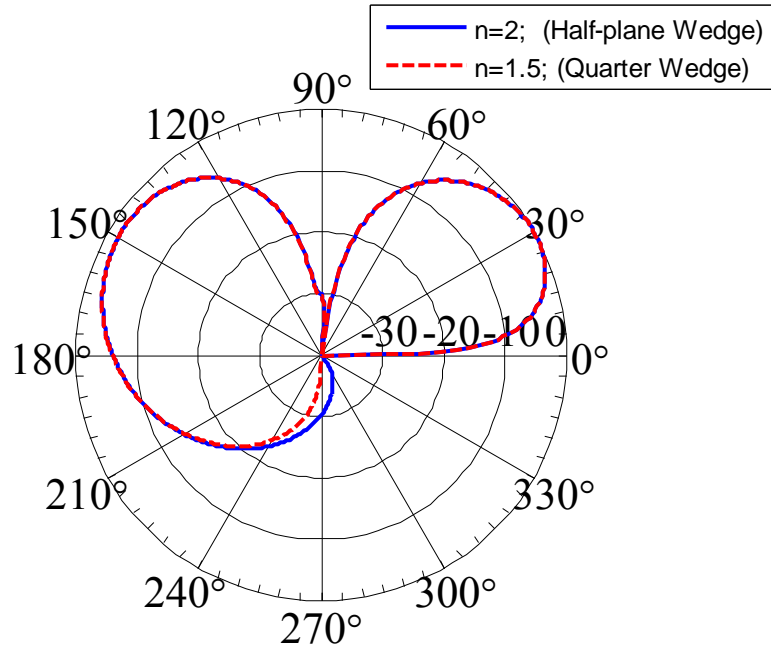


Figure 2-26 The ϕ -variation of the total E-field at $\rho = \lambda$ when the unity amplitude plane wave radiated from an electric line-source $\phi' = 30^\circ$ is incident upon a wedge

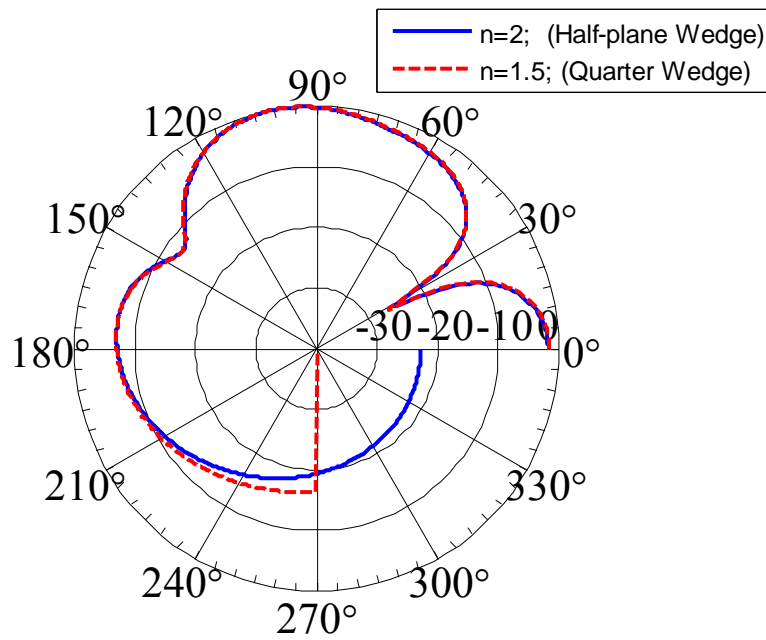


Figure 2-27 The ϕ -variation of the total H-field at $\rho = \lambda$ when the unity amplitude plane wave radiated from a magnetic line-source $\phi' = 30^\circ$ is incident upon a wedge

2.3.4 The Diffraction Coefficient in GTD

Previously, the exact modal solution given in Eqn. (2.65) and Eqn. (2.66) transformed into high-frequency asymptotic solution given in Eqn. (2.67). As mentioned before, when the incident wave is unity plane wave, the total field can be represented by $F(\beta\rho)$ given in Eqn. (2.67). By rewriting the $F(\beta\rho)$ part of the Eqn. (2.67),

$$F(\beta\rho) = \frac{1}{n} \sum_{m=0}^{\infty} \varepsilon_m J_{m/n}(\beta\rho) e^{j\frac{m\pi}{n^2}} \left\{ \cos\left[\frac{m}{n}(\phi - \phi')\right] \mp \cos\left[\frac{m}{n}(\phi + \phi')\right] \right\} \quad (2.68)$$

Infinite series given in Eqn. (2.68) is poorly convergent for large arguments ($\beta\rho$) of Bessel function. Therefore, $F(\beta\rho)$ has to be written in the form of inverse powers of $\beta\rho$ to overcome the convergence problem [1]. To obtain this form, *conventional method of steepest descent* is used. However in order to apply this method to Eqn. (2.68), Eqn. (2.68) which is in the form of an infinite series of modal solution should be converted into the integral form [16]. The Watson transformation (details can be found in [4], [17] and [18]) can be used for this modification.

After some mathematical manipulation Eqn. (2.68) can be written as,

$$F(\beta\rho) = \underbrace{\frac{1}{4\pi jn} \int_{(c'-c)} \cot\left(\frac{\phi - \phi' + z}{2n}\right) e^{j\beta\rho \cos z} dz}_{F_1(\beta\rho)} \pm \underbrace{\frac{1}{4\pi jn} \int_{(c'-c)} \cot\left(\frac{\phi - \phi' + z}{2n}\right) e^{j\beta\rho \cos z} dz}_{F_2(\beta\rho)} \quad (2.69)$$

$F_1(\beta\rho)$ and $F_2(\beta\rho)$ correspond to the incident and reflected fields, respectively.

By using the *method of steepest descent* (details are given in [5] and [19]), $F_1(\beta\rho)$ can be written as in the Eqn. (2.70) and similar procedure is valid for $F_2(\beta\rho)$.

Since $C' - C = C_T - \text{SDP}_{+\pi} - \text{SDP}_{-\pi}$;

$$F_1(\beta\rho) = \frac{1}{4\pi j n} \oint_{C_T} \cot\left(\frac{\phi - \phi' + z}{2n}\right) e^{j\beta\rho \cos z} dz - \frac{1}{4\pi j n} \int_{\text{SDP}_{+\pi}} \cot\left(\frac{\phi - \phi' + z}{2n}\right) e^{j\beta\rho \cos z} dz - \frac{1}{4\pi j n} \int_{\text{SDP}_{-\pi}} \cot\left(\frac{\phi - \phi' + z}{2n}\right) e^{j\beta\rho \cos z} dz \quad (2.70)$$

Then by using the residue calculus from [20],

$$\boxed{F_1(\beta\rho)|_{C_T} = e^{j\beta\rho \cos(\phi - \phi')} U[\pi - |-(\phi - \phi')|]} \quad (2.71)$$

If the observation is far away from the incident shadow boundary for $F_1(\beta\rho)$, conventional steepest descent method can be used for the remaining part of $F_1(\beta\rho)$, $F_1(\beta\rho)|_{\text{SDP}_{\pm\pi}}$.

$$\boxed{F_1(\beta\rho)|_{\text{SDP}_{\pm\pi}} = -\frac{e^{-j\pi/4}}{2n\sqrt{2\pi\beta}} \frac{e^{-j\beta\rho}}{\sqrt{\rho}} \left\{ \cot\left[\frac{\pi + (\phi - \phi')}{2n}\right] + \cot\left[\frac{\pi - (\phi - \phi')}{2n}\right] \right\}} \quad (2.72)$$

Approximately, Eqn. (2.72) can be written as in the Eqn. (2.73)

$$\boxed{F_1(\beta\rho)|_{\text{SDP}_{\pm\pi}} \simeq \frac{e^{-j\pi/4}}{\sqrt{2\pi\beta}} \frac{\frac{1}{n} \sin\left(\frac{\pi}{n}\right)}{\cos\left(\frac{\pi}{n}\right) - \cos\left(\frac{\phi - \phi'}{n}\right)} \frac{e^{-j\beta\rho}}{\sqrt{\rho}}} \quad (2.73)$$

It should be noted that when $\phi = \phi' + \pi$ (at ISB) Eqn. (2.73) has singularity.

Using the same notation $F_2(\beta\rho)|_{C_T}$ and $F_2(\beta\rho)|_{SDP_{\pm\pi}}$ can be written as,

$$\boxed{F_2(\beta\rho)|_{C_T} = e^{j\beta\rho\cos(\phi+\phi')} U[\pi - (\phi + \phi')]} \quad (2.74)$$

$$\boxed{F_2(\beta\rho)|_{SDP_{\pm\pi}} \simeq \frac{e^{-j\pi/4}}{\sqrt{2\pi\beta}} \frac{\frac{1}{n} \sin\left(\frac{\pi}{n}\right)}{\cos\left(\frac{\pi}{n}\right) - \cos\left(\frac{\phi+\phi'}{n}\right)} \frac{e^{-j\beta\rho}}{\sqrt{\rho}}} \quad (2.75)$$

Like the deficiency of $F_1(\beta\rho)|_{SDP_{\pm\pi}}$ at ISB, $F_2(\beta\rho)|_{SDP_{\pm\pi}}$ has deficiency at RSB ($\phi = \pi - \phi'$) since the denominator of Eqn. (2.75) is zero at RSB. Therefore *conventional method of steepest descent* is need to be modified. The modified method is called as *Pauli-Clemmov modified method of steepest descent* ([5] and [20]).

Pauli-Clemmov modified method of steepest descent adds a transition function multiplied with the each cotangent term in Eqn. (2.72). The transition function removes the deficiency of $F_1(\beta\rho)|_{SDP_{\pm\pi}}$ at ISB and the deficiency of $F_2(\beta\rho)|_{SDP_{\pm\pi}}$ at RSB. When going away from the shadow boundaries transition function is almost unity and *Pauli-Clemmov modified method of steepest descent* turns into the *conventional steepest descent method*.

The generalized form of the transition function is the Eqn. (2.76). And g^\pm is defined in Eqn. (2.77).

$$\boxed{F[\beta\rho g^\pm(\phi \pm \phi')] = 2j \sqrt{\beta\rho g} e^{+j\beta\rho g} \int_{\sqrt{\beta\rho g}}^{\infty} e^{-j\tau^2} d\tau} \quad (2.76)$$

where g^\pm is selected as g^+ for $SDP_{+\pi}$, g^- for $SDP_{-\pi}$

$g^+ = 1 + \cos\left[(\phi \pm \phi') - 2n\pi N^+\right]$ $g^- = 1 + \cos\left[(\phi \pm \phi') - 2n\pi N^-\right]$ <p>$\phi \pm \phi'$ is selected as $\phi - \phi'$ for incident field, $\phi + \phi'$ for reflected field where N^+, N^- is the closest integer that satisfies the following equation:</p> $2n\pi N^+ - (\phi \pm \phi') = +\pi \text{ for } g^+$ $2n\pi N^- - (\phi \pm \phi') = -\pi \text{ for } g^-$	(2.77)
---	--------

For the transition function in Eqn. (2.76), the following approximations can be used ([23], [24]). For the X values between 0.3 and 5.5, linear interpolation is used [1].

$$F(X) \simeq \left[\sqrt{\pi X} - 2Xe^{j\pi/4} - \frac{2}{3}X^2e^{-j\pi/4} \right] e^{j(\pi/4+X)} \text{ for } X < 0.3$$

$$F(X) \simeq \left[1 + j\frac{1}{2X} - \frac{3}{4}\frac{1}{X^2} - j\frac{15}{8}\frac{1}{X^3} + \frac{75}{16}\frac{1}{X^4} \right] \text{ for } X > 5.5 \quad (2.78)$$

Although, up to now, generally mathematical derivations of $F(\beta\rho)$ are covered in this part, there are physical meanings of the mathematical equations ([21], [22]).

To sum up, first, $F(\beta\rho)$ is divided into the two parts and each part is divided into the two integrals.

$$F(\beta\rho) = F_1(\beta\rho) + F_2(\beta\rho)$$

$$F_{1,2}(\beta\rho) = F_{1,2}(\beta\rho)\Big|_{C_T} + F_{1,2}(\beta\rho)\Big|_{SDP_{\pm\pi}}$$

They correspond to physically the following fields.

$$F_1(\beta\rho)\Big|_{C_T} = \text{Incident Geometrical Optics Fields}$$

$$F_2(\beta\rho)\Big|_{C_T} = \text{Reflected Geometrical Optics Fields}$$

$$F_1(\beta\rho)\Big|_{SDP_{\pm\pi}} = \text{Incident Diffracted Fields}$$

$$F_2(\beta\rho)\Big|_{SDP_{\pm\pi}} = \text{Reflected Diffracted Fields}$$

Since $F(\beta\rho)$ represents the total field when the unity amplitude plane wave incident upon a 2-D wedge, diffraction part of the $F(\beta\rho)$ is related to diffraction coefficient. In order to obtain diffraction coefficient, $F(\beta\rho)$ should be divided into GO and diffracted parts:

$$F(\beta\rho) = F_{GO}(\beta\rho) + F_{Diff}(\beta\rho) \quad (2.79)$$

Then the relation between incidence diffraction fields and incidence diffraction coefficient can be defined as in the Eqn. (2.80).

$$F_{Diff}^i(\beta\rho) = V^i(\rho, \phi, \phi', n) = \frac{e^{-j\beta\rho}}{\sqrt{\rho}} D^i \quad (2.80)$$

Similarly the relation between reflected diffraction fields and reflection diffraction coefficient can be defined as in the Eqn. (2.81).

$$F_{Diff}^r(\beta\rho) = V^r(\rho, \phi, \phi', n) = \frac{e^{-j\beta\rho}}{\sqrt{\rho}} D^r \quad (2.81)$$

Therefore soft and hard polarized functions can be written as in the Eqn. (2.82).

$$\boxed{\begin{aligned} V_{Soft}(\rho, \phi, \phi', n) &= \frac{e^{-j\beta\rho}}{\sqrt{\rho}} D^i - \frac{e^{-j\beta\rho}}{\sqrt{\rho}} D^r = \frac{e^{-j\beta\rho}}{\sqrt{\rho}} D^{soft}; D^{soft} = D^i - D^r \\ V_{Hard}(\rho, \phi, \phi', n) &= \frac{e^{-j\beta\rho}}{\sqrt{\rho}} D^i + \frac{e^{-j\beta\rho}}{\sqrt{\rho}} D^r = \frac{e^{-j\beta\rho}}{\sqrt{\rho}} D^{hard}; D^{hard} = D^i + D^r \end{aligned}} \quad (2.82)$$

Soft diffraction coefficient, D^{soft} and hard diffraction coefficient, D^{hard} are given in Eqn. (2.83) and Eqn. (2.84), respectively. These coefficients are called as *Keller's diffraction coefficients*. It should be noted that *Keller's diffraction coefficients* have singularities at reflection and incident shadow boundaries.

Keller's diffraction coefficients:

$$\begin{aligned}
 D^{soft} &= D^i - D^r \\
 &\simeq \frac{e^{-j\pi/4} \frac{1}{n} \sin\left(\frac{\pi}{n}\right)}{\sqrt{2\pi\beta}} \left[\frac{1}{\cos\left(\frac{\pi}{n}\right) - \cos\left(\frac{\phi - \phi'}{n}\right)} - \frac{1}{\cos\left(\frac{\pi}{n}\right) - \cos\left(\frac{\phi + \phi'}{n}\right)} \right]
 \end{aligned} \tag{2.83}$$

$$\begin{aligned}
 D^{hard} &= D^i + D^r \\
 &\simeq \frac{e^{-j\pi/4} \frac{1}{n} \sin\left(\frac{\pi}{n}\right)}{\sqrt{2\pi\beta}} \left[\frac{1}{\cos\left(\frac{\pi}{n}\right) - \cos\left(\frac{\phi - \phi'}{n}\right)} + \frac{1}{\cos\left(\frac{\pi}{n}\right) - \cos\left(\frac{\phi + \phi'}{n}\right)} \right]
 \end{aligned} \tag{2.84}$$

Uniform theory of diffraction (UTD) coefficients:

$$\begin{aligned}
 D^{soft} &= D^i - D^r \\
 &= -\frac{e^{-j\pi/4}}{2n\sqrt{2\pi\beta}} \times \\
 &\quad \left\{ \cot\left[\frac{\pi + (\phi - \phi')}{2n}\right] F[\beta\rho g^+(\phi - \phi')] + \cot\left[\frac{\pi - (\phi - \phi')}{2n}\right] F[\beta\rho g^-(\phi - \phi')] \right\} \\
 &\quad - \left\{ \cot\left[\frac{\pi + (\phi + \phi')}{2n}\right] F[\beta\rho g^+(\phi + \phi')] + \cot\left[\frac{\pi - (\phi + \phi')}{2n}\right] F[\beta\rho g^-(\phi + \phi')] \right\}
 \end{aligned} \tag{2.85}$$

$$\begin{aligned}
 D^{hard} &= D^i + D^r \\
 &= -\frac{e^{-j\pi/4}}{2n\sqrt{2\pi\beta}} \times \\
 &\quad \left\{ \cot\left[\frac{\pi + (\phi - \phi')}{2n}\right] F[\beta\rho g^+(\phi - \phi')] + \cot\left[\frac{\pi - (\phi - \phi')}{2n}\right] F[\beta\rho g^-(\phi - \phi')] \right\} \\
 &\quad + \left\{ \cot\left[\frac{\pi + (\phi + \phi')}{2n}\right] F[\beta\rho g^+(\phi + \phi')] + \cot\left[\frac{\pi - (\phi + \phi')}{2n}\right] F[\beta\rho g^-(\phi + \phi')] \right\}
 \end{aligned} \tag{2.86}$$

UTD coefficients in Eqn. (2.85) and Eqn. (2.86) reduces to the Keller's diffraction coefficients, when transition functions are removed (i.e., they are assumed unity).

UTD coefficients include all the terms in Keller's formula; besides, they also have Fresnel transition functions. By the help of these transition functions, singularities near the incident shadow boundary (ISB) and reflected shadow boundary (RSB) could be eliminated.

For instance, assume the source angle $\phi' = 30^\circ$ in Figure 2-25a when the incident wave is unity plane wave upon a half-plane conducting wedge ($n = 2$). In this case, ISB occurs at 210° and RSB occurs at 150° . The incident diffracted field magnitude calculated by the code developed in MATLAB[®] is given in Figure 2-28. It can be seen Keller's diffraction approach has singularity at ISB, 210° . Especially, when the observation is made at near-field ($\rho = \lambda$) errors may occur even though ϕ is far away from ISB.

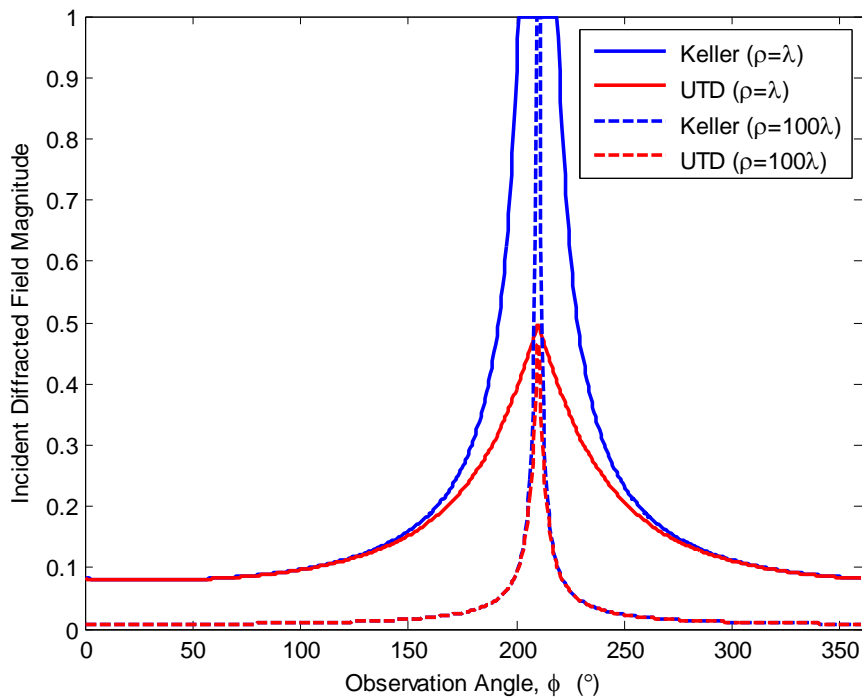


Figure 2-28 Incident diffracted field of plane wave upon a half-plane wedge

Similarly, the reflected diffracted field magnitude is given in Figure 2-29. For this case, Keller's diffraction approach has singularity at RSB, 150° .

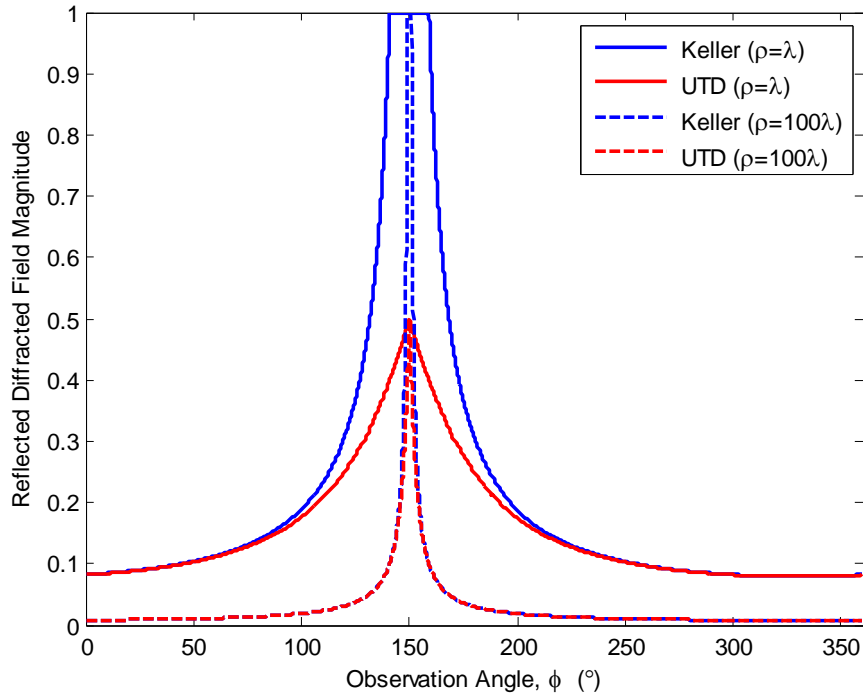


Figure 2-29 Reflected diffracted field of plane wave upon a half-plane wedge

2.4 ADVANTAGES OF GTD COMPARED TO GO

As mentioned before, Geometrical Theory of Diffraction (GTD) fields can be divided into the two parts: Geometrical Optics (GO) fields and Diffracted fields. Therefore, GTD includes GO. Besides, by the aid of the additional diffraction mechanisms, GTD is able to overcome the discontinuities around shadow boundaries and to predict the field distribution in diffraction region.

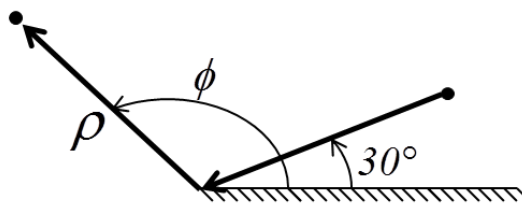


Figure 2-30 Plane wave incidence with an angle of 30° upon a half-plane wedge

Previously, for a half-plane wedge given in Figure 2-30, the exact normalized E-field distribution is given in Figure 2-26. This pattern is calculated by using the modal solutions.

By the help of the soft polarized GO fields given in Eqn. (2.87)

$$F_1(\beta\rho)|_{C_T} - F_2(\beta\rho)|_{C_T} \quad (2.87)$$

The code developed in MATLAB[®] gives GO fields as in Figure 2-31. It should be noted that this result is consistent with image theory. However, there is no field in diffraction region and there are discontinuities at boundaries.

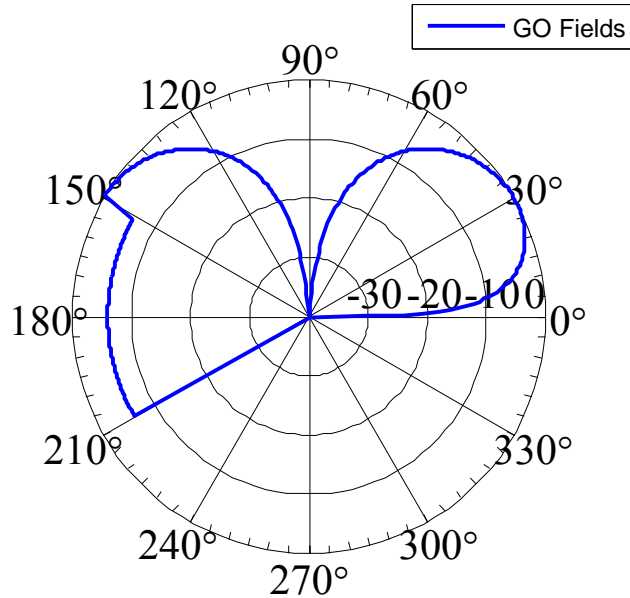


Figure 2-31 Normalized GO fields pattern for Figure 2-30

The GDT contribution says that there are also incident diffracted fields $(F_1(\beta\rho)|_{SDP_{\pm\pi}})$ and reflected diffracted fields $(F_2(\beta\rho)|_{SDP_{\pm\pi}})$. If these fields are taken into account in the developed, the fields can be calculated as in Figure 2-32.

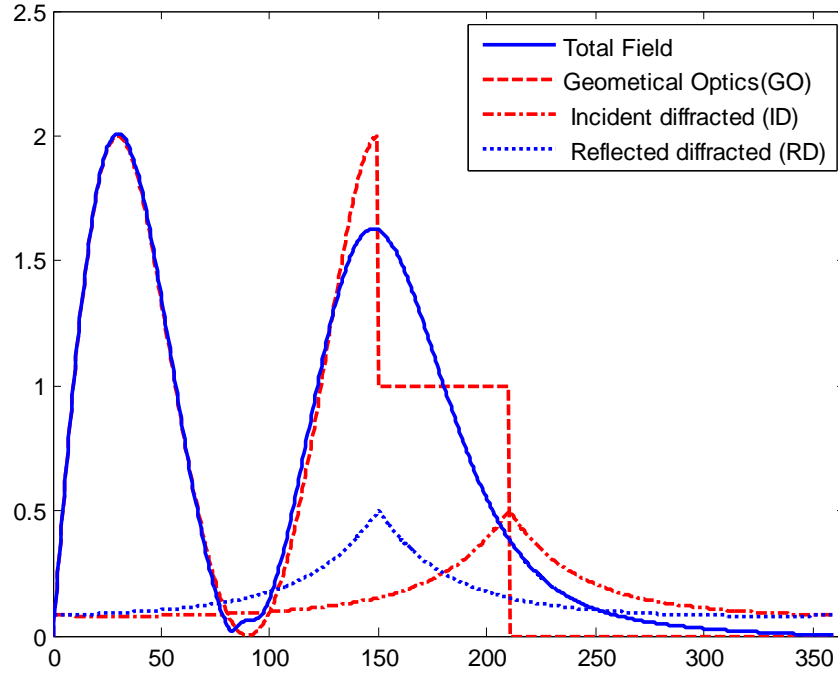


Figure 2-32 GO, diffracted and total (GTD) fields for Figure 2-30

Normalized polar plot of total field whose linear plot is given in Figure 2-32 is given in Figure 2-26. Figure 2-32 demonstrates the contribution of GTD, clearly.

- Although there is no GO fields after 210° , ID and RD exist there.
- ID is dominant at ISB and RD is dominant at RSB.
- Discontinuities of GO at ISB and RSB is removed by adding ID and RD.

Another example that can be used for GTD and GO comparison is given in Figure 2-33. The geometry was discussed in GO part of this theses and its GO field distribution is given in Figure 2-18, previously for $h = 0.5\lambda$ and $w = 2\lambda$. ISB and RSB are determined by α defined in Figure 2-34. Since $\alpha = 26.5^\circ$, discontinuities in Figure 2-18 exist at $0 \pm 26.5^\circ$ and $180 \pm 26.5^\circ$.

$$\alpha = \tan^{-1}\left(\frac{h}{w/2}\right) = \tan^{-1}(0.5) = 26.5^\circ$$

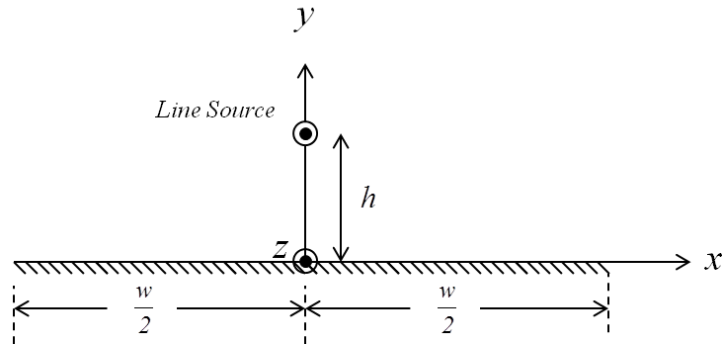


Figure 2-33 An infinitely long line source above w -width finite strip

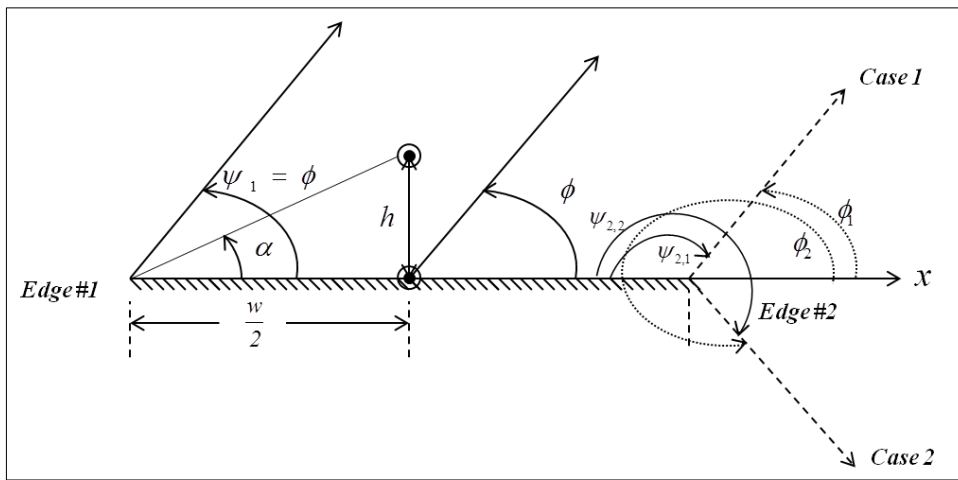


Figure 2-34 Angle definitions on the strip

When calculating diffracted fields it is important to define angles correctly. For Edge #1 the observation angle and GTD angle defined from the surface of wedge are same: $\phi = \psi_1$. However for Edge #2, these two angles are complementary. By using the geometry given in Figure 2-34 it can be written:

$$\psi_{2,1} = 180 - \phi_1, \text{ for Case 1}$$

$$\psi_{2,2} = 540 - \phi_2, \text{ for Case 2}$$

Also far-field approximations for amplitude and phase terms should be used.

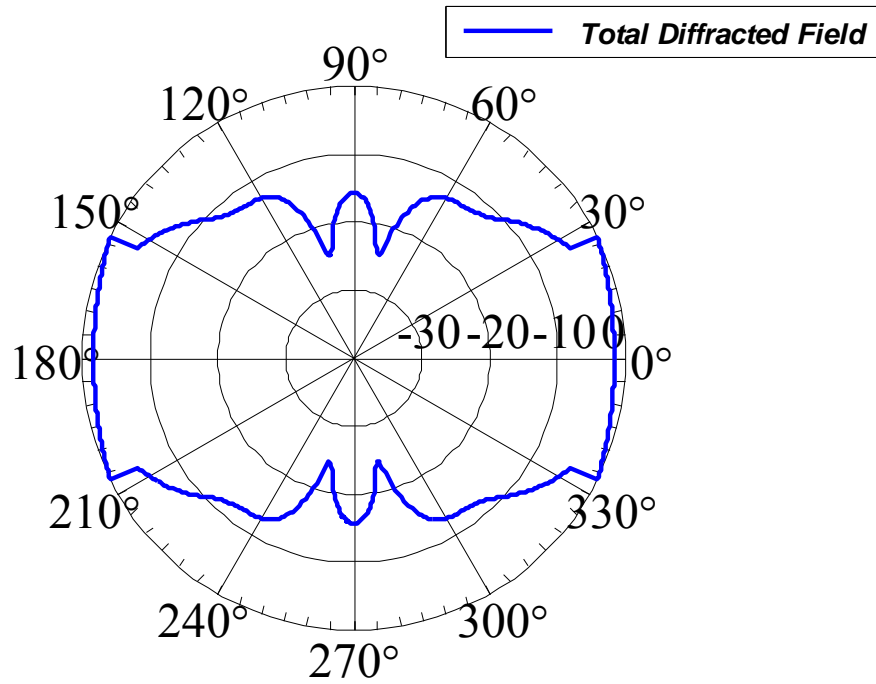


Figure 2-35 Normalized total diffracted field of an infinitely long line source above w -width finite strip given in Figure 2-33 ($h=0.5\lambda$ and $w=2\lambda$)

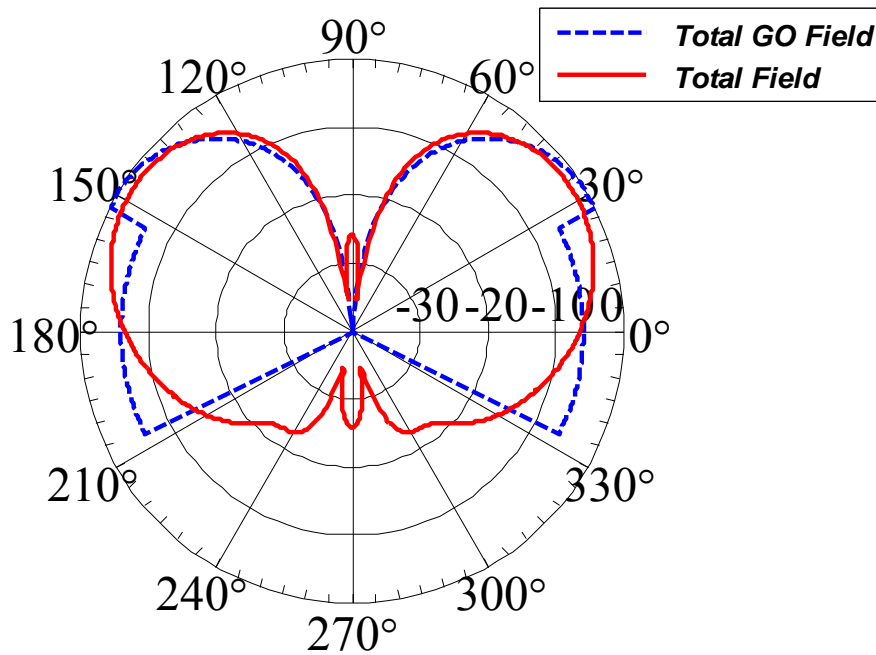


Figure 2-36 Total GO field and total (Diffracted + GO) field of for the geometry presented in Figure 2-33

By using the incident diffracted field $\left(F_1(\beta\rho)\Big|_{\text{SDP}_{\pm\pi}}\right)$ and reflected diffracted field $\left(F_2(\beta\rho)\Big|_{\text{SDP}_{\pm\pi}}\right)$ concepts, total diffracted field can be calculated by the code developed in MATLAB[®]. Normalized total diffracted field is given in Figure 2-35. It should be noted that total diffracted field has discontinuities where the GO field has also discontinuities. Therefore, diffracted field is able to compensate the discontinuities at GO fields. The total GTD (GO + diffracted) field is given Figure 2-36. By the diffraction mechanism of GTD, the discontinuities of GO field that exist at $0\pm 26.5^\circ$ and $180\pm 26.5^\circ$ are compensated. Also the field distribution in the diffraction region $(206.5^\circ(180+26.5) < \phi < 333.5^\circ(360-26.5))$ could be calculated.

To sum up, Geometrical Theory of Diffraction (GTD) fields are composed of Geometrical Optics (GO) fields and Diffracted fields. Therefore, GTD extends the GO approach.

By the aid of the additional diffraction mechanisms [1], GTD

- calculates the field distribution in the diffraction region,
- removes the discontinuities of GO near the ISB and RSB,
- handles the edge and surface discontinuities,
- provides fields even at caustics.

A good illustration of this comparison can be seen in Figure 2-36.

When calculating the diffracted fields of GTD, Fresnel transition functions in UTD may make the calculation steps more complex. Therefore, if the observation angle is far away from the incident shadow boundary (ISB) and reflected shadow boundary (RSB), Keller's diffraction approach can be used instead of UTD in calculations, for the sake of simplicity.

CHAPTER 3

EVALUATION OF GTD BASED PROPAGATION MODELS

In this chapter, after reviewing formulations of GTD, some real life propagation problems will be discussed by using GTD. In order to do that, simplified representations of terrain profiles are used. Although GTD is a high-frequency method, it provides quite acceptable results in real life propagation problems even for VHF due to the fact that the mountains, hills and ridges are electrically very large according to the operating wavelength [25]. For a typical public safety VHF communication system, operating frequency is 150 MHz and corresponding wavelength is 2 meters. It is very very small according to the elevation of mountains, generally hundreds or thousands of meters.

Then the propagation path loss values obtained by using GTD are compared with the results of another popular propagation path loss estimation tool: *the Longley-Rice method*. It is based on the electromagnetic theory and empirical data ([26], [27]). The model has common usage for most practical engineering problem due to its accurate estimations about the propagation path loss. There are lots of input parameters such as terrain profile, frequency, antenna heights, distance, the electrical properties of the ground (conductivity, permittivity), surface refractivity, etc. The details of Longley-Rice method is given in this chapter; however, for a more closer look at its theoretical background and for investigating the measurements that are the basis of Longley-Rice method; [26], the report proposed by Longley and Rice, can be analyzed.

Finally, the comparison between the propagation path losses (calculated by GTD and Longley-Rice method) and measured data is examined in order to find out the weaknesses and strengths about the approaches.

3.1 TERRAIN PROFILES ANALYZED BY USING GTD

In this part various types of terrain profiles are defined and analyzed by using GTD. Preferred terrain profiles are the capable of representing real life propagation paths between transmitter and receiver. The propagation path used for GTD is described by transforming the actual path into the 2-Dimensions (2-D). In other words, 2-D path is simply a plane defined on the Earth that includes both the transmitter and receiver antennas.

In brief, Geometrical theory of Diffraction (GTD), whose details are given in the previous chapter, enables to calculate the total field distribution for all propagation regions. The total field offered by GTD can be divided into four parts and their contribution to the total field is given in Eqn. (3.1). (-) is used for soft (*electric line*) polarization and (+) is used for hard (*magnetic line*) polarization in Eqn. (3.1).

$$\boxed{\begin{aligned} \text{Total Field} &= (\text{Incident GO Fields} \pm \text{Reflected GO Fields}) \\ &+ (\text{Incident Diffracted Fields} \pm \text{Reflected Diffracted Fields}) \end{aligned}} \quad (3.1)$$

Incident and reflected geometrical optics fields are defined in the regions where the direct path and specular reflection path is available between transmitted and receiver. They can be formulated for a half-plane wedge as in Eqn. (3.2).

$$\begin{aligned} \text{Incident GO Fields} &= e^{j\beta\rho\cos(\phi-\phi')}U\left[\pi - |-(\phi-\phi')|\right] \\ \text{Reflected GO Fields} &= e^{j\beta\rho\cos(\phi+\phi')}U\left[\pi - (\phi+\phi')\right] \end{aligned} \quad (3.2)$$

Unit step function in Eqn. (3.2) determines where the fields are defined with nonzero values. The field equations above are offered by Hutchins in [16]; however, they can also be calculated by the classical GO defined in the previous chapter.

Eqn. (3.3) gives the diffraction part of GTD and the diffracted field is defined everywhere except in the PEC wedge.

$$\vec{\mathbf{E}}^d(s) = \vec{\mathbf{E}}^i(Q_D) \cdot \bar{\bar{\mathbf{D}}} A(s', s) e^{-j\beta s} \quad (3.3)$$

where $\vec{\mathbf{E}}^i(Q_D)$ defines the incident field to the diffraction point, Q_D

$\bar{\bar{\mathbf{D}}}$ is the diffraction coefficient calculated by the code developed in MATLAB[®]

Diffraction coefficient in Eqn. (3.3) is calculated by the code developed in MATLAB[®], which is based on the uniform theory of diffraction, for both soft (*electric line*) and hard (*magnetic line*) polarization in this thesis. However, $\bar{\bar{\mathbf{D}}}$ can be calculated by using the Keller's diffraction approach, if the observation angle is far away the ISB or RSB.

Also $A(s', s)$, spatial attenuation factor, in Eqn. (3.3) is given by [1] as

$$A(s', s) = \begin{cases} \frac{1}{\sqrt{s}} & \text{for plane and conical wave incidence} \\ \frac{1}{\sqrt{\rho}}, \rho = s \sin \beta_0 & \text{for cylindrical wave incidence} \\ \sqrt{\frac{s'}{s(s'+s)}} \stackrel{s \gg s'}{\cong} \frac{\sqrt{s'}}{s} & \text{for spherical wave incidence} \end{cases} \quad (3.4)$$

3.1.1 A Mountain Modeled as a PEC Half-plane

PEC half-plane is also a wedge with a wedge angle of 0° . Therefore, the equations obtained for wedge diffraction is also valid for this example. Although there is no mountain in the natural that can be modeled as a half-plane as shown in Figure 3-1, it is preferred because it is a good starting point to represent more complex structures in the same way. Also some of the sharp mountains can be modeled as half-planes with some tolerable error. The transmitter antenna and the receiver antenna are located at either side of the mountain. Diffraction occurs at the top of the mountain. Antennas in Figure 3-1 are assumed as isotropic antennas and they are ideally matched. Gains and losses due to the antennas or cables can easily be added to the results.

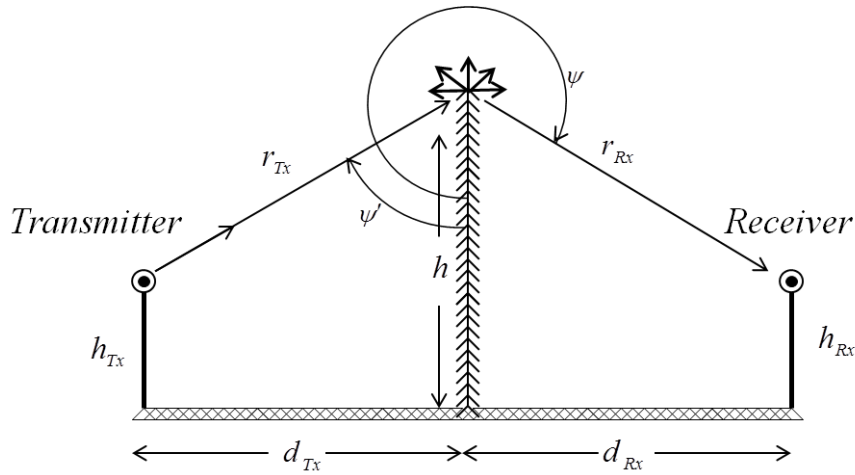


Figure 3-1 Transmitter and receiver antennas on either side of a mountain modeled as PEC Half-Plane Wedge

First, the “*path loss over free space loss*” is calculated. The “*path loss over free space loss*” states the additional loss due to presence of the obstacle between transmitter and receiver with respect to the line-of-sight case. In other words, free space loss always exists between transmitter and receiver due to the distance and it is not calculated in this section of this thesis in order to focus on obstruction loss. It also can be easily added to results like antenna gains/losses.

The path loss over free space loss is calculated by using $d_{Tx}, d_{Rx}, h_{Tx}, h_{Rx}$ and h as input parameters. It should be noted that frequency is not an input parameter, because GTD assumes frequency is always sufficiently “high”. Therefore, providing the same path loss for all the frequencies is one of the deficiencies of GTD since propagation path loss more or less depends on the frequency in real life.

In order to guarantee the validity of the developed MATLAB[®] code based on UTD, the obstruction loss is calculated by both Keller’s diffraction formula and the code developed in MATLAB[®], then the results are compared.

To calculate obstruction loss with Keller’s diffraction approach Eqn. (3.3) is used.

Eqn. (3.3) and parameters are given in Eqn. (3.5)

$$\begin{aligned}
 \vec{\mathbf{E}}^d(s) &= \vec{\mathbf{E}}^i(Q_D) \cdot \vec{\mathbf{D}} A(s', s) e^{-j\beta s} \\
 \vec{\mathbf{E}}^i(Q_D) &= \frac{e^{-j\beta r_{Tx}}}{r_{Tx}}, e^{-j\beta s} = e^{-j\beta r_{Rx}} \\
 A(s', s) &= \sqrt{\frac{s'}{s(s'+s)}} = \sqrt{\frac{r_{Tx}}{r_{Rx}(r_{Tx} + r_{Rx})}}
 \end{aligned} \tag{3.5}$$

Diffraction coefficients for soft and hard polarization can be found by using Eqn. (2.83) and Eqn. (2.84) with $n=2$. In the absence of obstacle, received field would be,

$$\begin{aligned}
 \vec{\mathbf{E}}^{\text{received at line-of-sight}} &= \frac{e^{-j\beta d}}{d} \text{ (Free Space Loss)} \\
 d &= \sqrt{(d_{Tx} + d_{Rx})^2 + (|h_{Tx} - h_{Rx}|)^2}
 \end{aligned} \tag{3.6}$$

By combining all these equations, obstruction loss is found as in Eqn. (3.7).

$$\begin{aligned}
 \text{Obstruction Loss} &= \left| \frac{\vec{\mathbf{E}}^{\text{diffracted}}}{\vec{\mathbf{E}}^{\text{received at line-of-sight}}} \right| \\
 &= \frac{d}{2\sqrt{2\pi\beta r_{Tx} r_{Rx} (r_{Tx} + r_{Rx})}} \left[\frac{1}{\cos\left(\frac{\phi - \phi'}{2}\right)} - \frac{1}{\cos\left(\frac{\phi + \phi'}{2}\right)} \right]
 \end{aligned} \tag{3.7}$$

For the $d_{Tx} = d_{Rx} = h = 5\lambda$ and $h_{Tx} = 0$ case, obstruction loss is calculated by both Keller's diffraction formula and the code developed in MATLAB[®]. Loss versus h_{Rx} , receiver antenna height, is plotted in Figure 3-2 and in Figure 3-3, for *soft* and *hard* polarization, respectively.

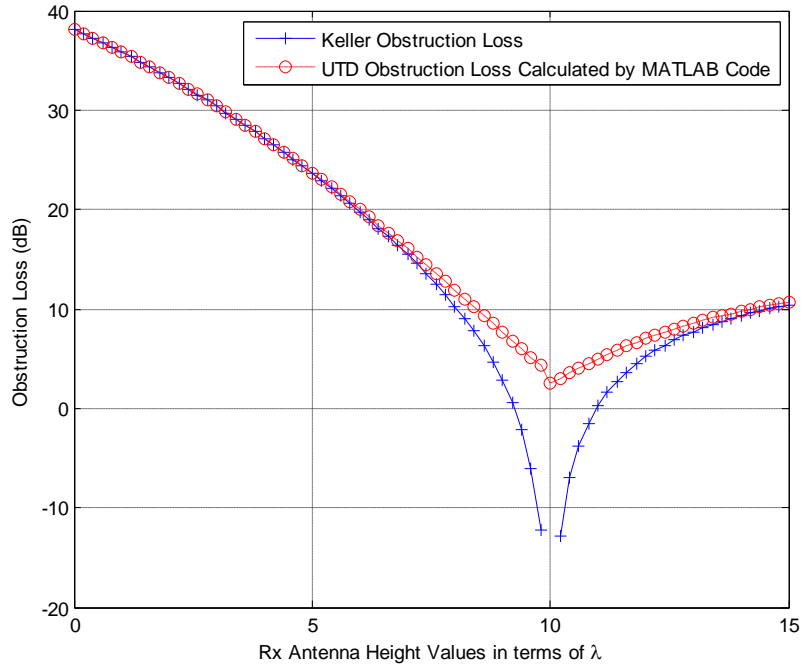


Figure 3-2 Comparison between obstruction loss values by using Keller's method and the UTD code developed in MATLAB[®] (*soft polarization*)

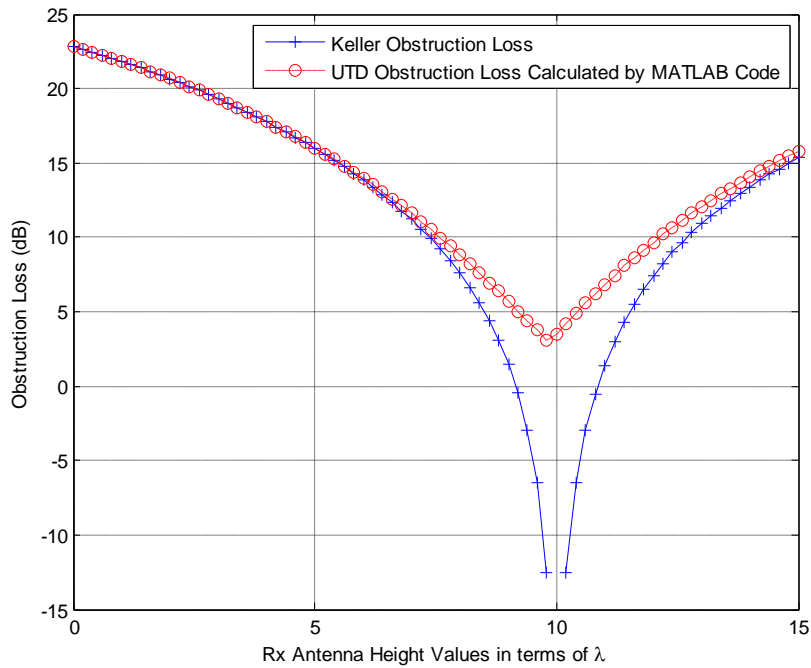


Figure 3-3 Comparison between obstruction loss values by using Keller's method and the UTD code developed in MATLAB[®] (*hard polarization*)

For the $d_{Tx} = d_{Rx} = h = 5\lambda$ and $h_{Tx} = 0$ case given in Figure 3-4, by using the basic trigonometry, it can be seen that incident shadow boundary (*ISB*) coincides with the receiver antenna when $h_{Rx} = 10\lambda$ since Keller's method fails around ISB, it has singularity at $h_{Rx} = 10\lambda$, as expected. Besides having the singularity, Keller's method has negative loss around ISB. It can be considered that negative loss corresponds to gain; therefore, Keller's method results do not make sense. However, the code developed in MATLAB[®] compensates the singularities since it is based on UTD. Therefore, Figure 3-2 and Figure 3-3 may be seen as the verification of the code developed in MATLAB[®].

Before examining another case for the geometry given in Figure 3-1, an important matter should be pointed about the obstruction losses given in Figure 3-2 and Figure 3-3. When the receiver antenna height exceeds 10λ , receiver antenna passes the incident shadow boundary. This is given in Figure 3-4. Therefore, besides the diffracted fields, incident GO fields also exist. It seems that the loss decreases, when the receiver antenna height exceeds 10λ in Figure 3-2 and Figure 3-3; however, the total field increases due to the incident GO fields. A similar situation is given in Figure 2-35. In Figure 2-35, the ISB occurs at 206.5° and the maximum diffracted field is at the ISB and then it decreases when going to the 0° ; however, the total field is increasing.

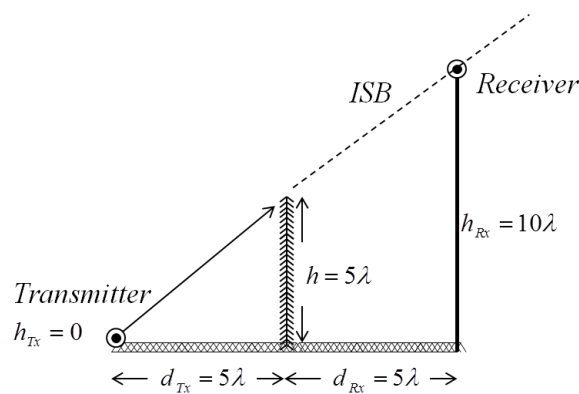


Figure 3-4 Incident shadow boundary for the case $d_{Tx} = d_{Rx} = h = 5\lambda$ and $h_{Tx} = 0$

Another case for the geometry in Figure 3-1 can be described as varying the d_{Tx} , d_{Rx} and h values for the fixed receiver and transmitter antenna heights. Let the fixed antenna heights be 0 to compare the previous case. Loss versus d_{Tx} , d_{Rx} and h , in terms of λ , is plotted in Figure 3-5 and in Figure 3-6, for *soft* and *hard* polarization, respectively.

For this case, the symmetry in Figure 3-1 is conserved and the effect of d_{Tx} , d_{Rx} and h is analyzed for both polarization when $h_{Tx} = h_{Rx} = 0$. In other words, the losses in Figure 3-5 and in Figure 3-6 can be considered as the enlargement effect of Figure 3-1. It should be noted that for the case $d_{Tx} = d_{Rx} = h = 5\lambda$ in Figure 3-5 and in Figure 3-6, the path losses are 38 dB and 22 dB, respectively. These values are consistent with the loss values given in Figure 3-2 and in Figure 3-3.

Unlike Figure 3-2 and Figure 3-3, in Figure 3-5 and Figure 3-6 there is no difference between Keller's method and the UTD code developed in MATLAB[®]. Because when $h_{Tx} = h_{Rx} = 0$, regardless of the d_{Tx} , d_{Rx} and h values, the receiver antenna is always far away from the ISB. According to the results obtained by comparing Figure 3-2 and Figure 3-3 and also by comparing Figure 3-5 and Figure 3-6, it is clear that the MATLAB[®] code based on UTD covers the Keller's diffraction formula. Therefore, there is no need to use Keller's diffraction formula any more, only the UTD code developed in MATLAB[®] will be used after this point of this thesis.

Up to now, all obstruction loss values are calculated by using d_{Tx} , d_{Rx} , h_{Tx} , h_{Rx} and h as input parameters. However, according to the reciprocity principle, there is no need to investigate the effect of these parameters independently [1]. Since the path loss would be the same when the transmitter and receiver are interchanged, changing the transmitter antenna height or changing the transmitter antenna height has the same effect on path loss.

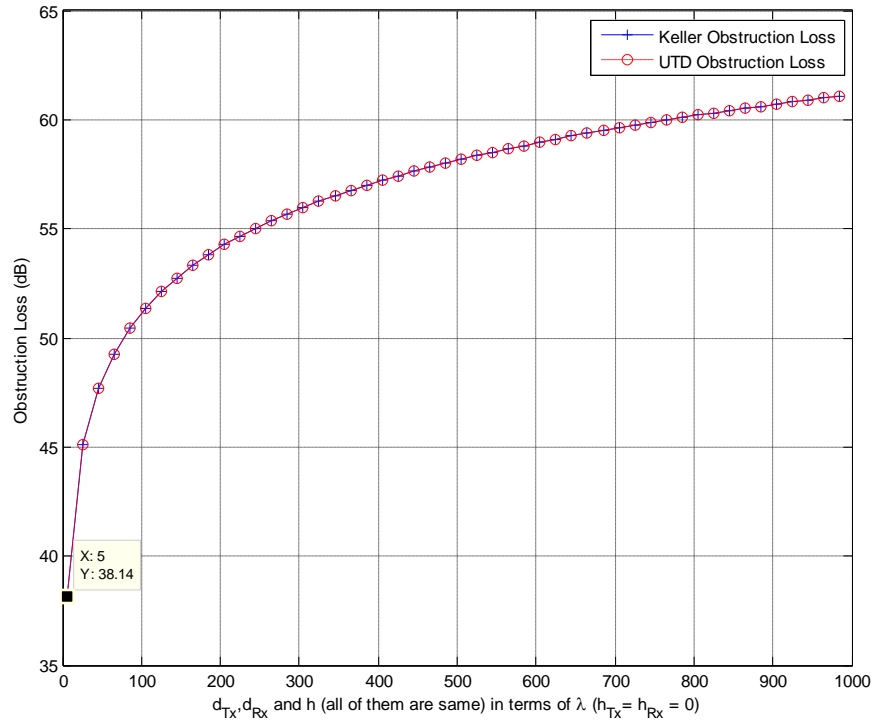


Figure 3-5 Obstruction loss calculated by both Keller's method and the code developed in MATLAB[®] (*soft polarization*)

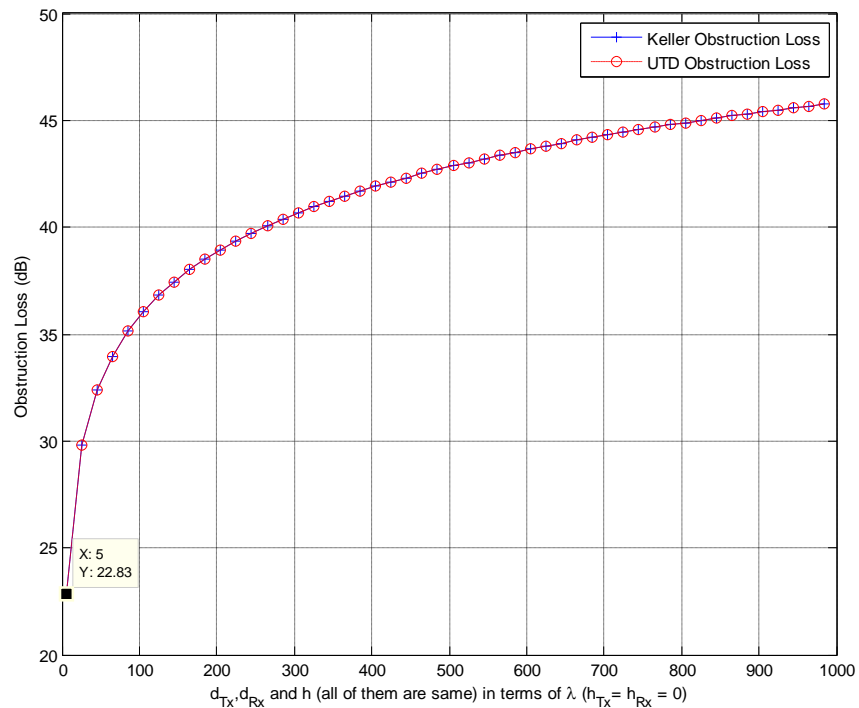


Figure 3-6 Obstruction loss calculated by both Keller's method and the code developed in MATLAB[®] (*hard polarization*)

The first symmetry mentioned above is about the antenna heights. The configuration to investigate the antenna height symmetry is given in Figure 3-7. The distances and heights of antennas and obstruction are also defined in Figure 3-7. The obstruction loss is calculated for both of the cases.

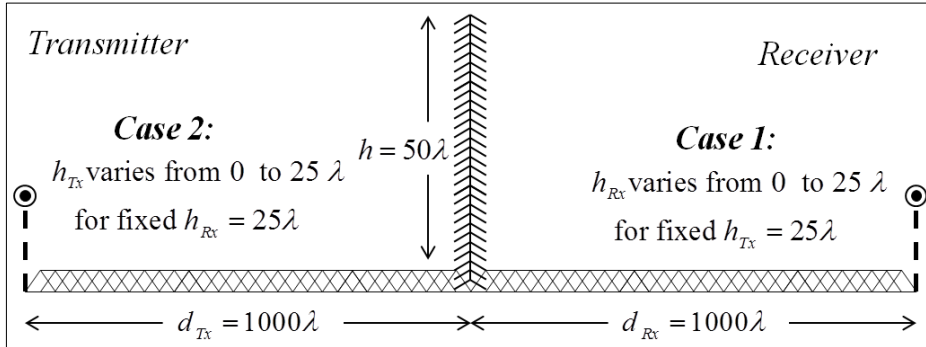


Figure 3-7 Configuration to examine the antenna height symmetry

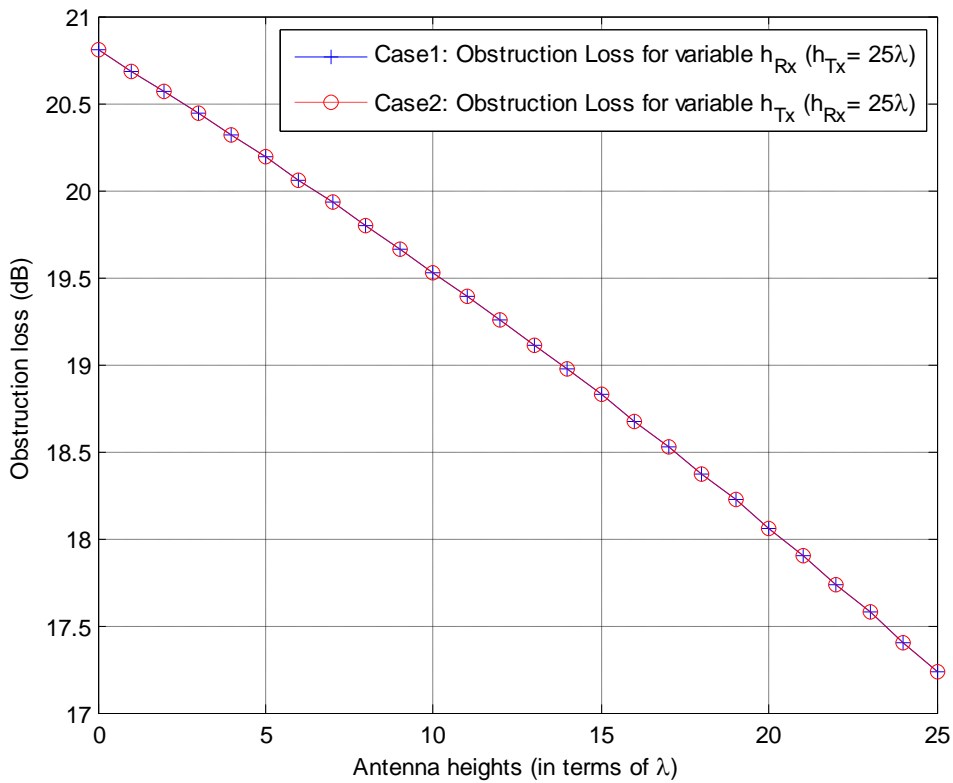


Figure 3-8 Obstruction loss for both of the cases given in Figure 3-7 (*soft pol.*)

Obstruction loss calculated for soft polarization is given in Figure 3-8. It can be seen from Figure 3-8, for both of the cases, obstruction loss is exactly same; therefore, varying Tx or Rx antenna heights has the same effect on obstruction loss.

The second symmetry mentioned above is about the antenna distances, d_{Tx} and d_{Rx} . The configuration to investigate the antenna distance symmetry is given in Figure 3-9. The obstruction loss is calculated for both of the cases.

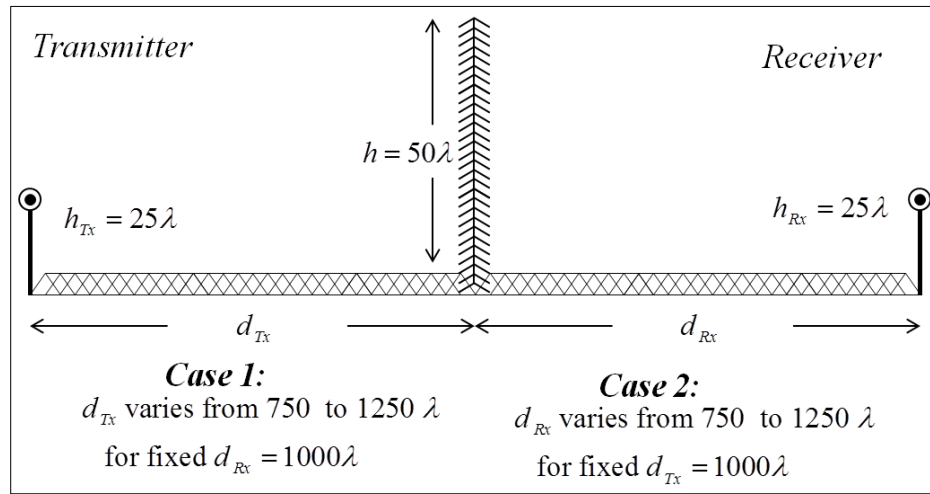


Figure 3-9 Configuration to examine the antenna distance symmetry

For both of the cases given in Figure 3-9, obstruction loss is calculated for soft polarization by using the UTD code developed in MATLAB[®] and the Keller's method. They are given in Figure 3-10 and in Figure 3-11, respectively. In Figure 3-10, there is a slight difference between the calculated obstruction losses. The difference is in the order of 0.01 dB; therefore, it can be neglected. Actually, even the receiver is far away from the ISB or RSB, still UTD Fresnel transition function has still a very slight effect on loss calculation. There is no such a transition function effect in Figure 3-11, Keller's formula; therefore, both are exactly same. Since 0.01 dB is very very small and the fact that it is a result of transition function in UTD, the difference can be neglected. Therefore, distance symmetry is satisfied.

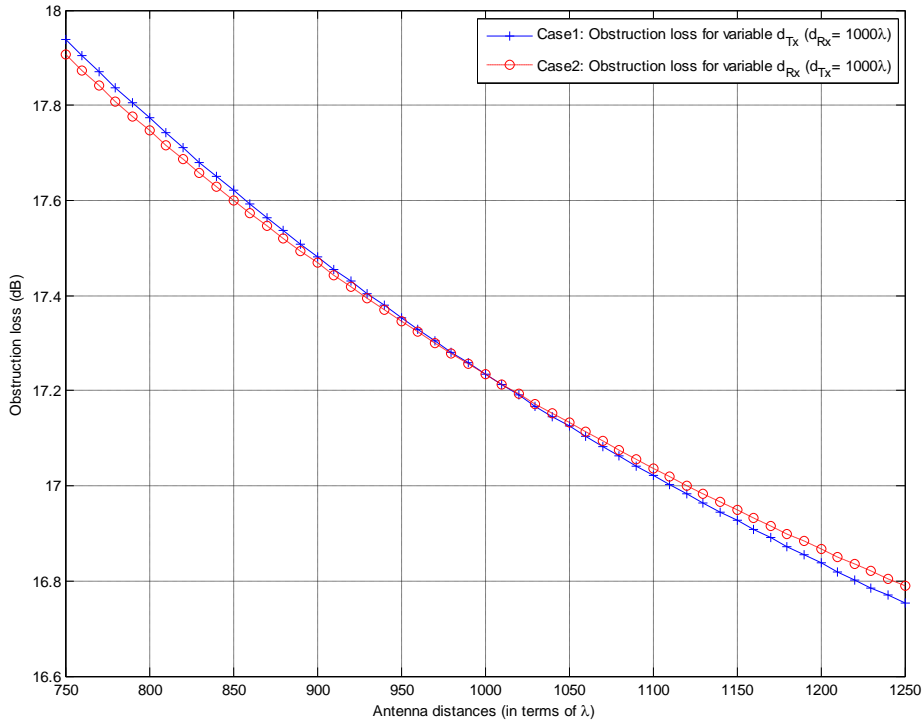


Figure 3-10 For Figure 3-9, loss calculated by UTD based MATLAB[®] code

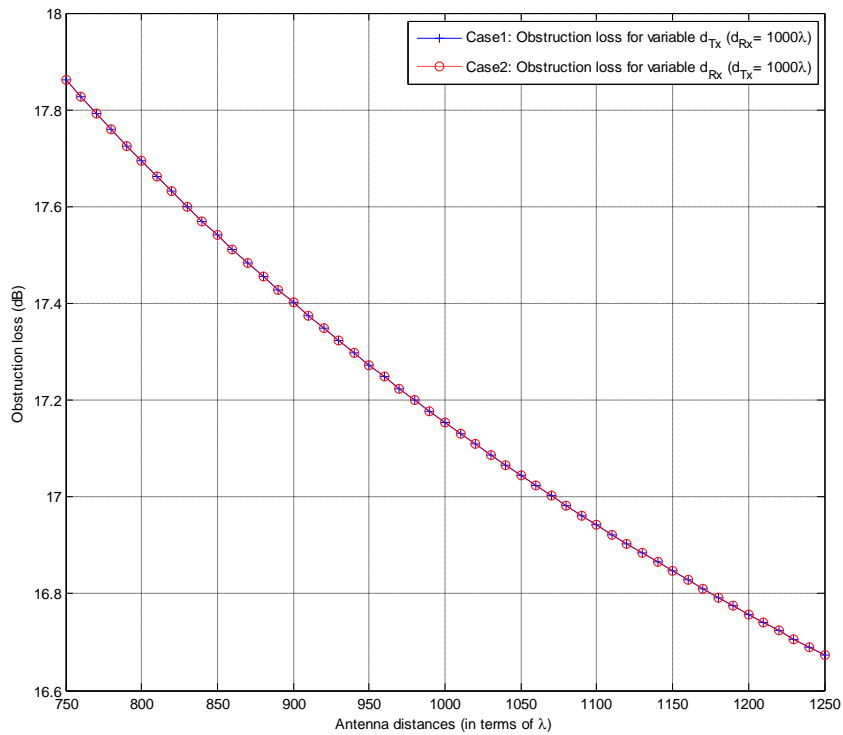


Figure 3-11 For Figure 3-9, loss calculated by Keller's formula

To sum up, although it seems that the obstruction loss depends on 5 independent input parameters (d_{Tx} , d_{Rx} , h_{Tx} , h_{Rx} and h), due to the reciprocity principle demonstrated in Figure 3-8, Figure 3-10 and Figure 3-11, the obstruction loss depends on 3 different parameters: d_{Rx} , h_{Rx} and h . As mentioned before, this does not mean the transmitter antenna distance or height is not important. They should be also taken into account when calculating the obstruction loss; however, the effects of parameters of the transmitter side are exactly same with the parameters of the receiver side. Also both in the real life and solving the optimization problems, one of the transmitter or receiver is accepted as fixed located and the other one is optimized by using this information. In this thesis, the transmitter side is accepted as fixed in terms of both distance and antenna height. Optimization will be made at the receiver side.

Before examining the effect of altering receiver side parameters, another important parameter, the height of the obstruction, should be discussed about Figure 3-1. The obstruction loss values calculated by using the UTD code developed in MATLAB[®] given in Figure 3-13 and in Figure 3-14 for soft and hard polarization, respectively. Parameters other than the obstruction height are chosen as in Figure 3-12. As expected, loss increases when the obstruction height increases. Obstruction height starts with 26λ in order to ensure that receiver is at the diffracted region. The difference between polarizations is very significant for large h values.

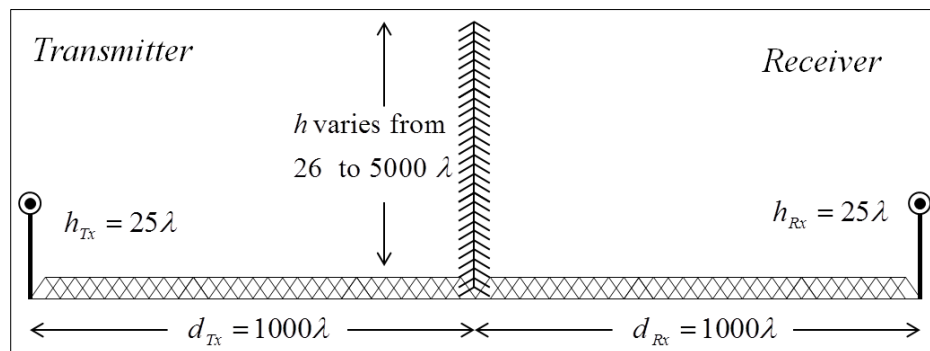


Figure 3-12 Other parameters when investigating the effect of obstruction height

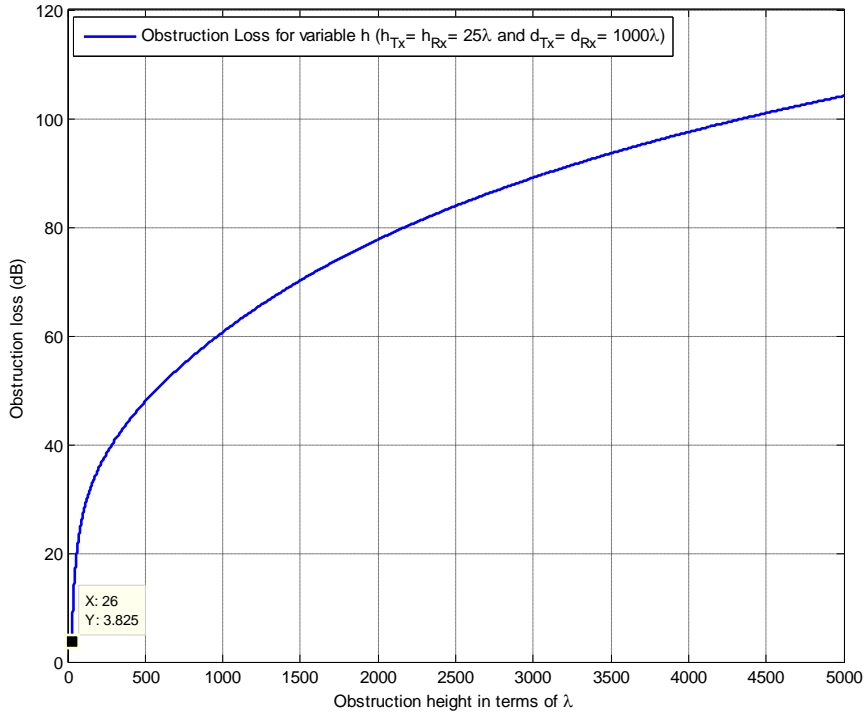


Figure 3-13 Loss calculated by the code developed in MATLAB[®] (*soft pol.*)

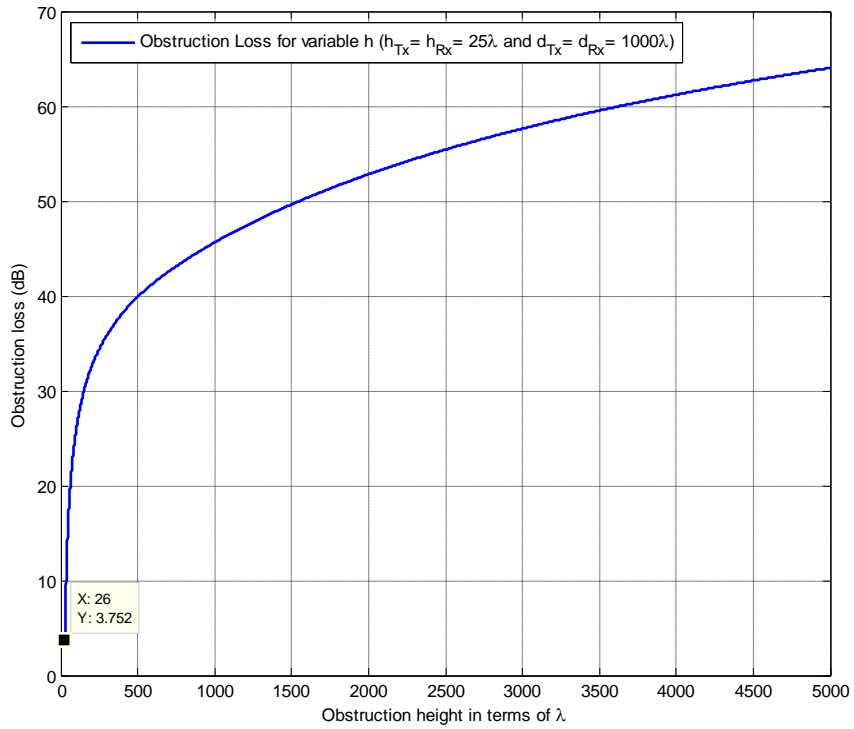


Figure 3-14 Loss calculated by the code developed in MATLAB[®] (*hard pol.*)

The remaining parameters are about the receiver side. They are d_{Rx} and h_{Rx} . While the other parameters (d_{Tx} , h_{Tx} and h) are fixed, the effects of these two parameters on the obstruction loss will be analyzed. The values of the d_{Tx} , h_{Tx} and h parameters and the design in order to analyze the effect of varying d_{Rx} and h_{Rx} are shown in Figure 3-15.

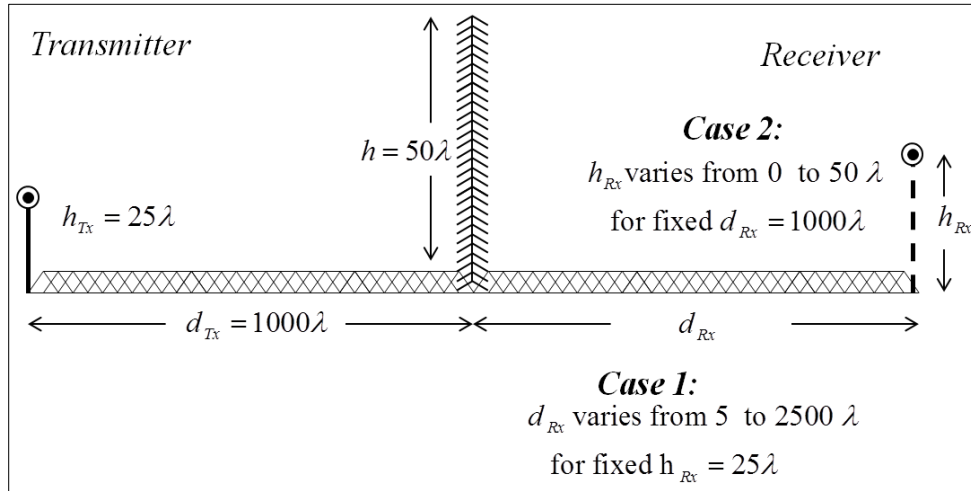


Figure 3-15 Configuration to examine the effect of receiver parameters, d_{Rx} and h_{Rx}

In Figure 3-16 and Figure 3-17, the obstruction loss values calculated by using the UTD code developed in MATLAB[®] is given for soft and hard polarization, respectively. Some important results should be discussed about Figure 3-16 and Figure 3-17. First of all, when d_{Rx} is small, there is a significant difference between soft and hard polarizations for the same d_{Rx} ; however, the difference becomes smaller for large d_{Rx} values. Another important result is that when d_{Rx} increases, the obstruction loss decreases. It is an acceptable result because, as always emphasized, the calculated obstruction loss is the loss over free space loss. Therefore, it is reasonable that the effect of the obstruction decreases, when the receiver goes far away from the obstruction. In other words, the receiver avoids the “shadowing effect” of the obstruction.

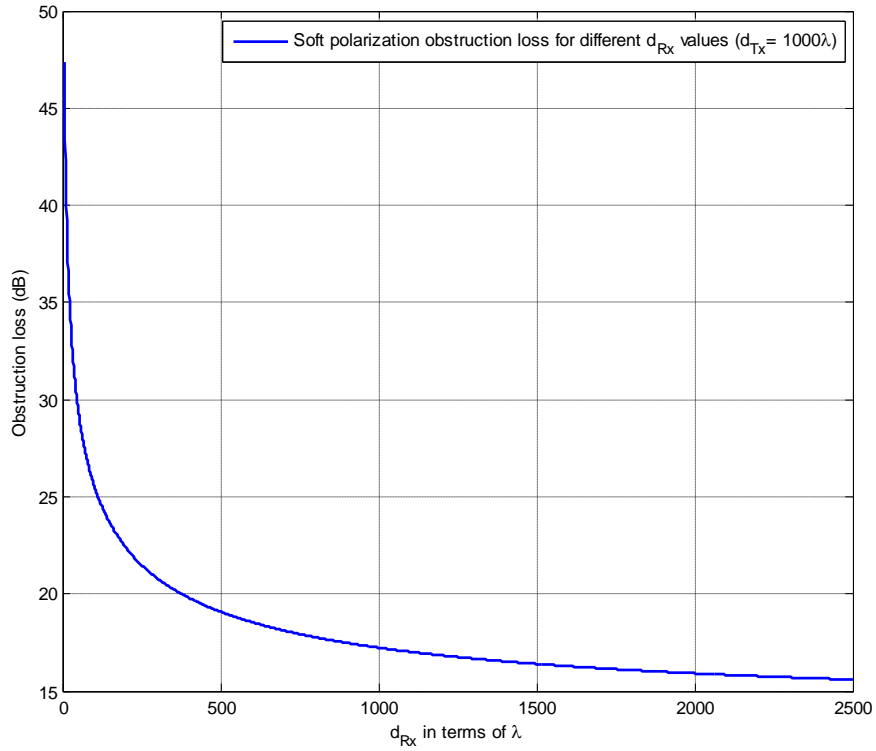


Figure 3-16 Obstruction loss vs. d_{Rx} calculated by MATLAB[®] (*soft pol.*)

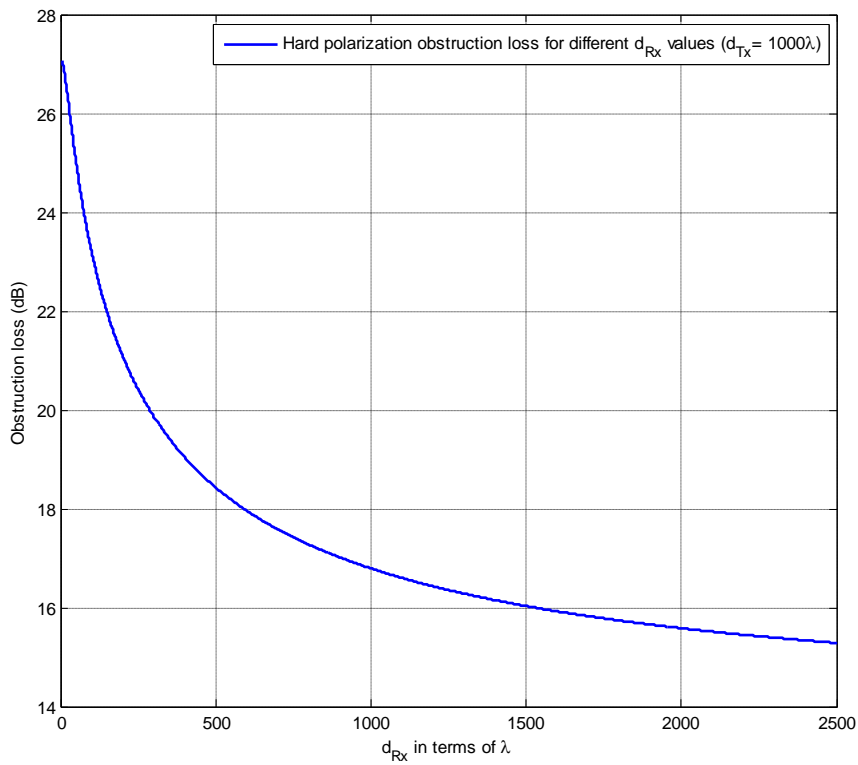


Figure 3-17 Obstruction loss vs. d_{Rx} calculated by MATLAB[®] (*hard pol.*)

However, decreasing obstruction loss does not mean the total loss is also decreasing, since the total loss includes both free space and obstruction losses. The free space loss starts with a constant value when the receiver is very close to obstruction and it increases almost linearly when the distance between the obstruction and receiver increases. Therefore, it is possible to make an optimization by the help of the sudden decline of obstruction loss given in Figure 3-16 and Figure 3-17. In Figure 3-18, the total loss is calculated for both of the polarizations of case-1 given in Figure 3-15.

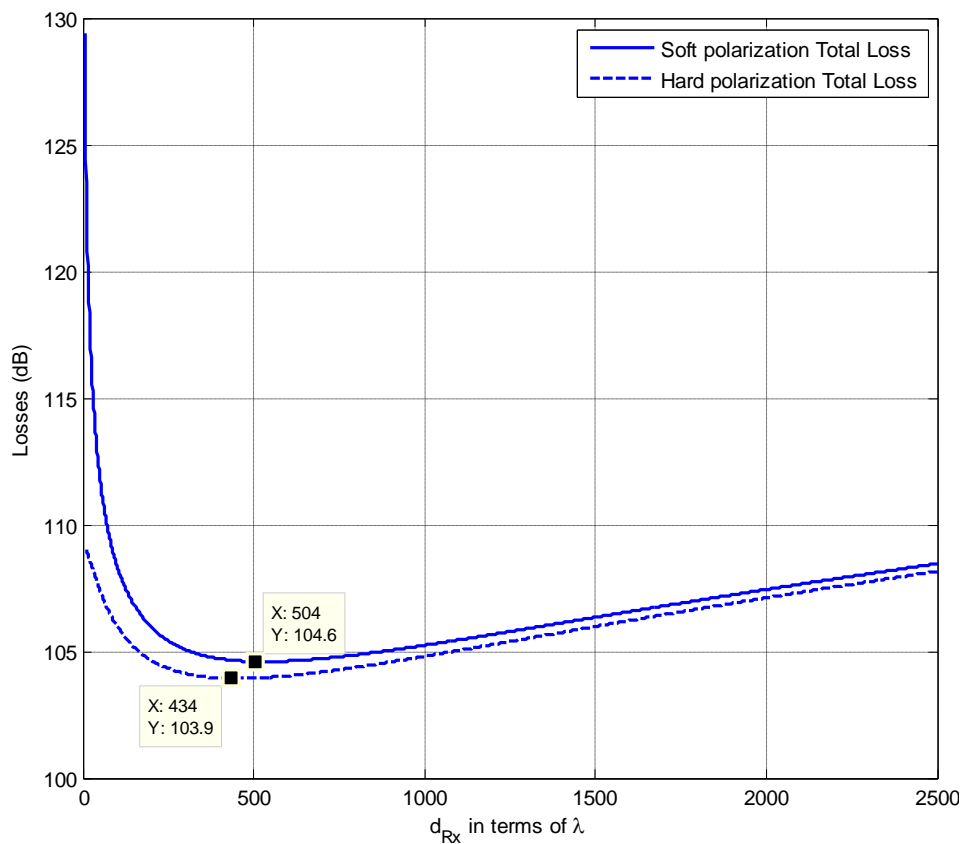


Figure 3-18 Receiver antenna distance optimization for the case-1 given in Figure 3-15 in order to minimize the total loss

In Figure 3-18, it can be seen that receiver antenna distance from the obstruction should be approximately 450λ for hard polarization and 500λ for soft polarization in order to obtain the minimum total loss.

The second parameter about the receiver is h_{Rx} . It varies as Case-2 shown in Figure 3-15. In Figure 3-19 and Figure 3-20, the obstruction loss values calculated by using the UTD code developed in MATLAB[®] is given for soft and hard polarization, respectively.

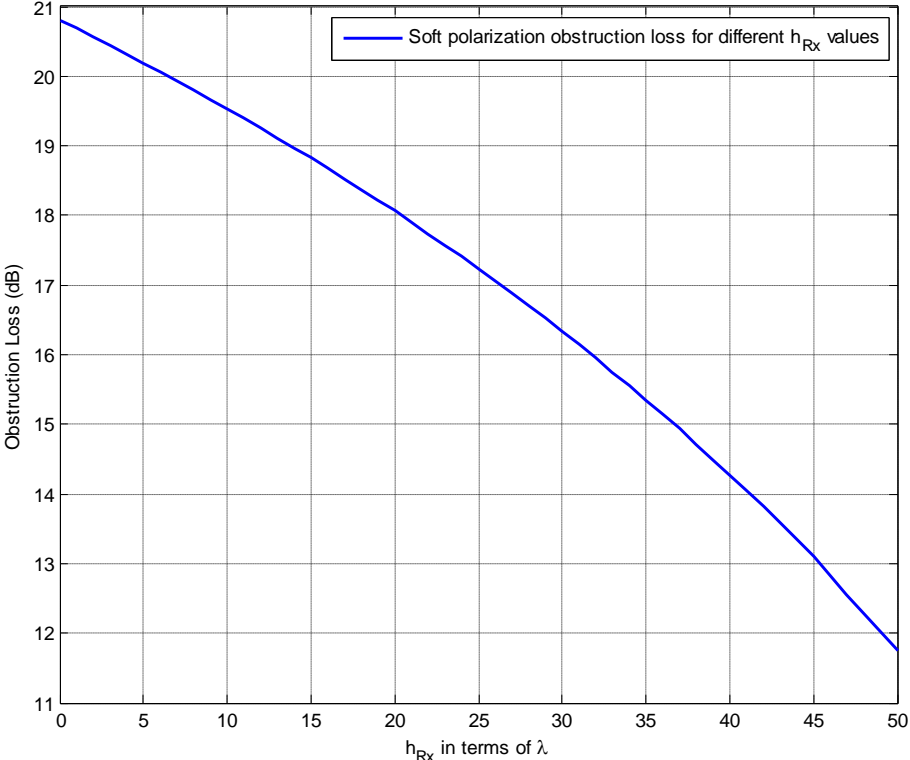


Figure 3-19 Obstruction loss vs. h_{Rx} calculated by MATLAB[®] (*soft pol.*)

As expected, when the receiver antenna height increases loss due to the obstruction decreases for both hard and soft polarization. It is not necessary to optimization by also using the free space loss change. Because free space loss is determined mainly by the $d_{Tx} + d_{Rx}$ distance that is a fixed distance, free space loss is almost constant. For soft polarization case, the obstruction, free space and total losses are plotted in Figure 3-21. It is clear that free space loss has an effect as adding a constant value to the obstruction loss.

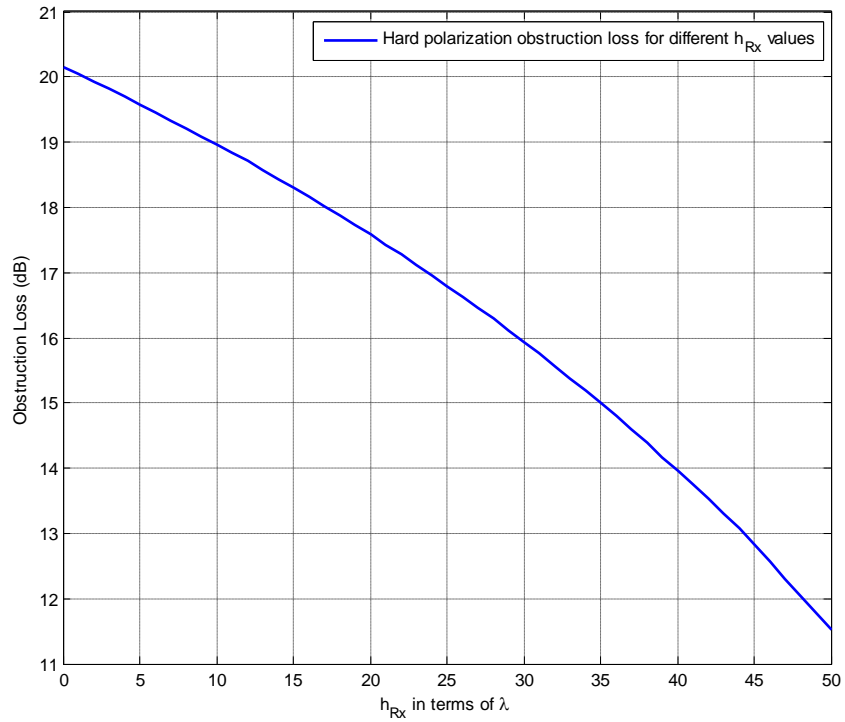


Figure 3-20 Obstruction loss vs. h_{Rx} calculated by MATLAB[®] (*hard pol.*)

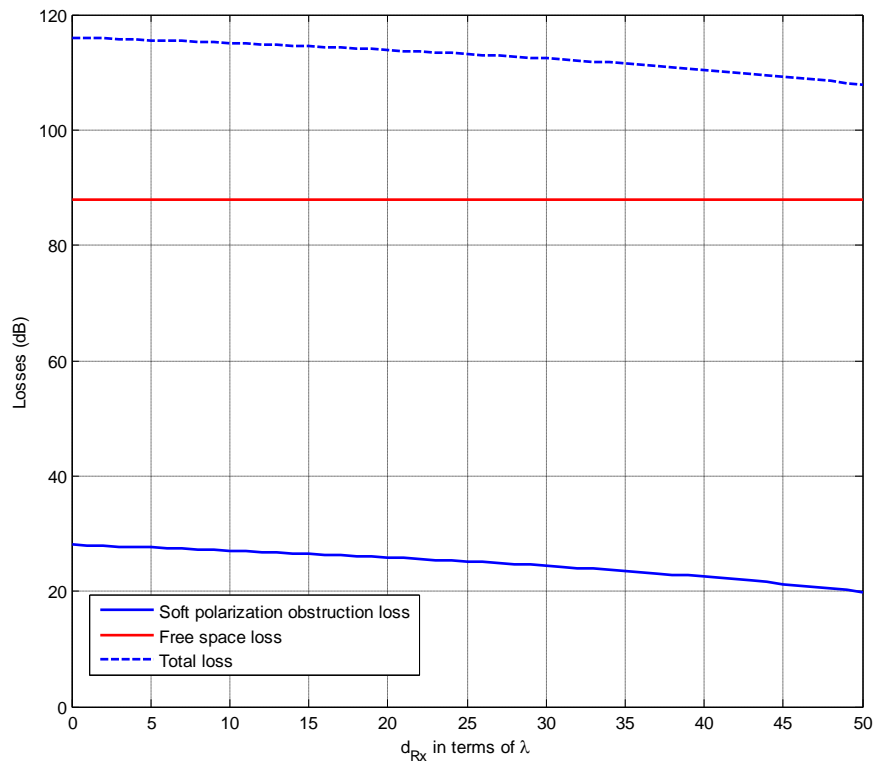


Figure 3-21 Total loss for the case-2 given in Figure 3-15 for soft polarization

3.1.2 A Mountain Modeled as a Wedge with a Nonzero Angle

The second case studied in this thesis is a wedge with a nonzero angle given in Figure 3-22. It is clear that the model examined in this part reduces to the previous model with, wedge angle, $WA=0$.

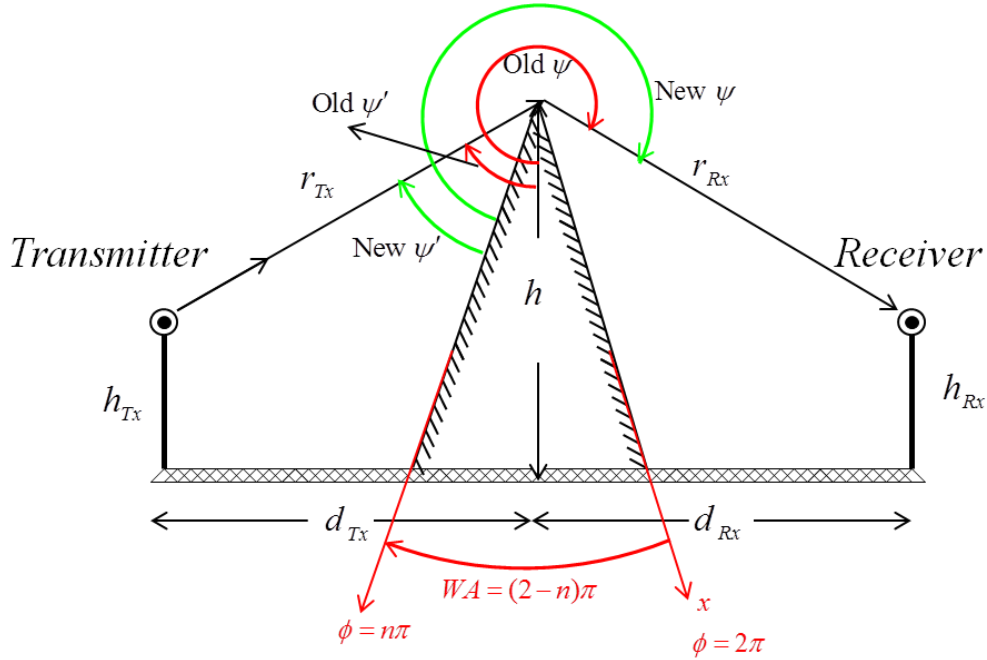


Figure 3-22 Transmitter and receiver antennas on either side of a mountain that can be modeled as a wedge that has a nonzero wedge angle

If the main formulas of GTD, that explain the diffraction mechanism for the case given in Figure 3-22, are rewritten in Eqn. (3.8). If the diffraction mechanisms of half-plane wedge which is given in Figure 3-1 and the nonzero angle wedge which is given in Figure 3-22 are compared by using the Eqn. (3.8). It is noted that the incident field $\vec{E}^i(Q_D)$, spatial attenuation term $A(s',s)$ and phase term $e^{-j\beta s}$ are the same for both of the cases. Therefore, the only different term in Eqn. (3.8) is D, diffraction coefficient, calculated by using the code developed in MATLAB[®].

$$\begin{aligned}
\vec{\mathbf{E}}^d(s) &= \vec{\mathbf{E}}^i(Q_D) \cdot \vec{\mathbf{D}} A(s', s) e^{-j\beta s} \\
\vec{\mathbf{E}}^i(Q_D) &= \frac{e^{-j\beta r_{Tx}}}{r_{Tx}}, e^{-j\beta s} = e^{-j\beta r_{Rx}} \\
A(s', s) &= \sqrt{\frac{s'}{s(s'+s)}} = \sqrt{\frac{r_{Tx}}{r_{Rx}(r_{Tx} + r_{Rx})}}
\end{aligned} \tag{3.8}$$

The MATLAB[®] code has five input parameters. These are observation distance, source and observation angles, incident field angle to the wedge (it is always 90° for point to point 2-D propagation) and wedge angle. Since wedge angle, WA, is always zero for the PEC wedge case, it is not defined as an input parameter in the previous part. Naturally, it should be taken into account for the general case. Also the source and observation angles are modified. In Figure 3-22, the old and new values of ψ and ψ' are shown by the red and green, respectively. It is clear that the difference between the old and new values of ψ and ψ' is equal to $WA/2$. And n can be written as in the following Eqn. (3.9)

$$n = \frac{360 - \text{Wedge Angle}}{180} \tag{3.9}$$

Another intuitive method to find out the $WA/2$ decrease in the angles is that imagine that PEC wedge is spread out from the x -axes. It seems that for this case, angles are decreased by an amount of WA ; however, in order to conserve system orientation both source and receiver should be rotated by $WA/2$. Therefore, Eqn. (3.10) can be written.

$$\phi_{new} = \phi_{old} - WA + \frac{WA}{2} = \phi_{old} - \frac{WA}{2} \tag{3.10}$$

Throughout this thesis, all formulations are given for exterior wedge, not for interior wedge. Since the exterior wedge can be used the modeling mountains.

In the half-plane wedge case, it was shown that some of the parameters given in Figure 3-22 have the same effects on the obstruction loss. Details of the previous work will not be covered in this part and the “independent” parameters in the sense of receiver optimization which are d_{Rx} , h_{Rx} and h will be discussed here.

Before examining the receiver side parameters, for the sake of completeness, the effect of the obstruction height, h , will be discussed. In a similar manner with the half plane wedge case, it is expected that the obstruction loss increases when the height of the obstruction increases. However, there is a significant difference in comparison with the half plane wedge case. The height of the obstruction should exceed d_{Tx} or d_{Rx} , since the input parameters are WA and h , the size of the obstruction is determined by these parameters. Therefore for a fixed WA , increasing the height of the obstruction enlarges the obstruction in horizontal axes. Then, as a mathematical error, the transmitter or receiver may be located on the mountain. Therefore, h varies from 26 to 950λ in this case.

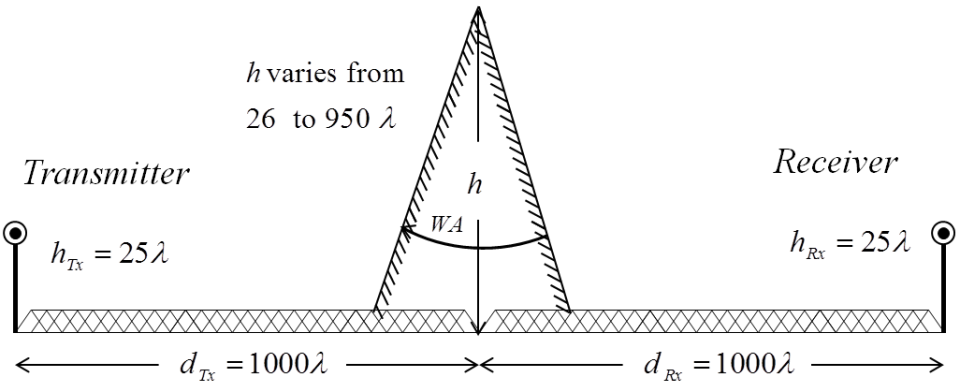


Figure 3-23 Configuration to investigate the effect of obstruction height

The WA values are selected 0° , 30° , 60° and 90° . Parameters other than the obstruction height are chosen as in Figure 3-23. The obstruction loss values calculated by using the UTD code developed in MATLAB[®] given in Figure 3-24 and in Figure 3-25 for soft and hard polarization, respectively.

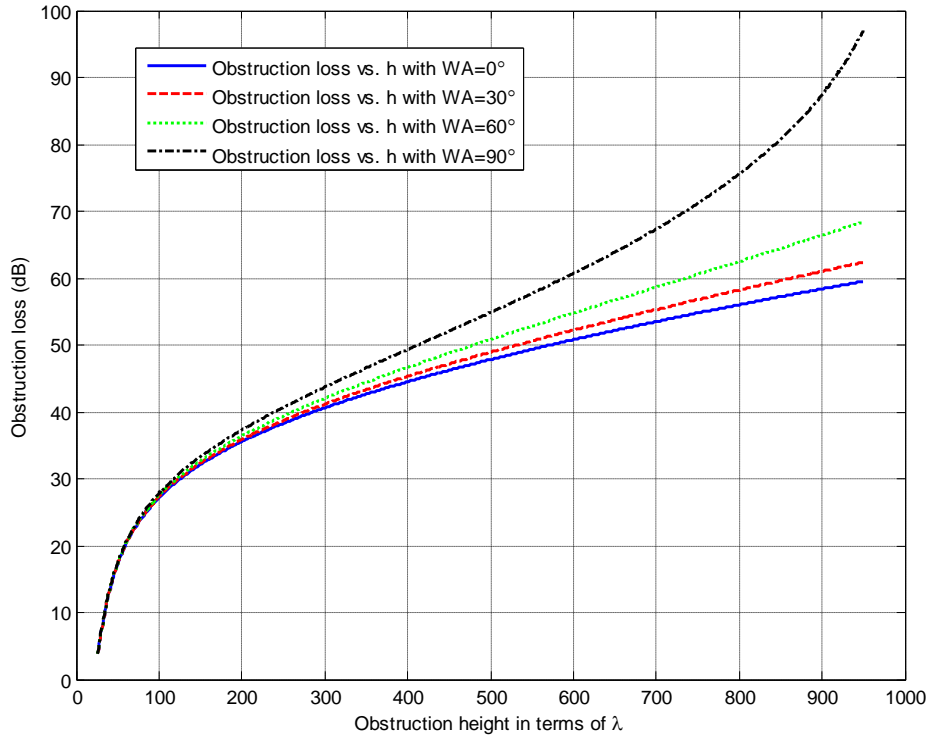


Figure 3-24 Loss calculated by MATLAB[®] vs. h for different WA (*soft pol.*)

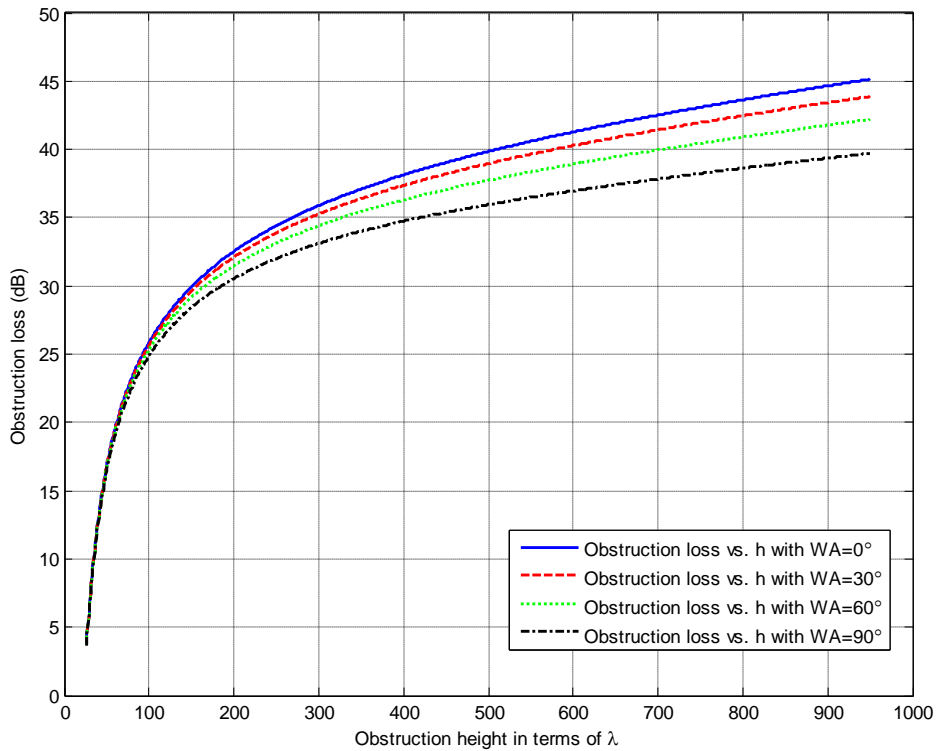


Figure 3-25 Loss calculated by MATLAB[®] vs. h for different WA (*hard pol.*)

As expected, loss increases when the obstruction height increases. Obstruction height starts with 26λ in order to ensure that receiver is at the diffracted region. WA determines the effect of height increment on horizontal enlargement. For example, for $WA=90^\circ$ case, the obstruction is closer to the antennas than the case $WA=60^\circ$. Therefore for large values of obstruction height, the loss increases rapidly. Due to reason discussed above, it is more detectable for large WA .

Another difference between the polarizations is that for the same obstruction height, loss is proportional to WA for soft polarization; however, it is inversely proportional to WA for hard polarization. Although for large obstruction heights, the explanations above are quite correct and sufficient, for small obstruction heights comparable to antenna heights, for example $h = 50\lambda$, the plots given in Figure 3-24 and Figure 3-25, the relationship between WA and obstruction loss is not clear. To investigate this relationship, the configuration given in Figure 3-26 is used. It is similar to the Figure 3-23.

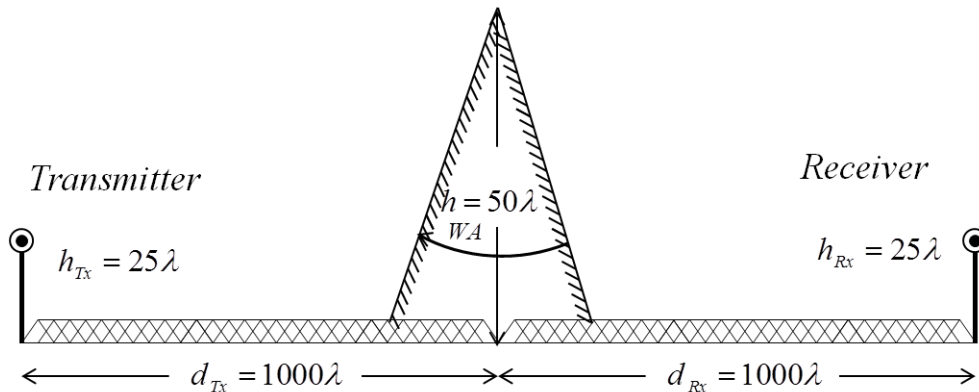


Figure 3-26 All height values are fixed only WA angle differs

The WA starts from 0° to 90° . Parameters other than WA are fixed and given in Figure 3-26. The obstruction loss values calculated by using MATLAB[®] code are given in Figure 3-27 and in Figure 3-28 for soft and hard polarizations, respectively. For small heights, similar to the large heights, loss is proportional to WA for soft polarization; however, it is inversely proportional to WA for hard polarization.

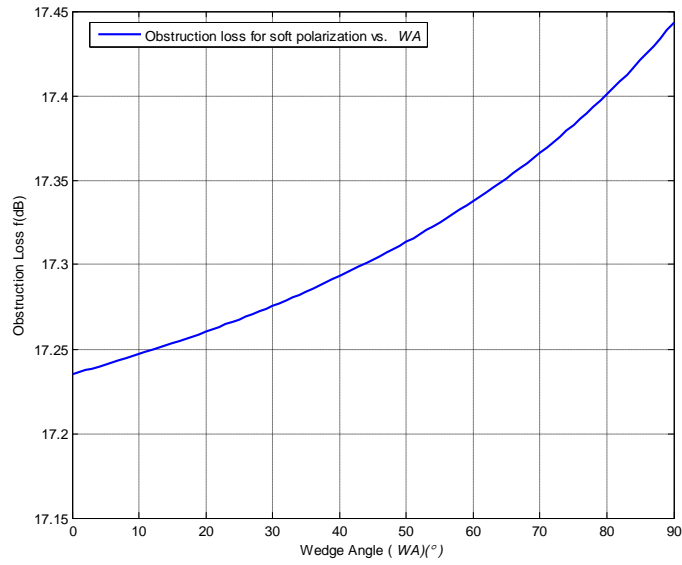


Figure 3-27 Loss calculated by MATLAB[®] vs. WA for Figure 3-26 (*soft pol.*)

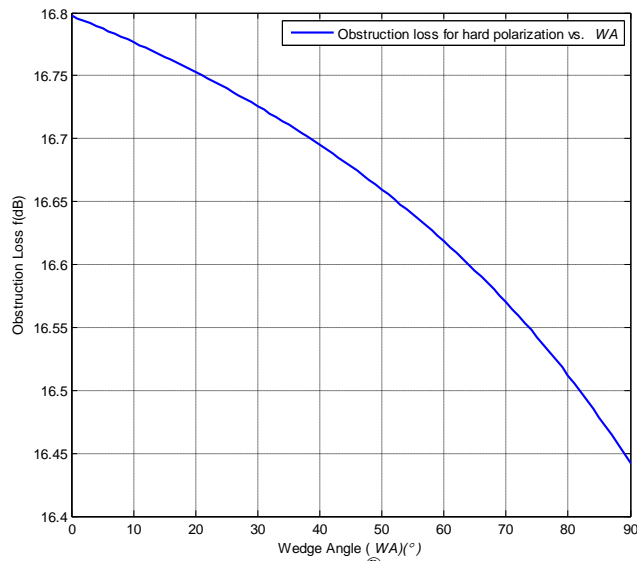


Figure 3-28 Loss calculated by MATLAB[®] vs. WA for Figure 3-26 (*hard pol.*)

It can be seen that, from Figure 3-24, Figure 3-25, Figure 3-27 and Figure 3-28; WA variation from 0° to 90° results in approximately 0.5 dB obstruction loss difference when $h = 50\lambda$. However, same WA variation results in almost 5 dB difference when $h = 600\lambda$. These values are for $d_{Tx} = d_{Rx} = 1000\lambda$ and $h_{Tx} = h_{Rx} = 25\lambda$.

Only the parameters about the receiver side are not discussed up to now for a nonzero angle wedge. These are d_{Rx} and h_{Rx} . While the other parameters (d_{Tx} , h_{Tx} and h) are fixed, the effects of these two parameters on the obstruction loss will be analyzed. The values of the d_{Tx} , h_{Tx} , h and WA parameters and the design in order to analyze the effect of varying d_{Rx} and h_{Rx} are shown in Figure 3-29.

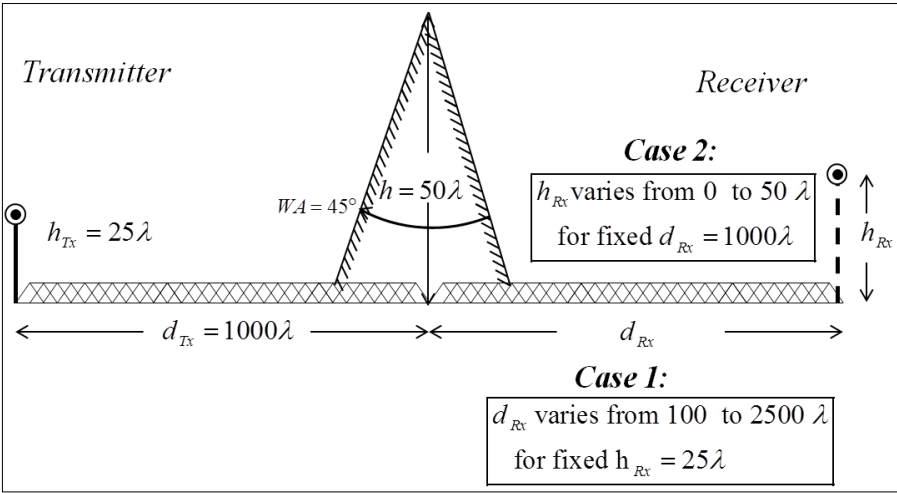


Figure 3-29 Configuration to examine the effect of d_{Rx} and h_{Rx} with 45° wedge

Unlike the half-plane wedge case, d_{Rx} starts from 100λ instead of 5λ due to the nonzero width of the wedge. It is expected from the half-plane wedge case that when d_{Rx} increases, the obstruction loss decreases. It was explained in the half-plane wedge case as the fact that the receiver avoids the “shadowing effect” of the obstruction. The obstruction loss for the case-1 in Figure 3-29 is plotted in Figure 3-30 for both soft and hard polarizations. The result is consistent with the result of half plane wedge.

The relationship between WA and h was previously discussed. Similarly the relationship between WA and receiver antenna distance, d_{Rx} , will be discussed.

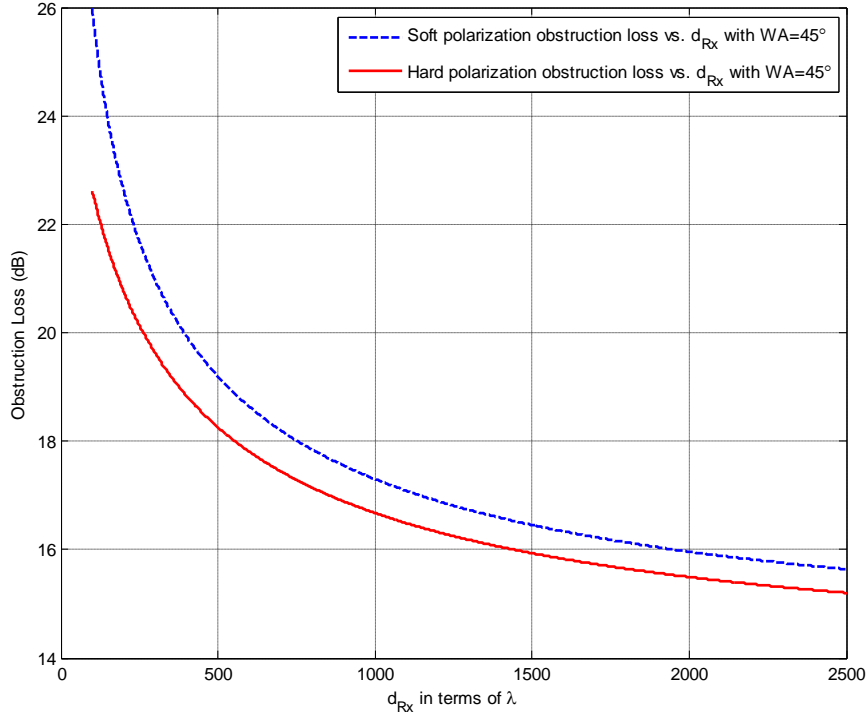


Figure 3-30 Soft and hard obstruction loss vs. d_{Rx} with $WA=45^\circ$

The relationship between WA and receiver antenna distance, d_{Rx} , is given in Figure 3-31 and Figure 3-32 for both soft and hard polarizations, respectively. It can be concluded from Figure 3-31 and Figure 3-32 that when the transmitter parameters, the height of the obstruction and receiver antenna are (d_{Tx} , h_{Tx} , h_{Rx} and h) fixed, the WA variation from 0° to 90° results in approximately 0.3 dB obstruction loss difference when d_{Rx} is large. Furthermore, same WA variation results in almost 1.5 dB difference when d_{Rx} is small. These values are obtained for $d_{Tx} = 1000\lambda$, $h_{Tx} = h_{Rx} = 25\lambda$, $h = 50\lambda$.

Consequently, the polarization and wedge angle have no significant effect on the obstruction loss for all values of d_{Rx} for Figure 3-29.

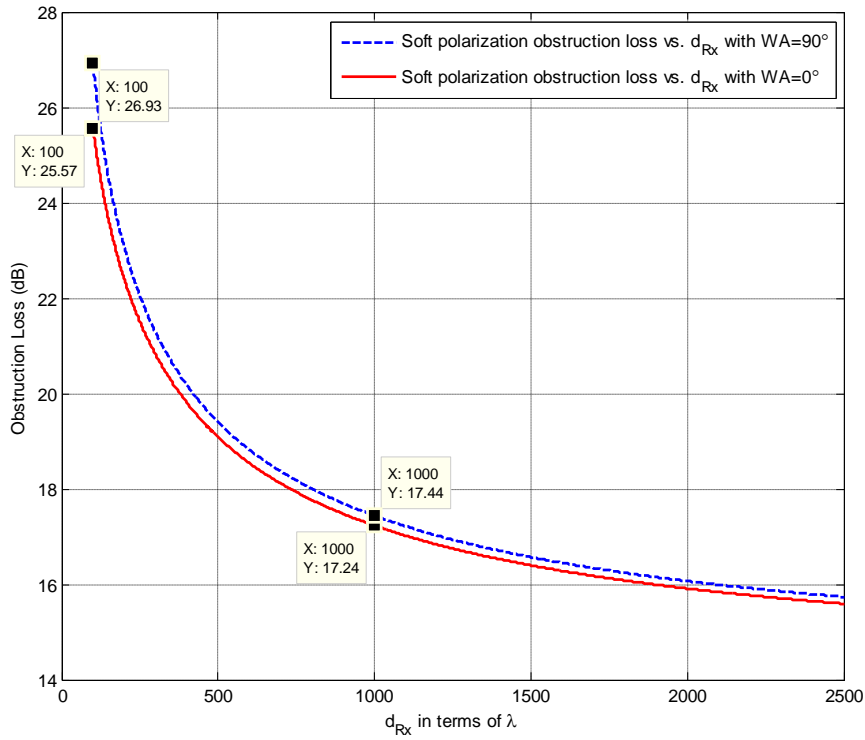


Figure 3-31 Soft polarization obstruction loss vs. d_{Rx} with $WA=0^\circ$ and 90°

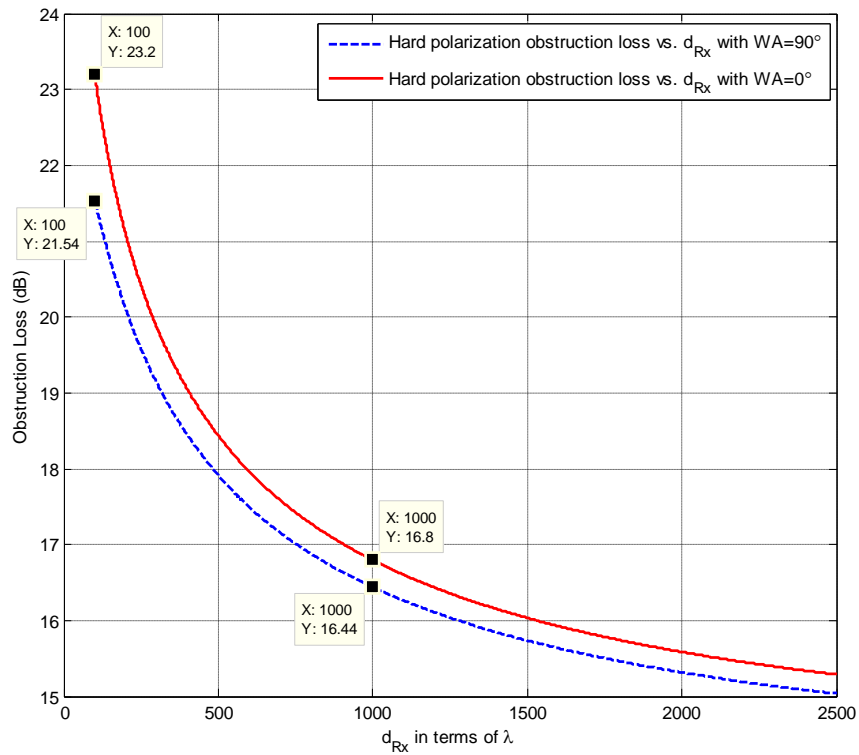


Figure 3-32 Hard polarization obstruction loss vs. d_{Rx} with $WA=0^\circ$ and 90°

The second case (Figure 3-29) is about the receiver antenna height. The obstruction loss is examined when the h_{Rx} varies from 0 to 50λ . In Figure 3-33 and Figure 3-34, the obstruction loss values calculated by using the UTD code developed in MATLAB[®] are given for soft and hard polarizations, respectively. When the receiver antenna height increases, the obstruction loss decreases.

Because free space loss is determined almost entirely by the $d_{Tx} + d_{Rx}$ distance which is independent from h_{Rx} and constant, free space loss is nearly a constant value. For soft polarization case, the obstruction, free space and total losses are plotted in Figure 3-35. Previously the relationships between WA and h and also WA and d_{Rx} were analyzed. The relationship between the last independent parameter h_{Rx} and WA is given in Figure 3-36. It can be observed in Figure 3-36 that the effect of WA increment up to 100° is almost zero. However, when WA approaches to the 150° , the effect increases but still it is limited to approximately 1.5 dB.

Up to this point in this chapter, it is shown that,

- UTD includes Keller's formula. Besides that, it is more powerful at shadow boundaries.
- The code developed in MATLAB[®] based on UTD runs properly.
- Changing the Tx parameters (h_{Tx}, d_{Tx}) or Rx parameters (h_{Rx}, d_{Rx}) has the same effect on obstruction loss so the receiver side is focused. Indeed, one of the Tx or Rx side should be fixed to optimize the other side.
- Increasing the obstruction height (h) increases obstruction loss for both zero and nonzero angle wedges, as expected.
- Increasing the distance between receiver and obstruction (d_{Rx}) decreases loss for both zero and nonzero angle wedges (“*shadowing effect*”).
- Increasing the receiver antenna height (h_{Rx}) decreases loss for both zero and nonzero angle wedges.

These results are obtained for the $d_{Tx} = d_{Rx} = 1000\lambda$, $h_{Tx} = h_{Rx} = 25\lambda$ and $h = 50\lambda$.

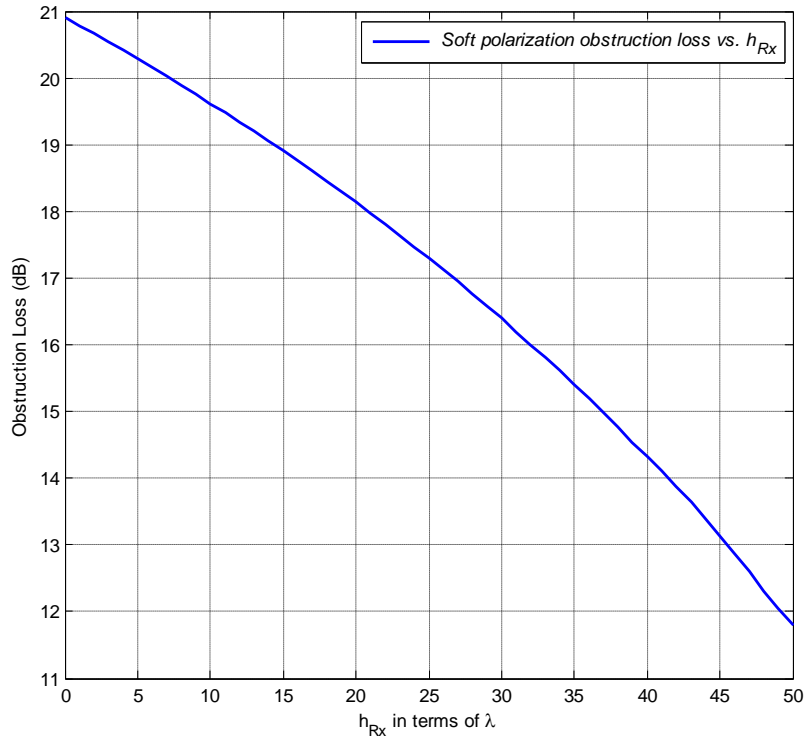


Figure 3-33 Obstruction loss vs. h_{Rx} for the case-2 given in Figure 3-29 (*soft pol.*)

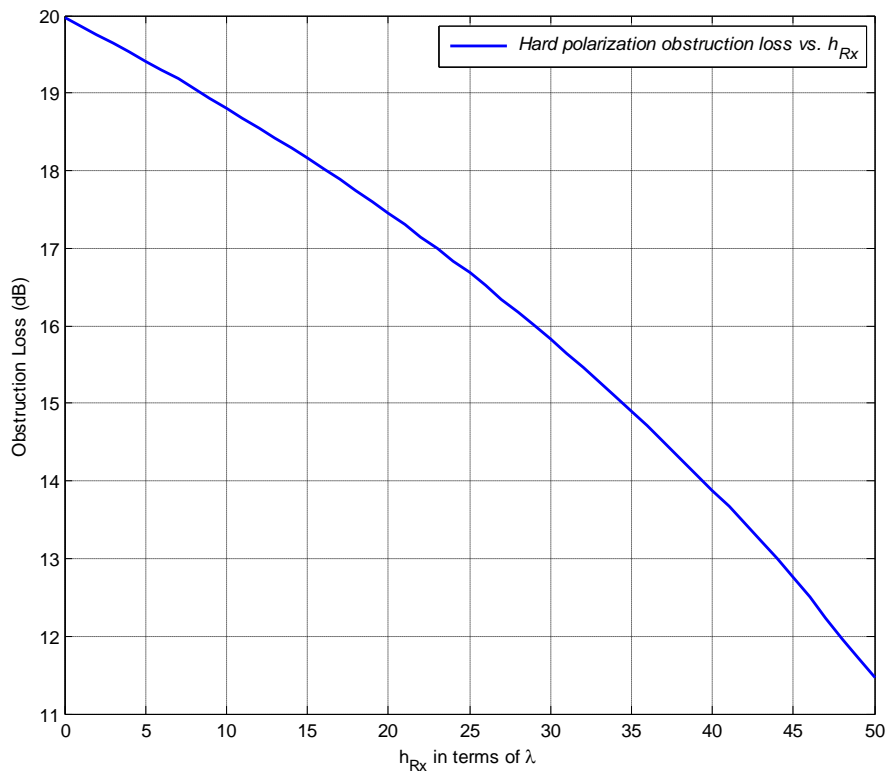


Figure 3-34 Obstruction loss vs. h_{Rx} for the case-2 given in Figure 3-29 (*hard pol.*)

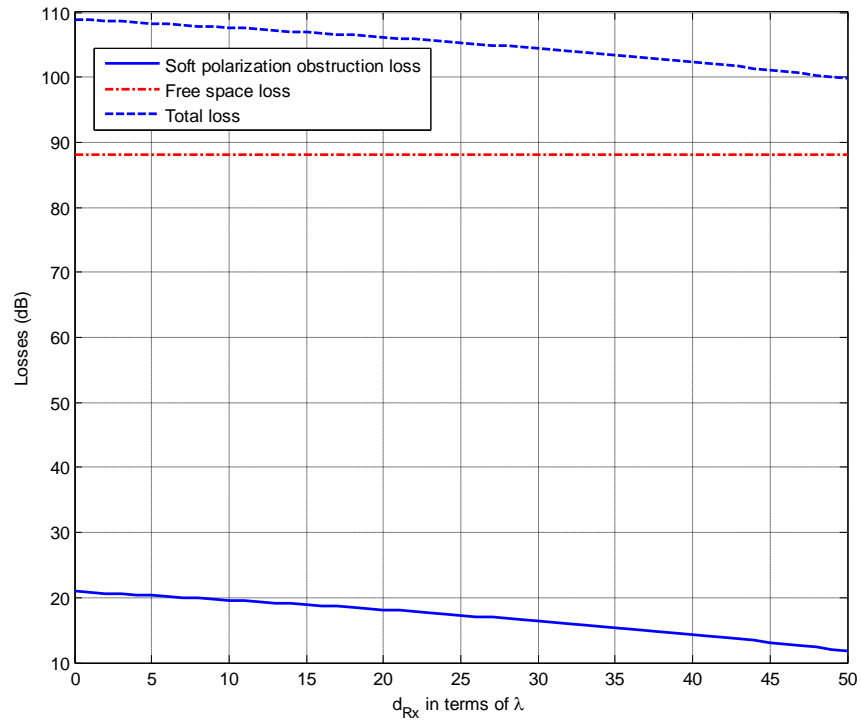


Figure 3-35 Total loss for the case-2 given in Figure 3-29 for soft polarization

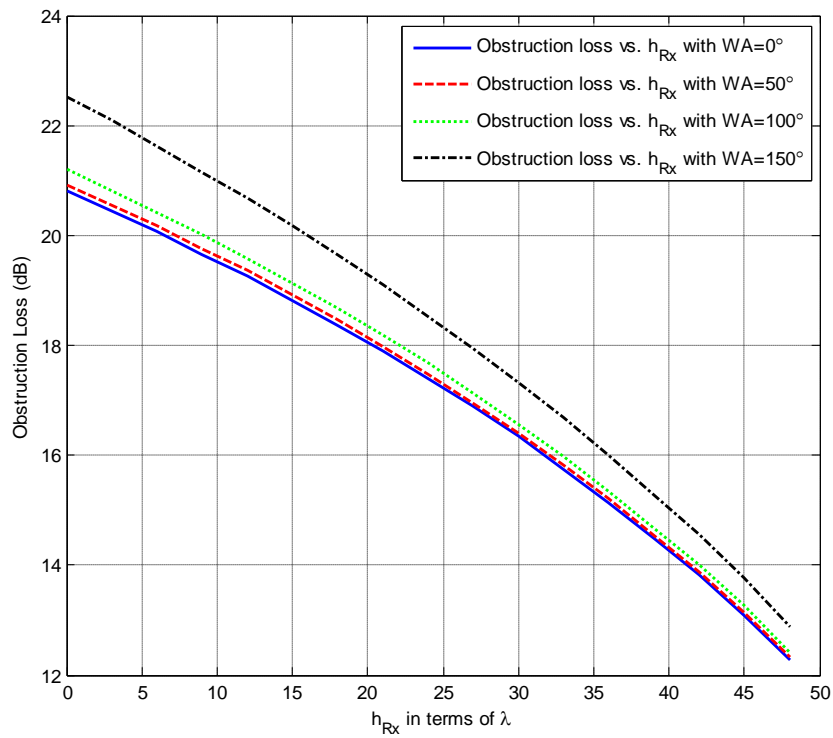


Figure 3-36 Obstruction loss vs. h_{Rx} for the case-2 given in Figure 3-29 for different wedge angles for soft polarization

Another important conclusion obtained up to this point is the effect of wedge angle. It is shown that,

- While all other parameters like h_{Rx} , d_{Rx} and h are fixed, increasing the WA increases the obstruction loss for soft polarization but it decreases loss for hard polarization. However these effects given in Figure 3-27 and Figure 3-28 are negligible ($Loss \leq 0.5 \text{ dB}$ for $d_{Rx} = 1000\lambda$ & $h_{Rx} = 25\lambda$).
- The effect of increasing the WA and its proportionalities with polarizations given above are valid for all d_{Rx} values; however, for small d_{Rx} values loss increases but still it is small ($Loss \approx 1.5 \text{ dB}$ for $d_{Rx} = 100\lambda$ & $h_{Rx} = 25\lambda$ from Figure 3-31 and Figure 3-32).
- Increasing the WA increases the obstruction loss for soft polarization, as mentioned above, is valid for all h_{Rx} values. As it can be seen from Figure 3-36, same amount of increment of WA has the same effect ($Loss \approx 0.1 \text{ dB}$) on obstruction loss for almost all h_{Rx} values. Also it should be noted that when WA approaches to 180° , loss increases rapidly but still it is very small ($Loss \approx 1 \text{ dB}$ for $WA = 150^\circ$).

for $d_{Tx} = d_{Rx} = 1000\lambda$, $h_{Tx} = h_{Rx} = 25\lambda$ and $h = 50\lambda$ case given in Figure 3-26.

3.2 LONGLEY-RICE MODEL IN HILLY TERRAIN

In the previous part, the use of GTD in the modeling of propagation path loss is described in a detailed way. Since GTD is totally based on physical theories, it is difficult to take into account some kind of daily parameters that can affect the propagation path loss. For example, weather conditions can affect electromagnetic wave propagation or vegetation on a hill may also make difficult to obtain receive fields. If one can succeed to model for a specific region of the Earth, for example deserts; the parameters may affect the propagation path loss in the equatorial conditions very differently, or the model for the buildings of a city may not be useful for another urban area. Also as can be seen the previous part, the terrain profile has also be defined for each propagation medium.

Although, GTD is the most powerful tool in order to estimate the path loss; due to the reasons given above, some engineers started to face some practical methods. These methods are generally based on empirical data. The formulation of the measured data provides to estimate the propagation path loss for different input parameters.

One of the common methods, based on measured data, is Longley-Rice model. Besides Longley-Rice model is based on measured data, it also uses the electromagnetic wave theory [27]. The Longley-Rice model described by A. G Longley and P. L. Rice in a technical report, given in [26], under the control of U.S Department of Commerce, Environmental Science Services Administration (ESSA) in 1968. Some modification to improve the performance of the model is applied in the later years. The Longley-Rice model is also known as ITS model since the authors worked with the Institute for Telecommunication Sciences (ITS).

The Longley-Rice model can be applied a very wide frequency spectrum, from 20 MHz to 20 GHz. It is based on the measurements reported by again ESSA in 1968. The measurements are given in the appendix of [26], the details of these measurements are not covered in this thesis. However, it is assumed that the measurements are provides sufficient data to proper operation of the model, except known deficiencies.

3.2.1 Input Parameters and the Details of Longley-Rice Model

First of all, the Longley-Rice model requires the terrain profile data, naturally. The interface programs based on Longley-Rice model, like Radio Mobile, can obtain the elevation data of the terrain from the open web sources. Since 90's, SRTM and DTED elevation data of the all over the world are sharing by the relevant intuitions. Nowadays, it is available 1-arc second SRTM for US and 3 arc-second SRTM for the remaining of the world. Actually, the Longley-Rice model is not strictly dependent on the terrain data, unlike GTD. A good approximation of data is

sufficient for the Longley-Rice model. The other input parameters and range are given in Table 3-1.

Table 3-1 The Longley-Rice model parameters (from [27])

The Longley-Rice model parameters and ranges	
<i>Parameter</i>	<i>Range</i>
Frequency	20 MHz to 20 GHz
Antenna Heights	0.5 m to 3000 m
Path Distance	1 m to 2000 km
Surface refractivity	250 to 400
Polarization	Vertical / Horizontal
Climate Conditions	Modeled up to 7
Reliability Level	0.1% to 99.9%

The terrain between the transmitter and receiver is defined by a 2-D plane in the Longley-Rice model. Therefore, reflections from the other obstructions which are not located in the same plane are not taken into account. After defining the terrain, the model decides propagation mode between the transmitter and receiver by using the antenna heights and obstruction heights. There are three different path loss calculation zones is the Longley-Rice model.

First one is the *line-of-sight* propagation mode. In this mode, transmitter and receiver directly “see” each other. In this mode, propagation path loss is assumed to be the free-space loss. However, if the terrain profile between receiver and transmitter satisfies the specular reflection conditions, also reflected field should be taken into account, besides direct field. ITS model takes into account the reflected field if the path length difference between direct and reflected waves is smaller than $\lambda / 4$ [25]. If the reflection exists, the reflection coefficient which is a function of ground electrical parameters and terrain irregularities is calculated by the ITS model.

Second propagation mode is the *diffraction* mode. In this mode, as expected, the receiver is located over the incident shadow boundary. In the transition region from

the *line-of-sight* mode to *diffraction* mode, the weighting functions are used to satisfy the field continuity. The algorithm of diffraction region is given in [27], which are based on measurement data. In the diffraction region, knife-edge diffraction mechanisms are used. If necessary, double knife-edge diffraction is also used. However, diffraction by more than two edges is neglected by ITS model.

If the receiver is located lower than a predetermined height, the last region called as *scattering* mode. Again the algorithm is not covered here, the details can be found in [27]. Weighting functions are used to satisfy the field continuity between *diffraction* and *scattering* modes.

The Longley-Rice model provides both area coverage and point-to-point path loss estimation. Actually, area coverage is the simply moving a mobile receiver all around the coverage area and then coloring the map according the strength of the received signal power.

Another important feature of ITS model is that it offers alternatives about reliability percentages in terms of time, locations and situations. Therefore, according to the deserved performance of the designed network, these margins are adjustable. Thus, it is able to remain in the safe side at propagation problems by using higher percentages. ITS model determines the additional losses by using the results of the lots of measured data. Therefore, they are assumed reliable and sufficient.

The detailed formulations and performance optimization of the Longley-Rice method is not the aim of this thesis. The results of ITS model are used to compare the GTD results. And tolerate the deficiencies of GTD by using the Longley-Rice method, if necessary. However, for the sake of completeness, the propagation loss estimation of the Longley-Rice model is briefly analyzed. The relationship between the propagation path loss and system parameter like h_{Rx} , d_{Rx} and h_{obs} will be investigated.

3.2.2 Propagation Path Loss Calculations of the Longley-Rice Model

The terrain profile data required to Longley-Rice model is created by using the code developed in MATLAB[®] and XVI32 hex editor. Hex editor is useful because digital elevation data is in the form of 16-bit signed integer. The created elevation data file is embedded to the interface program based on Longley-Rice model. The elevation data file type as known as SRTM (*Shuttle Radar Topography Mission*). In real life applications the SRTM files are available free, with low resolutions. In this thesis, pseudo SRTM files are created with maximum resolution, 1 arc-second. 1 second corresponds to approximately 30m around equator.

In this thesis, *Radio Mobile*[®] is used as the interface program to simulate the Longley-Rice ITS model. However, different programs can also be used, such as “*Pathloss 5*[®]” or “*SPLAT!*[®]”. The simulation interface is given in Figure 3-37.

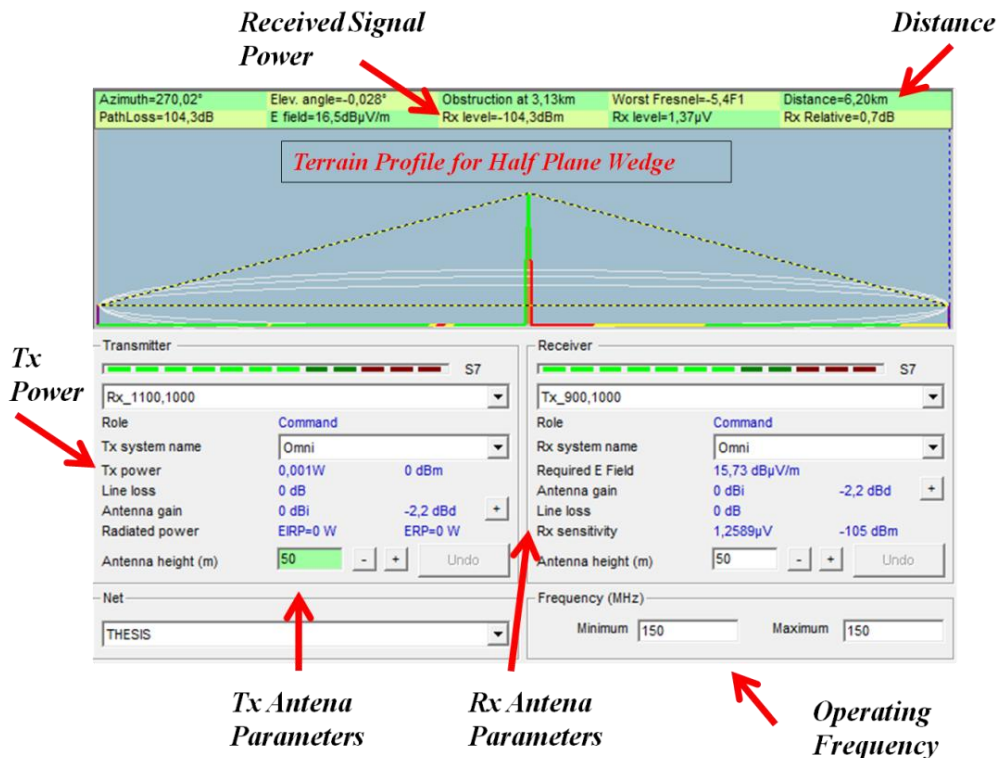


Figure 3-37 Interface of the Longley-Rice based propagation modelling program

The transmitter power is selected as 0 dBm in order to make the received signal (dBm) to the path loss (dB) equal in scalar sense. Similar to GTD, the effect of the propagation parameters h_{Rx} , d_{Rx} and h is examined in the Longley-Rice model. However, different than GTD, the parameters are in terms of meter instead of wavelength.

First, the obstruction height effect on obstruction loss is discussed for the configuration given in Figure 3-37. While the heights of the transmitter and receiver antennas are fixed to 50m and the distance between the transmitter and receiver is 6200m, the obstruction loss is given in Figure 3-38 for $f=150\text{ MHz}$ for vertical polarization. As expected, there is a direct proportionality between them.

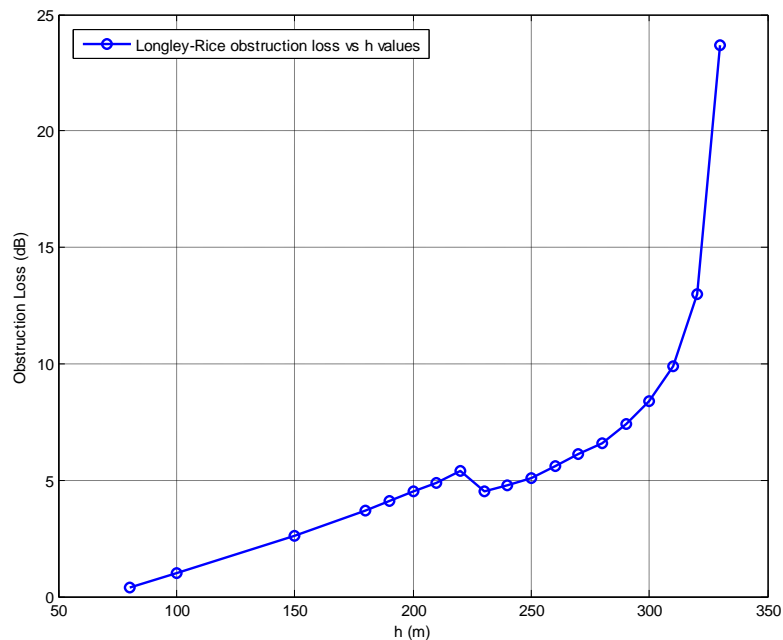


Figure 3-38 Obstruction loss vs. obstruction height (h) for Figure 3-37

The relationship between the receiver antenna distance and obstruction loss is given in Figure 3-39. Receiver antenna distance, d_{Rx} , corresponds to distance between the receiver and the obstruction, not the transmitter. Therefore, as can be seen from Figure 3-39, when d_{Rx} decreases, the obstruction loss increases since receiver is

very close to obstruction. When d_{Rx} increases, the obstruction loss decreases because the receiver avoids the “shadowing effect” of the obstruction.

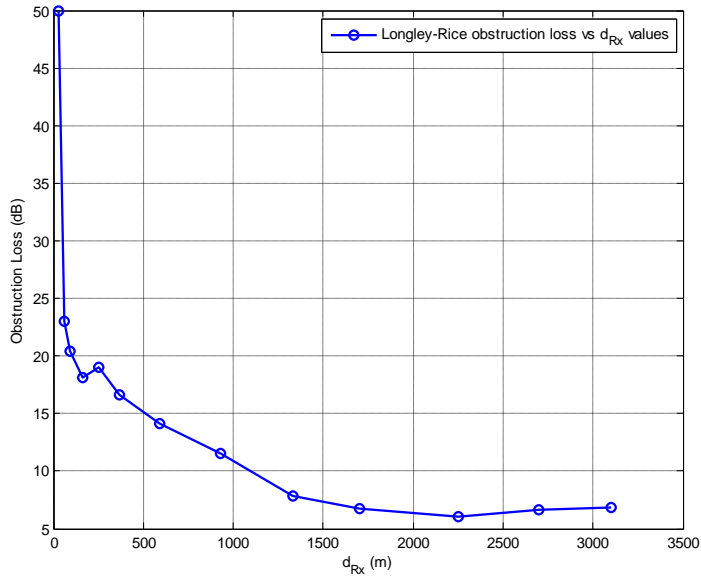


Figure 3-39 Obstruction loss vs. receiver antenna distance for Figure 3-37

The last parameter is receiver antenna height, h_{Rx} . Again it is expected that loss and receiver antenna height is inversely proportional to each other as it can be seen in Figure 3-40.

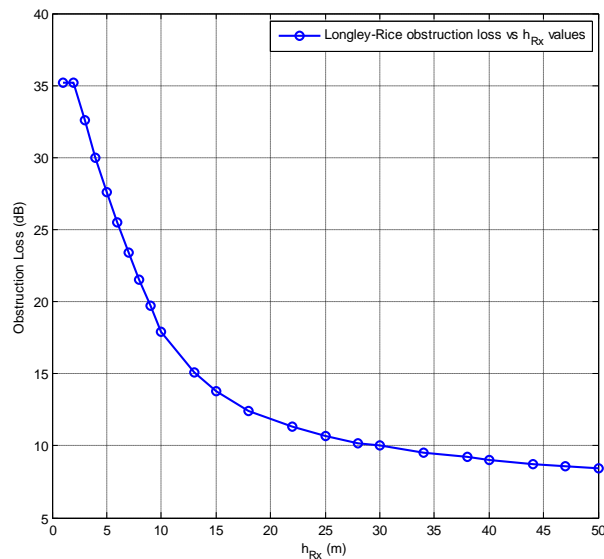


Figure 3-40 Obstruction loss vs. receiver antenna height for Figure 3-37

It is shown that GTD and Longley-Rice model gives the similar responses to the similar variations in propagation parameters. However, especially for small distances, even the parameter variations have the similar effect on obstruction loss; there are magnitude differences. Therefore, comparing the GTD and Longley-Rice Model by the real-life measurements is necessary in order to find out the weak and strong aspects of these methods. As mentioned before, this thesis does not focused on the Longley-Rice Model optimization. The Longley-Rice Model is useful for evaluation of GTD by comparing two approaches. Thus, following Longley-Rice model results may be improvable by using some other tools or parameters.

3.3 COMPARISON OF MEASURED DATA AND RESULTS OF MODELS

In the previous parts, the results of GTD and the Longley-Rice models are given. Both GTD and the Longley-Rice method gives similar responses to the parameter variations. However, still, it is necessary to refer another data source in order to comment about the differences of two approaches.

The measured data in this thesis is obtained from [29], by McQuate, Harman and Barsis, which provides data about spot measurement at the environment of Colorado plains at [29]. They are called phase-2 measurements since phase-1 was obtained in 1967.

In this thesis, two of the terrain profiles are digitalized in order to compare GTD and the Longley-Rice ITS models with each other. One of the selected terrain profiles is within the line-of-sight and the other one is beyond the line-of-sight. Therefore, it is possible to evaluate both cases. Since the real terrain profile cannot be exactly modeled, piecewise linearization is used. Again the elevation data is converted to a hex file to represent the elevation data by 16-bit signed integer SRTM “.hgt” file. This is done by using the code developed in MATLAB[®] and XVI32 hex editor. It should be noted that there are some rounding errors due to the fact that SRTM includes only integers and some linearization errors.

3.3.1 Profile R1-0.5-T1 (Planar, Line-of-Sight Sloping Terrain)

The elevation data for terrain profile at [29] is given in Table 3-2. It is observed that it is a short range profile, 550m, and the maximum elevation difference throughout the path is around 20m.

Table 3-2 The original identification of R1-0.5-T1 made by McQuate (from [29])

O'5R1T1.PFL	LAT	LON
TX CNTRY US	40.0944	254.8811
RX CNTRY US	40.0939	254.8745
DATE PROFILE TAKEN:		1967
SOURCE MAP- SCALE: 1:		24000
SOURCE DTBS-RES.(km):		
First Point TX or RX: R		
Tot. Path Length(km):		.55
Number of Points:		7

-Distance-	Gnd Hgt	Coverage
fm first pt a.m.s.l.	Code	
(km)	(m)	(0-99)

.00	1589.	
.10	1585.	
.19	1582.	
.27	1579.	
.39	1576.	
.45	1573.	
.55	1570.	

For profile R1-0.5-T1, simple linearization by using the first and last datum is sufficient. It can be seen from Figure 3-41, the exact and linear form of elevation data are match. Besides its simplicity, profile R1-0.5-T1 has another advantage due to the fact that there is no edge in the terrain. Therefore, GTD reduces to GO for this case. Otherwise, both GO and diffraction mechanisms play role the propagation path loss and it would be difficult to decide whether the error occurs due to the GO part or diffraction part. After determining the error due to GO, it would be possible

to apply this error to other case in order to find out the error due to the only by the diffraction mechanism.

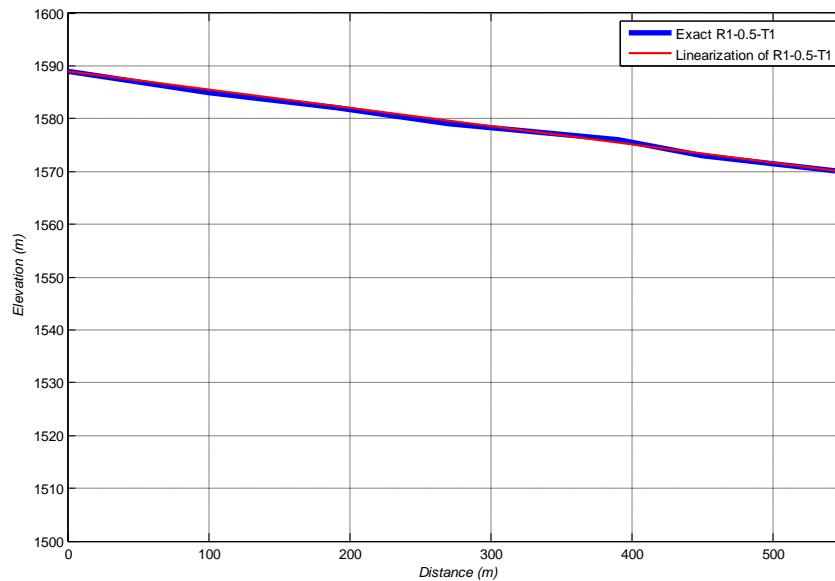


Figure 3-41 Exact and linear elevation data for profile R1-0.5-T1

The transmitter is located at 550m and receiver at 0 m according to the distance axis given in Figure 3-41. At [29], measurements are made at 7 different frequencies: 230 MHz, 410 MHz, 751 MHz, 910 MHz, 1846 MHz, 4595 MHz and 9190 MHz. At [29], the only difference between different frequencies, for profile R1-0.5-T1, is the transmitter antenna height [29]. Transmitter antenna height is 6.6m for 751 MHz and below, 7.3m for 910 MHz and above. It is not necessary to analyze all 7 frequencies in a detailed way; therefore, two of them are selected. In order to obtain low and high frequency characteristics, 230 MHz and 1846 MHz are chosen.

3.3.1.1 Operating Frequency 230 MHz, Terrain Profile R1-0.5-T1

For this case, since the simulation interface program based on Longley-Rice Model requires the conductivity and relative permittivity. Conductivity is selected as 0.005 S/m and relative permittivity is selected as 15.0 which are average ground electrical constants. Also local surface roughness, clutter effects, is not taken into account for both GTD and Longley-Rice models.

The measured data obtained from [29], is plotted in Figure 3-42. Since, in [29], the data are measured when the Rx antenna height starts with 1 goes to 13, GTD and Longley-Rice model calculations are made similarly. Rx antenna height starts with 1m, increases to 13m with 0.5m intervals; so, there are 25 points in the graph.

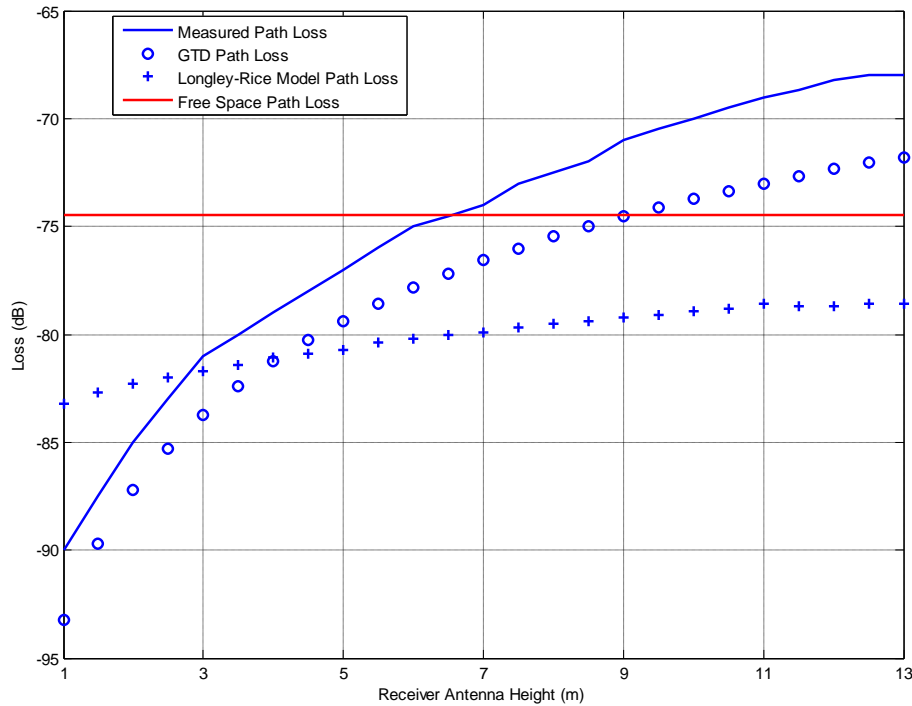


Figure 3-42 Path losses vs. receiver antenna height at 230 MHz for R1-0.5-T1

The horizontal polarization is used for the Longley-Rice model. It can be observed from Figure 3-42, that there is a good agreement between GTD and measured data. The maximum error is around 2 dB. Longley-Rice model path loss again predicts the measured path loss with around 3 dB average error. This is also acceptable but it is clear that GTD is much more inconsistent with the measured data.

In general, the differences between the measured data and the data obtained from models are acceptable. From the point of view of GTD, local roughness and also finite conductivity are not taken into account; therefore, the difference is acceptable. From the point of view of Longley-Rice model, again local roughness effect (clutter effect) is not taken into account and its calculation method is almost entirely

empirical; therefore, the error versus speed trade off is quite acceptable also for Longley-Rice model. Indeed, there are lots of parameters which are impossible to take into account in the empirical models, such as reflection from other sources or unwanted signal source that creates with the interference with the desired signal.

3.3.1.2 Operating Frequency 1846 MHz, Terrain Profile R1-0.5-T1

Again for this case, conductivity is 0.005 S/m and relative permittivity is 15.0 and polarization is horizontal for the Longley-Rice Model. However, for 1846 MHz, transmitter antenna is 7.3 instead of 6.6.

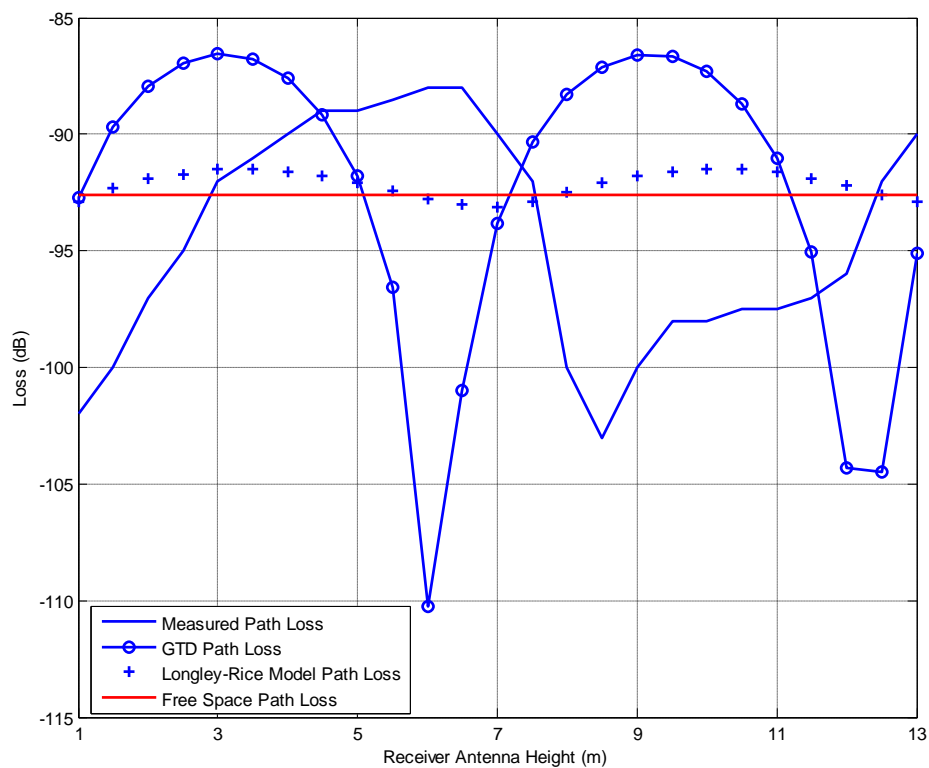


Figure 3-43 Path losses vs. receiver antenna height at 1846 MHz for R1-0.5-T1

It is clear that Longley-Rice model fails to predict the path loss. The reason is that Longley-Rice model does not take into account the reflected waves [25]. Therefore, it gives simply free space loss. The Longley-Rice method calculates the reflected field if the path length difference between the direct and reflected rays is smaller

than one-quarter wavelength. At 1846 MHz, the wavelength is 16 cm and one-quarter wavelength is 4 cm. It is exceeded by all the receiver antenna heights in this case.

In Figure 3-43, the GTD path loss values are calculated correctly; however, there is a “delay” between the measured data and the calculated one. According to [25], this “delay” is due to the terrain surface roughness which may also be called as clutter effect. Trees, stones and plants at the terrain cause such an effect. Therefore, GTD results are modified by multiplying reflection coefficient with a roughness factor; however, this is another concept that is beyond the scope of this thesis. It should also be noted that such delay errors are correctable. Even with the roughness factor, still, there would be some differences due to the finite conductivity or environmental effects. Not the environmental effects but the finite conductivity effect can be modified in GTD. However, it is again beyond the scope of this thesis. Also it should be expected that, Longley-Rice model is more successful to modeling the environmental effects since it is based on statistical data that already cover the environmental effects.

Beyond the line-of-sight terrain profile will be discussed in the next part, after analyzing the line-of-sight profile, R1-0.5-T1, in this part.

3.3.2 Profile R1-5-T5A (Abrupt Terrain, Beyond the Line-of-Sight)

The elevation data for R1-5-T5A terrain profile at [29] is given in Table 3-3.

Table 3-3 The original identification of R1-5-T5A made by McQuate (from [29])

005R1A5.PFL	LAT	LON	-----	.69	1591.	3.57	1551.
TX CNTRY US	40.1036	254.8167	-Distance- Gnd Hgt Coverage	.92	1591.	4.20	1554.
RX CNTRY US	40.0939	254.8745	fm first pt a.m.s.l. Code	1.34	1597.	4.96	1558.
DATE PROFILE TAKEN:	1967		(km) (m) (0-99)	1.61	1597.	5.04	1558.
SOURCE MAP- SCALE: 1:	24000		-----	2.04	1579.		
SOURCE DTBS-RES.(km):			.00 1589.	2.14	1582.		
First Point TX or RX: R			.23 1591.	2.22	1582.		
Tot. Path Length(km):	5.04		.43 1591.	3.25	1545.		
Number of Points:	17		.55 1588.	3.36	1545.		

It is seen that R1-5-T5A is a longer than R1-0.5-T1, it is 5040 m and the maximum elevation difference throughout the path is around 30m. The exact terrain profile data of R1-5-T5A given in [29] and its piecewise-linear version is given in Figure 3-44. Since there exists lots of roughness at the terrain, it is not possible to linearize by the start and end points of the plot; therefore, piecewise linearization is preferred.

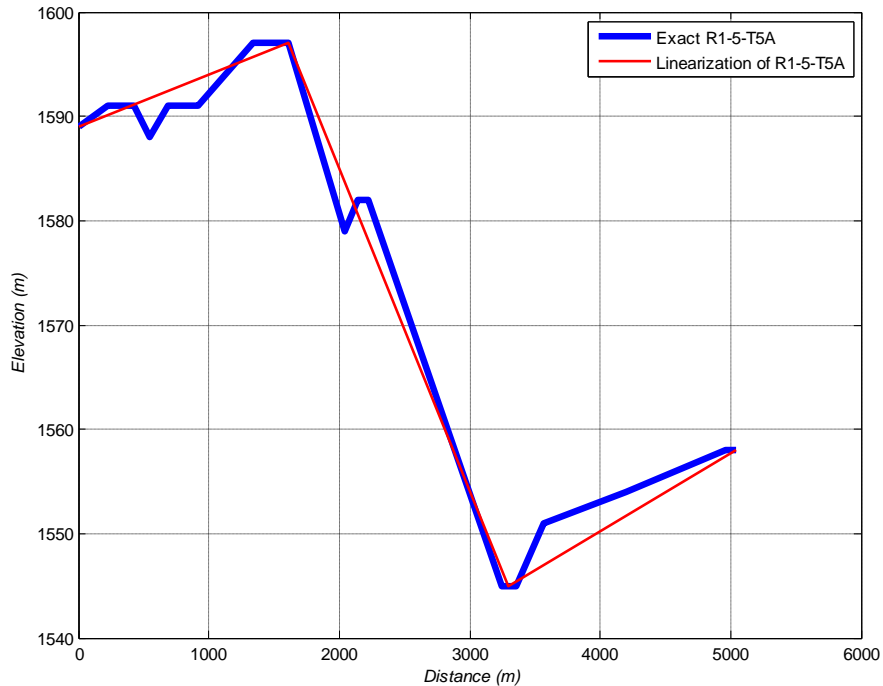


Figure 3-44 The exact R1-5-T5A terrain profile and linearization of terrain

The transmitter is located at 5040 m distance and 1558m height. The receiver is at 0 m distance and basically located at 1589m elevation. In order to find diffracted fields by GTD, it is necessary to find diffraction coefficient. Again since the measurements are taken in [29], when height of the receiver antenna starts 1m and goes to 13m with 0.5m intervals, GTD and Longley-Rice calculations use the same method. In order to find source and observation angle and distance, the linear version of R1-5-T5A given in Figure 3-44 is located a coordinate system, which is given in Figure 3-45 .

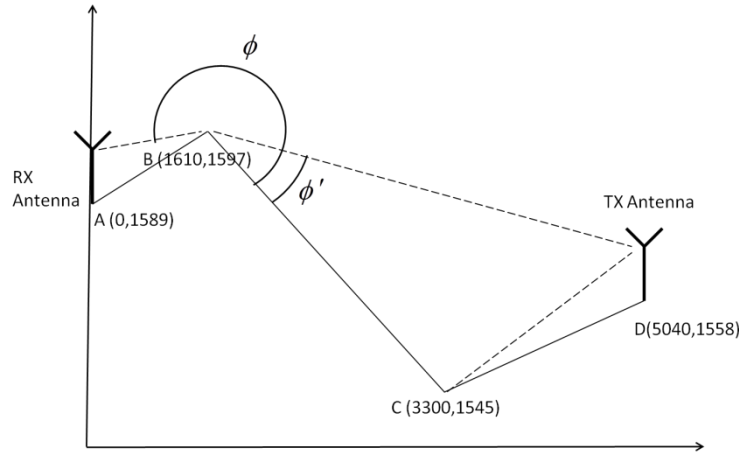


Figure 3-45 Coordinate system and coordinates of linear terrain

At [29], measurements are made at 7 different frequencies: 230 MHz, 410 MHz, 751 MHz, 910 MHz, 1846 MHz, 4595 MHz and 9190 MHz. The only difference between different frequencies, for profile R1-5-T5A, is the transmitter antenna height. Transmitter antenna height is 6.6m for 751 MHz and below, 7.3m for 910 MHz and above. In order to obtain low and high frequency characteristics, 230 MHz and 4595 MHz are selected.

Also profile R1-5-T5A, converted to digital elevation SRTM file using the code developed in MATLAB[®] and XVI32 hex editor. In Figure 3-46, it can be seen that the antenna locations and the embedded elevation data at the interface of the Radio Mobile program, based on the Longley-Rice model. It is clear that the embedded elevation data is almost same with the linear version of the terrain profile R1-5-T5A. Figure 3-46 is given for the operating frequency is 230 MHz, but elevation data valid also for 4595 MHz since terrain profile does not change with frequency.

3.3.2.1 Operating Frequency 230 MHz, Terrain Profile R1-5-T5A

For this case conductivity and relative permittivity are 15.0 and 0.005 S/m, respectively, as in the previous case. Also local surface roughness and clutter effects are not taken into account for both GTD and Longley-Rice models.



Figure 3-46 Embedded terrain profile R1-5-T5A at the interface of the program

The measured data obtained from [29], is plotted in Figure 3-47. Again there are 25 points for GTD and Longley-Rice models in the graph; since Rx antenna height starts with 1m, increases to 13m with 0.5m intervals.

It is clear that, similar to the previous path, in Figure 3-47, GTD estimates the path loss closer to the measured values than the Longley-Rice method. According to the [29], R1-5-T5A is very rough surface. Therefore, the difference between the estimated path loss by GTD and measured path loss may be result of the rough surface, because GTD method described in this thesis does not take into account the clutter effect. As mentioned before, clutter effect may be added to the GTD by modifying the reflection coefficient by a roughness factor; however, that is beyond the scope of this thesis. In a similar way, clutter sources at the terrain may be responsible for the difference between the estimated and measured path loss in Longley-Rice method. To solve this problem, clutter data available at the market may be added the results of such simulation programs.

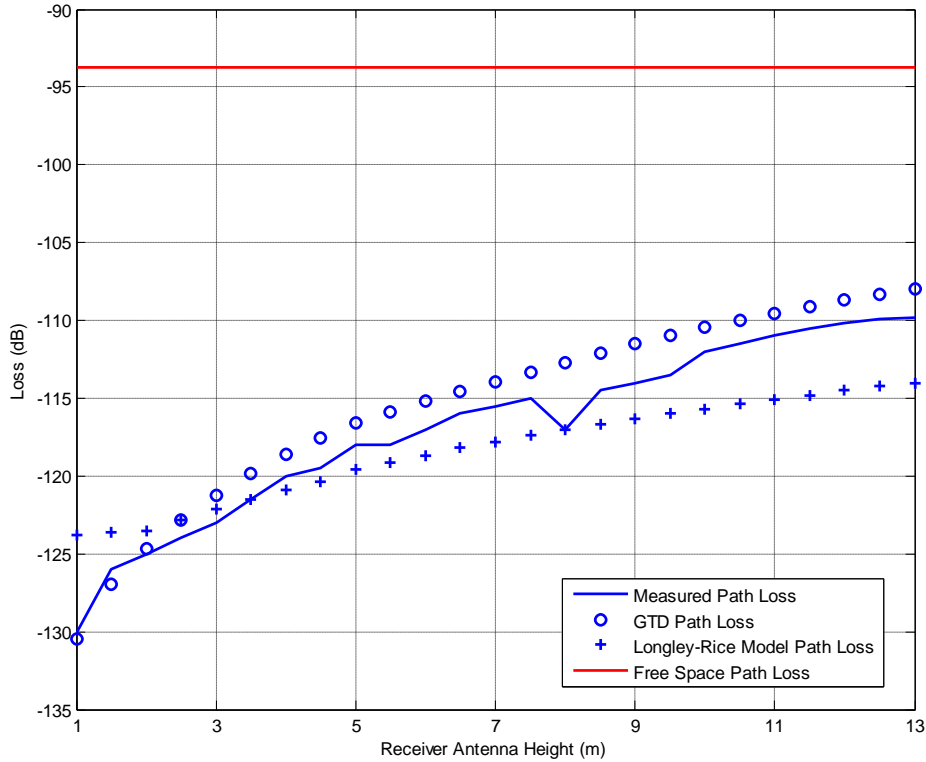


Figure 3-47 Path losses vs. receiver antenna height at 230 MHz for R1-5-T5A

3.3.2.2 Operating Frequency 4595 MHz, Terrain Profile R1-5-T5A

Polarization, conductivity and relative permittivity are selected as the same with the previous ones. The measured data obtained from [29], the estimated path losses by GTD and Longley-Rice Model are plotted in Figure 3-48. As expected, it is similar to the Figure 3-47. Still GTD estimates the propagation path loss better than Longley-Rice method; however, the error in GTD estimation increases from 2 dB to 7 dB approximately with the frequency increasing. Increasing in the error may be the result of the surface roughness, not taken into account in this thesis. Because when the frequency is increased, wavelength is decreased and the fixed size roughness parameters become bigger than due to the operating wavelength decreasing. Therefore, negligible roughness in the previous case now may have a noticeable effect on the path loss. Therefore, it may be concluded that roughness factor should be taken to account at GHz propagations in GTD applications.

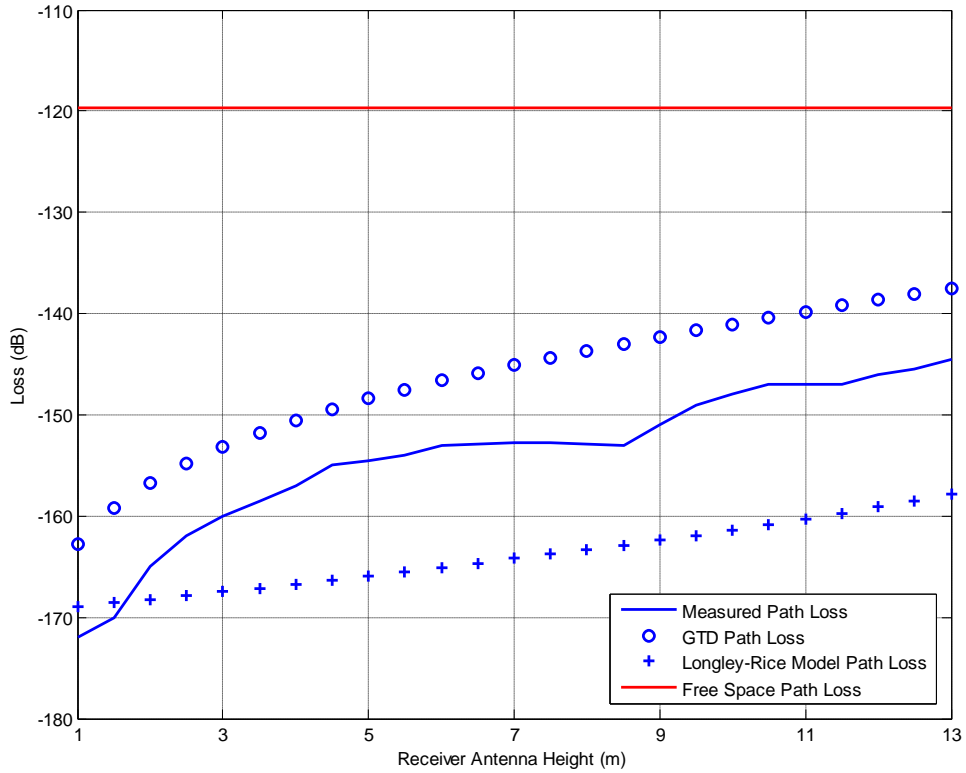


Figure 3-48 Path losses vs. receiver antenna height at 4595 MHz for R1-5-T5A

To sum up, GTD estimates the path loss better than the Longley-Rice method for the short terrain profiles analyzed up to now in this thesis. However, long terrain profiles, it may be expected that Longley-Rice gives more accurate results than GTD. Because GTD does not take into account Tropospheric effects; however, as mentioned before one of the input parameters of the Longley-Rice model is surface refractivity; therefore, it calculates the effective earth radius and Tropospheric scattering.

Another important result obtained in this chapter is that the error between measured data and GTD estimated path loss is increasing with the frequency. This is an expected result by taking into the consideration the terrain profile surface roughness. Modeling the clutter effect on path loss requires an in-depth study which is not the aim of this thesis. However, it should be noted that, at low frequencies since the wavelength is large, lots of the surface roughness are negligible. While

increasing the frequency, even the small objects become electrically very large according to small operating wavelength. Therefore, roughness correction should be applied to the GO reflection coefficient especially at GHz propagation. For the Longley-Rice model based simulation programs, clutter data that defines effect of clutter on path loss is available at the market.

Also it is shown that, when the surface roughness has no series influence on path loss, there is a good match between GTD results and measured data. This indicates that the average ground electrical parameters like conductivity and permittivity are sufficient to modeling the ground by GTD as PEC.

Multiple diffraction mechanisms of GTD are not included in this thesis.

Finally, although the performance of GTD is better than the performance of the Longley-Rice model for terrain profiles analyzed here, Longley-Rice model may give accurate results than GTD by some modification and improvements. In other words, comparison made in this chapter is not final analysis since Longley-Rice improvements may be applicable. Longley-Rice method is utilized in this thesis just to test the performance of GTD by comparing with it.

CHAPTER 4

OPTIMIZATION OF AN ANTENNA SYSTEM LOCATED ON A HILLY TERRAIN IN TERMS OF RECEIVER SIDE

In this chapter, by using the results obtained in previous chapters, as a case study, including optimization of an antenna system located on hilly terrain is performed by selecting the proper receiver parameter, we mainly focused on receiver side, because in real life applications transmitters serve more than for one user, for example a GSM site may transmits signal thousands of user mobile phone at the same time, or a television system similarly provides services may be hundreds of thousands of people at the same time. Therefore, in real life experiences, it may not be possible the parameter optimization of a transmitter because there are lots of receivers. Therefore, in this chapter, receiver parameter optimization is carried out for such a system given in Figure 4-1.

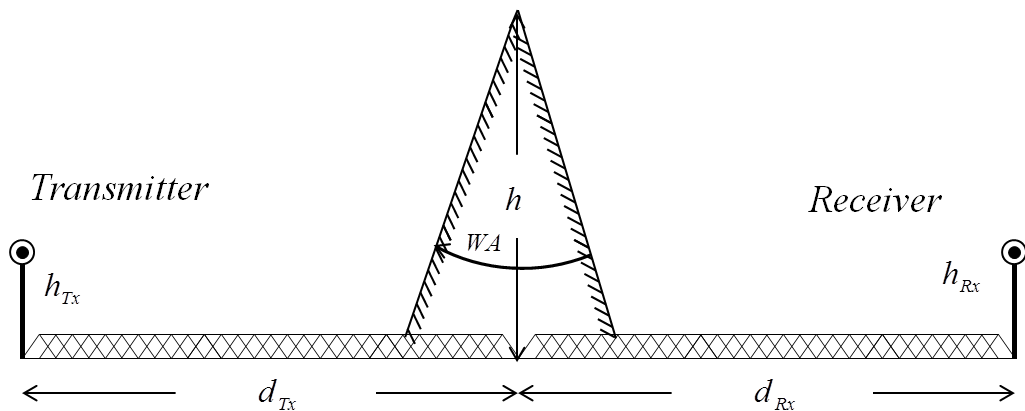


Figure 4-1 A simple antenna system where the receiver in diffraction region

Some of the important parameters which are given in Figure 4-1 or not given can be listed as,

- Polarization (vertical or horizontal),
- Minimum and maximum operating frequency,
- Transmitter antenna height, antenna type and antenna gain,
- Receiver antenna height, antenna type and antenna gain,
- Input power to the transmitted antenna after cable losses,
- Transmitter and receiver polarizations,
- Height and location of the obstruction,
- Angle of the wedge that represents the obstruction,
- The distance between the obstruction and transmitter and receiver ,
- System topology (voice, data),
- System reliability parameter in terms of time, location and situation.

Some other parameters may be added to the list given above, such as climate conditions.

First, the polarization effect will be discussed. However, it should be noted that the polarization term in this chapter refers another phenomena according to the previous chapter. In previous chapter, the polarization is called as *soft* or *hard* and it corresponds to whether wave is radiated from an electric or magnetic line source, respectively. However, in this chapter polarization may be *horizontal* or *vertical* and it is determined according to the position of the antenna.

GTD is derived from the structure that includes a wedge and a line source which is parallel to edges of wedge. That corresponds to the *horizontal* polarization. This is shown in Figure 4-2. In order to compare the same polarizations; in this thesis, the *horizontal* polarization is used in the Longley-Rice model.

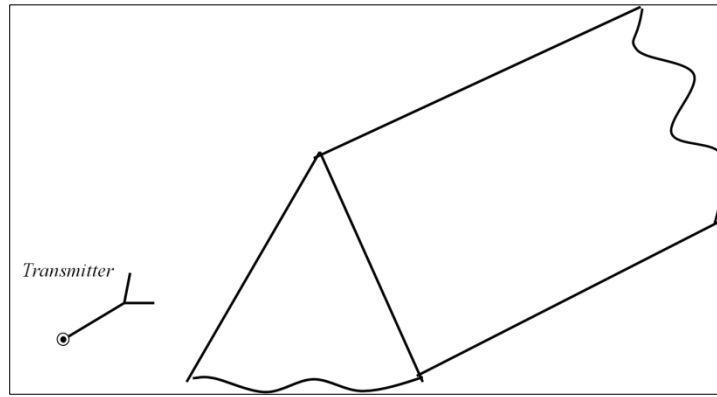


Figure 4-2 Representation of parallel polarization of an antenna and 3-D hill

In real life applications, it is important that selecting all the polarizations same since cross polarization losses are important. If there is no way to know the receiver polarization, transmitter polarization should be selected as circular.

The second parameter is minimum and maximum operating frequency. Since there are more than one transmitter channels in a transmitter site and they share the same antenna system, optimization should take into account all of them. Generally, the frequency can be selected as the arithmetic average of the operating frequencies. GTD is a high frequency technique; therefore, the frequency does not change the diffraction losses. However, free space loss depends on frequency also the phase difference between direct and reflected waves are important for the GO part. Therefore, overall GTD results are dependent to the frequency.

As can be seen from Figure 3-47 and Figure 3-48, if the frequency is larger than 1 GHz the surface roughness has an important effect on GTD results. Therefore, if the terrain has lots of roughness that cause clutter effect, operating frequency should be selected below 1 GHz in order to guarantee the GTD estimation about path loss.

The third item in the list is transmitter antenna height, type and gain. However, the optimization of transmitter site is not discussed in this thesis. Since in real life applications, one transmitter serves lots of users at the same time; therefore, it is not

possible to determine a reference receiver in order to make optimization, as discussed before.

Next one is the receiver antenna height, type and gain. The antenna type should be selected in accordance with the desired performance and physical constraints. Gain should be selected high as possible as; however, if the gain of a practical antenna is high, the antenna pattern will be narrower. Therefore, gain should be selected high but at the same time pattern should includes the desired angles. Receiver antenna height effect on obstruction loss for half-plane wedge is given in Figure 3-19 and in Figure 3-20. If the wedge angle is not zero, antenna height vs. obstruction loss plots given in Figure 3-30, Figure 3-31 and Figure 3-32 . It is not necessary to give these plots here again, since it is clear that higher receiver antenna as much as possible is desirable to make the obstruction loss smaller, as expected.

Not only the calculated GTD results but also measured data show that higher receiver antenna height should be preferred. According to the measurement given in Figure 3-42 for R1-0.5-T1 and the measurements given in Figure 3-47 and Figure 3-48 for R1-5-T5A indicate that there is an inverse proportionality between the receiver antenna height and obstruction loss. The only exception is measurements given in Figure 3-43 for the line of sight terrain profile R1-0.5-T1. Since it provides some important results, it is given in Figure 4-3 again, without free space loss plot.

As can be seen from Figure 4-3, when there is line-of-sight between the transmitter and receiver, the Longley-Rice model generally does not takes into account the reflected waves for high frequencies. Because quarter-wavelength path difference between direct and reflected waves is exceeded for high frequencies. If it is exceeded, the Longley-Rice model does not take into account the reflection mechanism. Therefore, the model provided by GTD should be reliable.

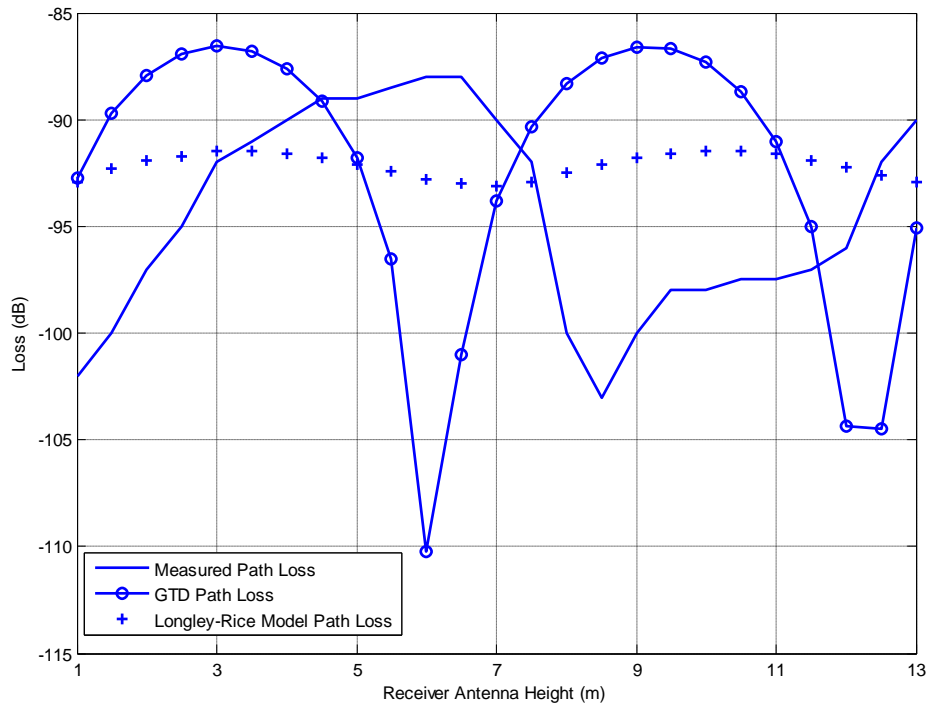


Figure 4-3 Path losses vs. receiver antenna height at 1846 MHz for R1-0.5-T1

The “delay” between the measured and GTD results are discussed before, it is due to the surface roughness; not the antenna height. However, at some intervals, although the height of the receiver antenna increases the path loss does not decrease. Because, the terrain profile does not include any diffraction edge, the diffraction mechanism of GTD does not exist; therefore, there are only GO fields. The phase difference between the direct and reflected waves are important in GO, as discussed before. There, due to the out of phase direct and reflected waves the received power may be decreases. Therefore, if the frequency is high and there is line of sight between receiver and transmitter, antenna height should be selected by taking into account the GO field effects.

The last parameter in the list should be discussed is the distance between the obstruction and receiver antenna. The other items in the list are fixed or unchangeable. For example, height and location of a mountain cannot be changed. Similarly the wideness of the mountain cannot be changed so wedge angle is fixed.

When $h_{Tx} = h_{Rx} = 25\lambda$, $h = 50\lambda$ and $d_{Tx} = 1000\lambda$, the obstruction loss vs. the distance between the obstruction and receiver antenna, are given in Figure 4-4. It can be seen that there is a sharp decrease near the obstruction and when d_{Rx} increases loss still decreases but smoothly. Another important point is that the obstruction loss given in Figure 4-4 is the loss over free space. Since the free-space loss does not increase so rapidly after the obstruction, due to the distance between the transmitter and obstruction; it is possible to make an optimization about the distance between the obstruction and receiver antenna.

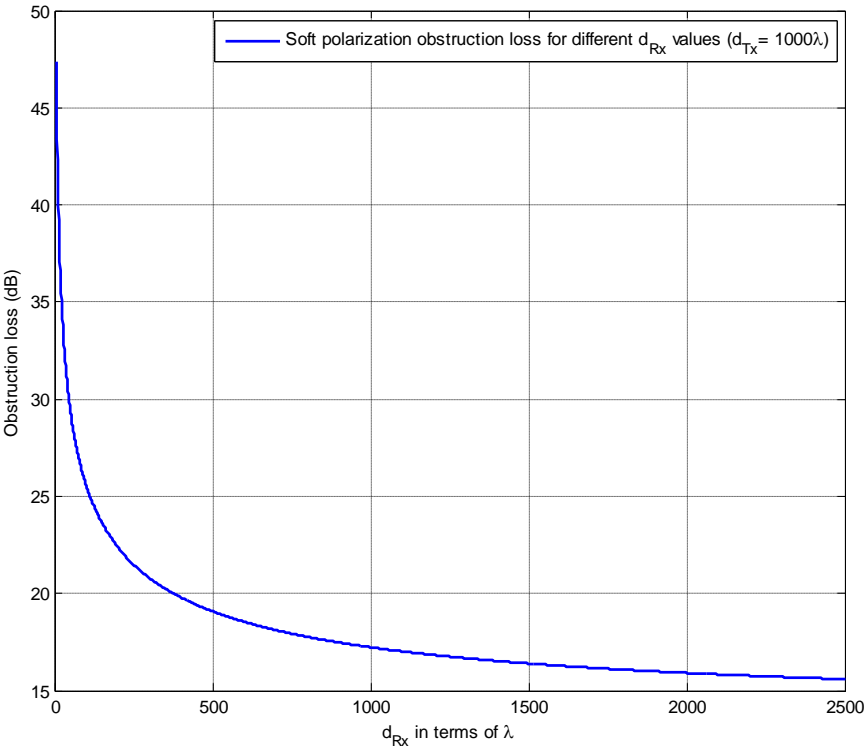


Figure 4-4 Loss vs. d_{Rx} when $h_{Tx} = h_{Rx} = 25\lambda$, $h = 50\lambda$ and $d_{Tx} = 1000\lambda$

When $h_{Tx} = h_{Rx} = 25\lambda$, $h = 50\lambda$ and $d_{Tx} = 1000\lambda$, the total loss is given in Figure 4-5. It can be seen that maximum field obtained at the distance 500λ after the obstruction. When all other parameters are same but d_{Tx} is decreased to 500λ and increased to 1000λ , the total losses are given in Figure 4-6 and Figure 4-7.

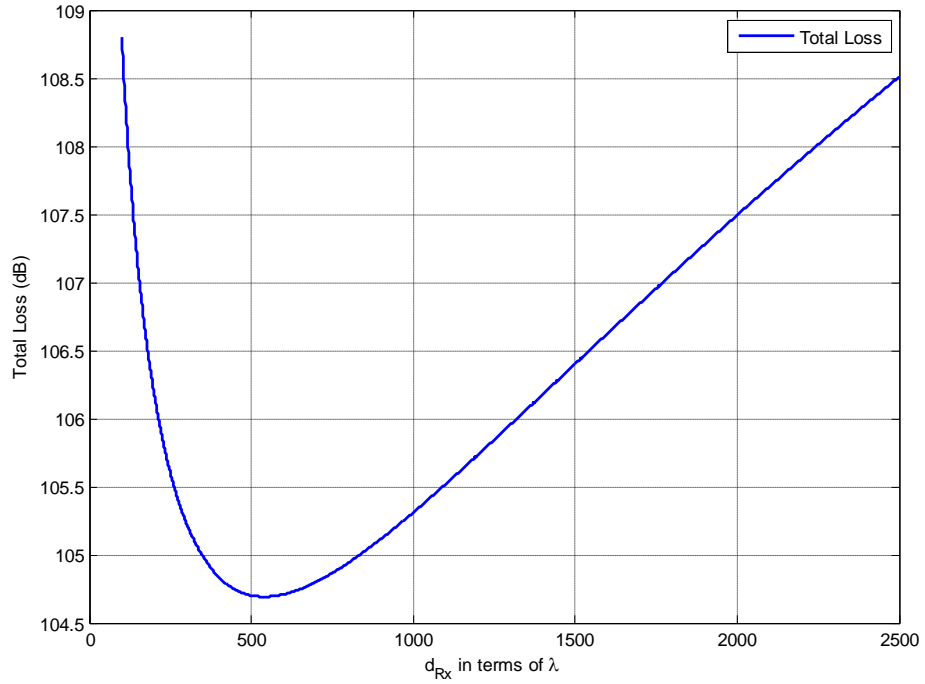


Figure 4-5 Total loss vs. d_{Rx} for $h_{Tx} = h_{Rx} = 25\lambda$, $h = 50\lambda$ and $d_{Tx} = 1000\lambda$

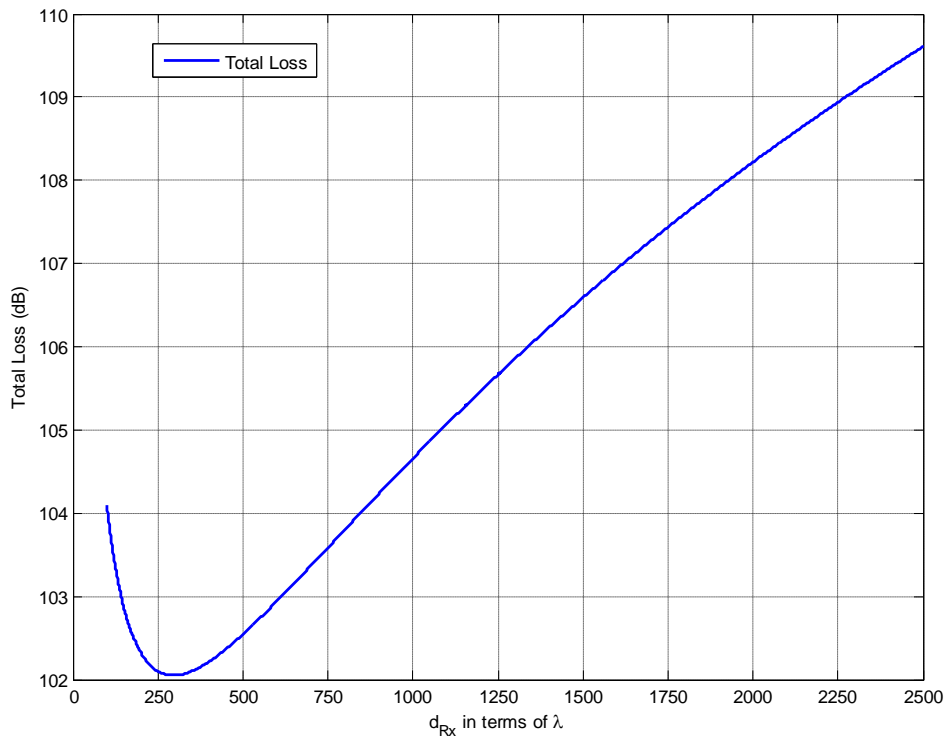


Figure 4-6 Total path loss vs. d_{Rx} for $h_{Tx} = h_{Rx} = 25\lambda$, $h = 50\lambda$ and $d_{Tx} = 500\lambda$

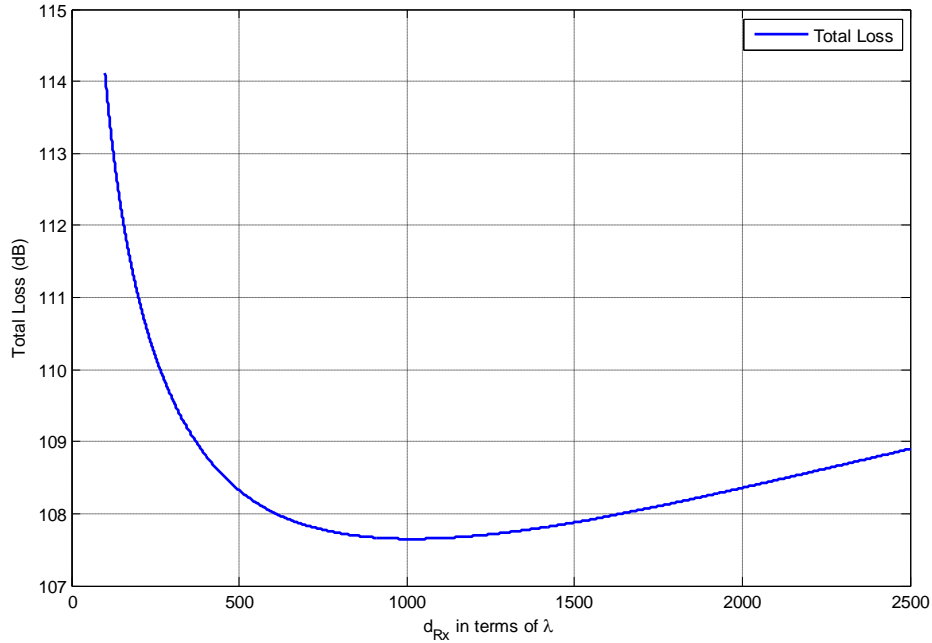


Figure 4-7 Total path loss vs. d_{Rx} for $h_{Tx} = h_{Rx} = 25\lambda$, $h = 50\lambda$ and $d_{Tx} = 2000\lambda$

From Figure 4-5, Figure 4-6 and Figure 4-7, it can be concluded that the maximum received field can be achieved after the obstruction with a distance, *half of the distance between the transmitter and obstruction*, $\frac{d_{Tx}}{2}$.

To sum up, in this chapter, the parameters are described for an antenna system located on a hilly terrain. After discussing the general constraints about the parameters, the study focused on the receiver site. The other parameters are assumed constant or configurable according to the receiver.

Two important parameters about the receiver side are receiver antenna height and location.

About the first parameter, antenna height, it is shown that, although for many practical cases the higher receiver antenna corresponds to higher received field, some exceptional cases are discussed like in Figure 4-3. The reason of this exceptional case is the reflected waves in GO and explained in a detailed way in

this chapter. If there is a line-of-sight between transmitter and receiver and also the operating frequency is high, the receiver antenna height should be determined carefully due to the phase difference between the direct and reflected waves in GO. Especially, if there is no edge at the terrain, then due lack of diffracted fields, the GO fields may dominate and the effect described above would become more noticeable.

About the second parameter, antenna distance, it is shown that the receiver antenna should be located far away from the obstruction in order to avoid shadowing effect of the obstruction and reduce the obstruction path loss. However, moving away from the obstruction means moving away from the transmitter at the same time. Therefore free space path loss also increases. Therefore an optimization is offered in this thesis about d_{Tx} , d_{Rx} should be selected as $\approx \frac{d_{Tx}}{2}$ or a little smaller than it. Here d_{Tx} corresponds the distance between the obstruction and transmitter. Also, d_{Rx} corresponds the distance between the obstruction and receiver.

CHAPTER 5

CONCLUSION

Main goal of this thesis work is modeling the propagation path loss for hilly terrain by using ray optic methods. To do this, first, the field variations of various types of structures are examined by Geometrical Optics. Due to the failures of GO, diffraction mechanisms of GTD are inserted the classical GO theorem. GTD diffraction coefficients are obtained by analyzing the wedge diffraction fields when a field is incident upon the wedge. The structure is selected as wedge due to the fact that in real life, the mountains and hills can be represented by a wedge. Then a code developed in MATLAB[®] in order to apply diffraction mechanisms to the problems practically. Also the code is applied to the problems that cannot be solved by Geometrical Optics, the results proved that the code and GTD mechanisms work properly.

Then simplified models of real life propagation environments are analyzed by using GTD. To do that, the mountains located between the transmitter and receiver is represented by a wedge. And the diffraction phenomena in the real life are simulated by the coefficients obtained from the wedge diffraction. The relationship between propagation path loss and lots of propagation environment parameters are discussed. The models are analyzed for both soft and hard polarization. The discussions about GTD can be summarized as,

- Varying the transmitter and the receiver parameters has the same effect on the obstruction loss. Therefore, only the receiver side is analyzed.

- Increasing the height of the obstruction increases the obstruction path loss, as expected.
- Increasing the distance between the obstruction and receiver antenna, while all other parameters are same, decreases the obstruction path loss. Since receiver avoids the “*shadowing effect*” of the obstruction.
- Increasing the height of the receiver antenna decreases the obstruction path loss, as expected.
- While all other parameters are the same, loss is proportional to wedge angle for soft polarization and inversely proportional to hard polarization. However, the effect of wedge angle is limited to 1.5 dB, even the wedge angle varies from 0° to 90° .

Also, the Longley-Rice model is applied to same structures by using a simulation program, Radio Mobile[®], which is based on Longley-Rice method. The elevation data used by the program is modified by using a code developed in MATLAB[®] and XVI Hex editor. Therefore, it is possible to analyze any type of the structure by the program.

Then the Longley-Rice model results are compared with GTD results. It is observed that varying the same parameter has the similar effect on obstruction loss in both GTD and the Longley-Rice models. But the magnitude of the effect is different. For example, increasing the receiver antenna distance decreases the obstruction loss for both GTD and Longley-Rice model; however, the amount of decrease is different.

Measured data is used in the comparison of the GTD and Longley-Rice models as reference. To do the data measured at Colorado plains by McQuate, Harman and Barsis. Although different terrain profiles are available two of them are selected: one lie-of-sight and one beyond the line-of-sight. Line-of-sight profile, R1-0.5-T1 is analyzed by GTD and the Longley-Rice one low (230 MHz) and one high (1846 MHz) frequency. The beyond the line-of-sight profile, R1-5-T5A is analyzed by

GTD and the Longley-Rice one low (230 MHz) and one high (4595 MHz) frequency, similarly.

The results can be summarized as,

- GTD provides better estimation on propagation path loss according to the Longley-Rice model for the short range terrain profiles analyzed in this thesis.
- Although GTD always provides results with an acceptable error, the amount of the error is increasing with the frequency. For example, in R1-5-T5A terrain profile, the error increased from 2 dB to 7 dB. This is a result of the decreasing wavelength with increasing frequency. For fixed size clutter sources such as plants, stones, become more noticeable for the propagated waves when the wavelength is small. Therefore, especially, after 1 GHz GTD results should be modified by roughness factor.
- In line-of-sight propagation medium, the Longley-Rice model neglects the reflected wave and gives only free space loss for high frequencies.

In Chapter 4, by taking into account the results above, the parameters of an antenna system located on a hilly terrain is discussed. Although increasing the height of the receiver antenna generally increases the received field, there are some exceptions in line-of-sight propagation medium. The example of this exception is given in the measured and GTD data for line-of-sight profile, R1-0.5-T1 and it is emphasized that this effect should be taken into account in determining the receiver antenna height. The other changeable receiver antenna parameter in an antenna system is antenna location. As mentioned before, if the distance between the obstruction and the receiver antenna increases, obstruction loss decreases. However, in this case, receiver goes far away from the transmitter source and the free space loss increases. Therefore, an optimal distance is offered to minimize the total loss, and it

corresponds to approximately half of the distance between transmitter and obstruction ($d_{Rx} \approx \frac{d_{Tx}}{2}$).

Although throughout this thesis, GTD and Longley-Rice models are compared, it should be noted that the performance of the Longley-Rice model may be improved. However, that is not an aim of this thesis. And it would be a future work based on this thesis. In other words, a future work improves Longley-Rice model and then it may be useful than GTD. Since Longley-Rice is an empirical model, it may tolerate the clutter errors better than the GTD. One another advantage of Longley-Rice model is also useful for very long propagation distances since the earth curvature and Tropospheric effects are taken into account in Longley-Rice method. By the help of this advantages, a future work make Longley-Rice better than GTD.

Another future work may be taking into account the roughness factor and finite conductivity effects. Finite conductivity does not cause series errors; however, as mentioned before, after 1 GHz, GTD is needed to improve by roughness factor.

The performances of GTD and the Longley-Rice model are compared for only line-of-sight case and one diffraction case in this thesis. A future work similar to this thesis study may analyze the multiple diffraction performance of these two approaches.

REFERENCES

- [1] C.A. Balanis, *Advanced Engineering Electromagnetics*, Second Edition, John Wiley & Sons, New York, 2012.
- [2] J. B. Keller, "Diffraction by an aperture," *Journal of Applied Physics*, vol. 28, no. 4, pp. 426-444, April 1957.
- [3] J. B. Keller, "Geometrical theory of diffraction," *Journal of the Optical Society of America*, vol. 52, no. 2, pp. 116-130, February 1962.
- [4] R. G. Kouyoumjian, "Asymptotic high-frequency methods," *Proceedings of the IEEE*, vol. 53, pp. 864-876, August 1965. 11-36
- [5] P. H. Pathak and R. G. Kouyoumjian, "The dyadic diffraction coefficient for a perfectly conducting wedge," Technical Report 2183-4 (AFCRL-69-0546), Ohio State University ElectroScience Laboratory, June 5, 1970.
- [6] P. H. Pathak and R. G. Kouyoumjian, "An analysis of the radiation from apertures on curved surfaces by geometrical theory of diffraction," *Proceedings of the IEEE*, vol. 62, no. 11, pp. 1438-1447, November 1974.
- [7] R. G. Kouyoumjian and P. H. Pathak, "A uniform geometrical theory of diffraction for an edge in a perfectly conducting surface," *Proceedings of the IEEE*, vol. 62, no. 11, pp. 1448-1461, November 1974.
- [8] P. Y. Ufimtsev, "Method of edge waves in the physical theory of diffraction," translated by U.S Air Force Foreign Technology Division, Wright-Patterson AFB, Ohio, September 1971.
- [9] P. Y. Ufimtsev, "Approximate computation of the diffraction of plane electromagnetic waves at certain metal bodies (i and ii)," *Sov. Phys. Tech.*, vol. 27, pp. 1708-1718, August 1957.
- [10] P. Y. Ufimtsev, "Secondary diffraction of electromagnetic waves by a disk," *Sov. Phys. Tech.*, vol. 3, pp. 549-556, 1958.
- [11] http://en.wikipedia.org/wiki/Fresnel_equations. [Last accessed on 5/9/2015]
- [12] R. K. Luneberg, "Mathematical theory of optics", Brown University Notes, Providence, RI, 1944.
- [13] M. Kline and I. Kay, *Electromagnetic Theory and Geometrical Optics*, Interscience, New York, 1965.
- [14] R. G. Kouyoumjian, L. Peters, Jr., and D. T. Thomas, "A modified geometrical optics method for scattering by dielectric bodies," *IRE Trans. Antennas Propagat.*, vol. AP-11, no. 6, pp.690-703, November 1963.

- [15] R.F. Harrington, *Time-Harmonic Electromagnetic Fields*, McGraw-Hill, New York, 1961.
- [16] D. L. Hutchins, "Asymptotic series describing the diffraction of a plane wave by a two-dimensional wedge of arbitrary angle", Ph.D. dissertation, Dept. of Electrical Engineering, Ohio State University, 1967.
- [17] J. R. Wait, *Electromagnetic Radiation from Cylindrical Structures*, Pergamon, New York, 1959.11-19
- [18] G. N. Watson, "The diffraction of electrical waves by the earth," *Proceedings of the Royal Society of London*, Series A95, pp. 83-99, October 1918.11-35
- [19] L. B. Felsen and N. Marcuvitz, *Radiation and Scattering of Waves*, Prentice-Hall, Englewood Cliffs, N.J., 1973.11-37,12-47
- [20] F. B. Hildebrand, *Advanced Calculus for Applications*, Prentice-Hall, Englewood Cliffs, N.J., 1962.12-48
- [21] W. Pauli, "On asymptotic series for functions in the theory of diffraction of light," *Physical Review*, vol. 34, pp. 924-931, December 1938. 11-38
- [22] F. Oberhettinger, "On asymptotic series occurring in the theory of diffraction of waves by a wedge," *J. Math. Phys.*, vol. 34, pp. 245-255, 1956. 11-39
- [23] J. Boersma, "Computation of Fresnel integral," *Math. Comp.*, vol. 14, p. 380, 1960.
- [24] G. L. James, "An approximation to the Fresnel integral," *Proceedings of the IEEE*, vol. 67, no. 4, pp. 677-678, April 1979.
- [25] K. A. Chamberlin and R. J. Luebbers, "An evaluation of Longley-Rice and GTD Propagation Models," *Proceedings of the IEEE*, vol. AP-30, no. 6, pp. 1093-1098, November 1982.
- [26] A. G. Longley and P. L. Rice, "Prediction of Tropospheric Radio Transmission Loss Over Irregular Terrain. A Computer Method-1968," *ESSA Technical Report ERL79-ITS 67*, Institute for Telecommunications Sciences, July 1968.
- [27] G. A. Hufford, A. G. Longley and W. A. Kissick, "A Guide to the use of the ITS Irregular Terrain Model in the Area Prediction Mode," *NTIA Report 82-100*, U.S. Department of Commerce, April 1982.
- [28] https://en.wikipedia.org/wiki/Longley%E2%80%93Rice_model [Last accessed on 5/9/2015]
- [29] P. L. McQuate, J. M. Harman, A. P. Barsis, "Tabulations of Propagation Data over Irregular Terrain in the 230-to-9200-MHz Frequency Range Part1: Gunbarrel Hill Receiver Site," *ESSA Technical Report ERL65-ITS 58*, Institute for Telecommunications Sciences, March 1968.